GALACTIC CORONA OR LOCAL GROUP INTERGALACTIC MEDIUM?

Rik J. Williams[1], **Smita Mathur**[1], **and Fabrizio Nicastro**[2]

[1]Department of Astronomy, The Ohio State University, 140 W. 18th Ave., Columbus, OH 43210 USA
[2]Harvard–Smithsonian Center for Astrophysics, Cambridge, MA USA

ABSTRACT

Cosmological hydrodynamic simulations predict that the low redshift universe comprises of a web of warm–hot intergalactic gas and galaxies, with groups of galaxies and clusters forming at dense knots in these filaments. Our own Galaxy being no exception is also expected to be surrounded by the warm–hot intergalactic medium, filling the Local Group. Some theoretical models also predict the existence of a hot Galactic corona. With X-ray and FUV observations of extragalactic sources, we can probe the warm–hot gas through absorption lines of highly ionized elements. Indeed, *Chandra*, *XMM* and *FUSE* observations have detected $z = 0$ absorption lines toward many sightlines. The debate that has emerged is over the interpretation of these observations: are the $z = 0$ absorption systems from the halo of our Galaxy or from the extended Local Group environment? This has important implications for our understanding of the mass of the Local Group, the physical conditions in the intergalactic medium, the structure of the Galaxy and galaxy formation in general. We will present the current status of the debate and discuss our ongoing observing program aimed at understanding the $z = 0$ absorption systems, with an emphasis on the high quality *Chandra*spectra of the Mrk 421 and Mrk 279 sightlines.

Key words: Intergalactic Medium; Local Group; Galactic Halo.

1. INTRODUCTION

The intergalactic medium (IGM) is expected to contain most of the baryonic matter in the universe, a tenuous filamentary "web" of gas bridging the gaps between collapsed objects such as galaxies and clusters. At high redshifts ($z > 2$) this web appears in quasar spectra as a multitude of Lyman alpha forest absorption lines. In the nearby universe, on the other hand, hydrodynamic simulations show that most of the IGM has been shock–heated to a warm–hot (WHIM) phase with temperatures of $\sim 10^6$ K (Cen & Ostriker, 1999; Davé et al., 2001). At these temperatures scant neutral hydrogen remains, and the IGM is thus best detected through absorption lines from highly ionized metals (Hellsten et al., 1998), particularly O VI, O VII, and O VIII. Recent *Chandra* observations have indeed confirmed that this low–redshift WHIM exists and comprises a baryon content consistent with expectations (Nicastro et al., in preparation Nicastro et al., 2005a,b).

Just as other galaxies are expected to form in the densest "knots" of the cosmic web, we also expect to see WHIM adjacent to, perhaps surrounding, our own Milky Way. Indeed, X-ray spectra of several quasars show likely $z = 0$ O VII absorption. The upper limit on the O VII emission toward Mrk 421 found by Rasmussen et al. (2003) indicates that this absorption system probably has an extremely low density and is thus likely to be extragalactic. Additionally, other nearby low– and high–ionization components may be associated with either the WHIM itself or may represent gas from the WHIM that has cooled and is now in the process of accreting onto the Galaxy; for example, the high–velocity O VI absorption seen with *FUSE* along many quasar lines of sight (Wakker et al., 2003) and neutral hydrogen high–velocity clouds (H I HVCs).

2. THE DEBATE: WHIM OR CORONA?

The origin of the local O VII absorption, and in particular its relation to the observed O VI, is still to a large degree unknown. There is some evidence that these ions could originate in a warm–hot Galactic corona: for example, likely O VII absorption has been detected within 50 kpc of the Galaxy by Wang et al. (2005). The observed deflection and stripping of the Magellanic clouds also lends credence to the existence of a low–density corona. Lower–ionization absorption, such as that from Si IV and C IV, is also seen at the same velocities as some O VI HVCs, indicating that these O VI clouds, at least, may have lower temperatures and higher densities than expected from the WHIM.

However, there are also reasons to believe this absorption

is tracing extended WHIM gas. High column densities of O VI, O VII, and O VIII from the local IGM are predicted by simulations to lie in certain directions (Kravtsov et al., 2002). Furthermore, the mean velocity vector of the O VI HVCs is highest in the local standard of rest and lowest in the Local Group rest frame, indicating that their origin could indeed be extragalactic (Nicastro et al., 2003). The presence of O VII between the Galaxy and Large Magellanic Cloud does not rule out an extragalactic origin for the absorption in some directions since neither the Galactic absorption or WHIM is necessarily homogeneous; additionally, the WHIM is known to be homogeneous and consist of a variety of temperature and density phases, so some lower–ionization lines may be expected as well.

Thus, the questions – how are the local X-ray and UV absorption components related to each other, which are of Galactic origin, and which arise in the local WHIM?– are still unanswered. The answers to these questions have profound implications for both studies of galaxy formation and cosmology. We are now undertaking a program to determine the distribution and properties of this local hot gas and its ties to lower–ionization components, with a focus on new and archival *Chandra* and *FUSE* data. Here we present the first results of this study, an analysis of the particularly high–quality *Chandra* and *FUSE* spectra of the bright AGN Mrk 421 and Mrk 279.

3. THE MRK 421 SIGHTLINE

A full discussion of the Mrk 421 *Chandra* and FUSE spectra, and the analysis thereof, can be found in Williams et al. (2005); the following is a summary of the main results.

3.1. Observations and measurements

The bright $z = 0.03$ blazar Mkn 421 was observed during two exceptionally high outburst phases for 100 ks each as part of our *Chandra*–AO4 observing program: one at $f_{0.5-2\mathrm{keV}} = 1.2 \times 10^{-9}\,\mathrm{erg\,s^{-1}\,cm^{-2}}$ with the Low Energy Transmission Grating (LETG) combined with the ACIS-S array, and another at $f_{0.5-2\mathrm{keV}} = 0.8 \times 10^{-9}\,\mathrm{erg\,s^{-1}\,cm^{-2}}$ with the HRC-S array and LETG. Each of these observations contains ~ 2500 counts per resolution element at 21.6 Å. Additionally, another short observation of Mkn 421 was taken with HRC/LETG (29 May 2004), providing another 170 counts per resolution element. These three spectra were combined over the 10–60 Å range to improve the signal–to–noise ratio (S/N$\sim$ 55 at 21 Å with 0.0125 Å binning). The final coadded spectrum of Mkn 421 is one of the best ever taken with *Chandra*: it contains over 10^6 total counts with ~ 6000 counts per resolution element at 21.6 Å, providing a 3σ detection threshold of $W_\lambda \sim 2$ mÅ ($N_{\mathrm{OVII}} = 8 \times 10^{14}\mathrm{cm^{-2}}$ for an unsaturated line).

Using the CIAO fitting package Sherpa we initially modeled the continuum of Mkn 421 as a simple power law with Galactic foreground absorption, excluding the 48–57 Å HRC chip gap region. Metal abundances for the Galactic gas were then artificially adjusted to provide a better fit around the O 1 and C 1 K–edges near 23 Å and 43 Å respectively. This is *not* intended to represent actual changes to the absorber composition, but rather to correct uncertainties in the instrument calibration. After this fit there were still some systematic uncertainties in the best–fit continuum model; these were corrected with broad (FWHM $= 0.15 - 5$ Å) Gaussian emission and absorption components until the modeled continuum appeared to match the data upon inspection. Indeed, the residuals of the spectrum to the final continuum model have a nearly Gaussian distribution, with a negative tail indicating the presence of narrow absorption lines (see Nicastro et al., 2005a, Figure 8). We searched for narrow, unresolved (FWHM< 0.05 Å) absorption lines at known C, N, O, and Ne transition wavelengths and used Gaussians to measure the equivalent widths (or upper limits thereupon) for all lines found. All in all, equivalent widths for 9 significantly detected absorption lines were measured (including O VII Kα, β, and γ) and 4 upper limits calculated.

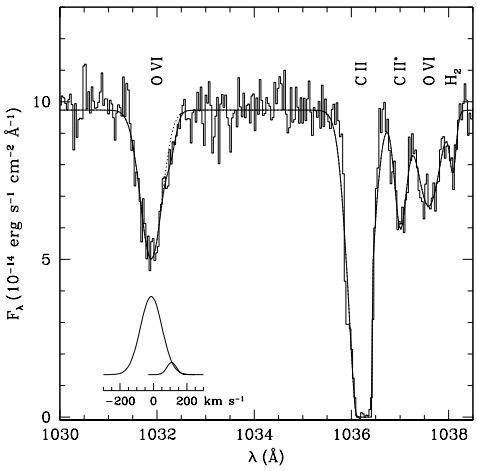

Figure 1. FUSE spectrum of Mrk 421 near the O VI doublet. The 1032 Å line is well–fit by a strong absorber at $v \sim 0\,km\,s^{-1}$ and a much weaker component at $v \sim 100\,km\,s^{-1}$ (inset).

Mrk 421 was also observed for a total of 84.6 ks with FUSE, providing a signal–to–noise ratio of 17 near the O VI wavelength once all spectra are combined and binned to $\sim 10\,\mathrm{km\,s^{-1}}$. This spectrum shows strong, broad O VI absorption at $v \sim 0$, most likely originating in the Galactic thick disk, as well as a possible O VI HVC at $v \sim 110\,\mathrm{km\,s^{-1}}$ (Figure 1).

3.2. Doppler parameters

To convert the measured equivalent widths to ionic column densities, we calculated curves of growth for each

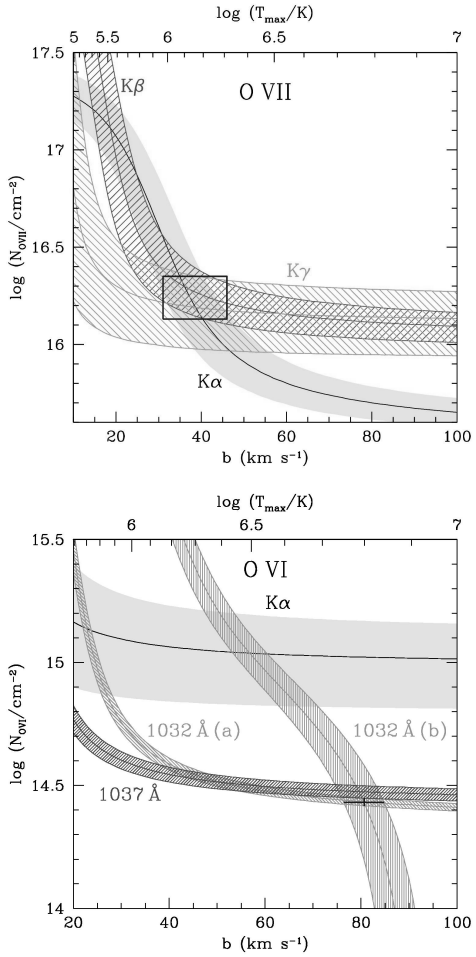

Figure 2. Mrk 421 column density and Doppler parameter diagnostics for the O VII *(top) and O* VI *(bottom) absorption, with each transition labeled. In the O* VI *panel, the "a" and "b" curves are derived from the 1032 Å absorption equivalent width and FWHM, respectively.*

absorption line over a grid of Doppler parameters ($b = 10-100\,\mathrm{km\,s^{-1}}$) and column densities ($\log N_H/\mathrm{cm^{-2}} = 12.0 - 18.0$), assuming a Voigt line profile. Since the X-ray lines are unresolved, b cannot be measured directly. It can, however, be inferred from the relative strengths of the three measured O VII K–series lines. These line ratios by themselves are insufficient to determine the physical state of the O VII–absorbing medium since b and $N_{\rm OVII}$ are degenerate: the Kα line saturation could be due to high column density, low b, or a combination of both. However, given an absorption line with a measured equivalent width and known oscillator strength, the inferred column density as a function of the Doppler parameter can be calculated. The measured equivalent width (and errors) for each transition thus defines a region in the $N_{\rm OVII} - b$ plane. Since the actual value of $N_{\rm OVII}$ is fixed, b and $N_{\rm OVII}$ can be determined by the region over which the contours "overlap;" i.e. the range of Doppler parameters for which the different transitions provide consistent $N_{\rm OVII}$ measurements.

Figure 2 (top panel) shows such 1σ contours for the three measured O VII transitions. The Kα and Kβ tracks appear consistent at the 2σ level for $13 < b < 55\,\mathrm{km\,s^{-1}}$, while the overlap between the Kα and Kγ tracks provides approximate 2σ limits of $24 < b < 76\,\mathrm{km\,s^{-1}}$. We thus assume a 2σ range of $24 < b < 55\,\mathrm{km\,s^{-1}}$. It should be noted that Figure 2 also shows some overlap between the K_α and K_γ at $b \leq 12\,\mathrm{km\,s^{-1}}$; however, this solution is unlikely given the lower limit provided by the K_β line. Moreover, $b = 12\,\mathrm{km\,s^{-1}}$ implies a maximum temperature (assuming purely thermal motion) of $T_{\rm max} = 1.3 \times 10^5\,\mathrm{K}$; such a low temperature is unlikely to produce the observed strong high–ionization lines.

A similar analysis is not as effective when applied to the strong O VI$_{\rm LV}$ UV doublet (from the thick disk), since these lines are only slightly saturated. The O VI$_{\rm LV}$ 1032 Å line is fully resolved by *FUSE* and relatively unblended, so its Doppler parameter can be estimated much more accurately using the measured line width and strength. In an unsaturated absorption line, $\mathrm{FWHM} = 2(\ln 2)^{1/2} b$; however, the measured FWHM increases if the line is saturated. We compensated for this by calculating Voigt profile FWHMs on a grid of $N_{\rm OVI}$ and b, and determining the region consistent with the O VI$_{\rm LV}$ 1032 Å FWHM measurement of $152 \pm 7\,\mathrm{km\,s^{-1}}$.

When the FWHM–derived contour is overlaid on the $N_{\rm OVI} - b$ contour inferred from the equivalent width measurement of the LV–O VI 1032 Å line, the two regions overlap nearly orthogonally (Figure 2, bottom panel) leading to a constraint of b(O VI$_{\rm LV}$)$= 80.6 \pm 4.2\,\mathrm{km\,s^{-1}}$. This is more than 3σ higher than the Doppler parameter calculated for the O VII absorption, indicating that the O VII and thick–disk O VI$_{\rm LV}$ cannot arise in the same gaseous phase. Also, at no value of the Doppler parameter do the 1032 Å, 1037 Å, and O VI Kα lines all produce a consistent $N_{\rm OVI}$ measurement; in fact, the O VIKα column density is a factor of ~ 4 higher than that inferred from the UV data. It is thus possible that the O VI UV transition is being suppressed, perhaps by atomic physics effects, in the absorbing medium and the $K\alpha$ line produces a more accurate representation of the true O VI column density; in the following analysis we consider both possibilities.

3.3. Temperature and Density Constraints

The abundance ratios of metal ions (for example, O VII/O VIII) are expected to vary with temperature as a result of collisional ionization; additionally, as the density decreases to typical WHIM values ($\sim 10^{-4}\,\mathrm{cm^{-3}}$), photoionization from the extragalactic ionizing background plays an increasingly important role. We used Cloudy version 90.04 (Ferland, 1996) to calculate relative ionic abundances for all measured elements over a grid of $\log T$ and $\log n_e$. As with the Doppler parameter and column density diagnostics described above, any measured ion column density ratio then produces a "track" of consistency in the $\log T - \log n_e$ plane, and (assuming the

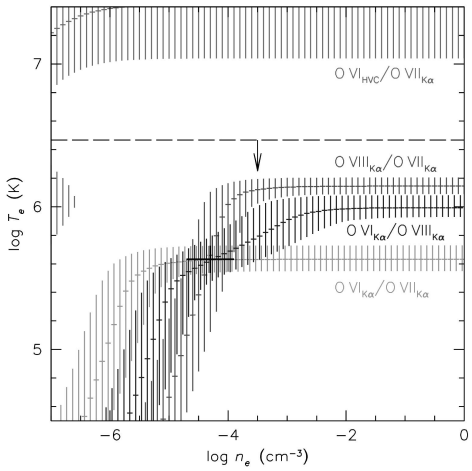

Figure 3. 2σ *constraints on the gas temperature and density toward Mrk 421, derived from oxygen ion ratios as labeled. The dashed line indicates the upper limit on the temperature from the* O VII *Doppler parameter.*

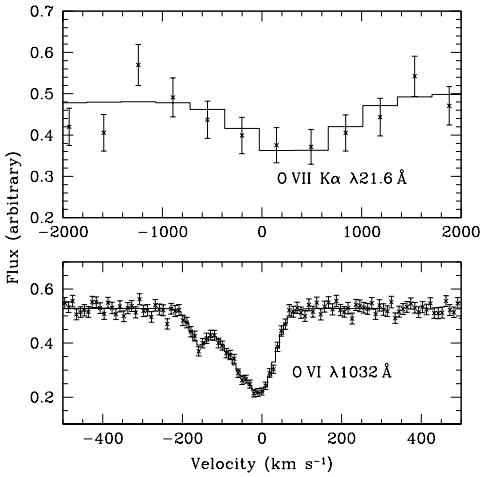

Figure 4. Velocity plot of the O VII *and* O VI *absorption seen in the Mrk 279* Chandra *and* FUSE *spectra respectively. The centroids of the* O VII *and high–velocity* O VI *lines differ by* $\sim 2.5\sigma$.

ions arise in the same gaseous phase) the overlap between such "tracks" can place constraints on the gas temperature and density.

Column density ratios between different ions of the same element (e.g. O VI, O VII, and O VIII) produce the strongest constraints since these ratios are independent of the relative metal abundance in the gas Figure 3 shows such constraints derived from these oxygen abundance ratios. If the O VI Kα line accurately traces the O VI column density of this medium, then the contours overlap at $n_e \sim 10^{-4}$ cm^{-3}. Coupled with the total oxygen column density and assuming O/H of 0.3 times Solar, this implies that the absorber has a radial extent of ~ 1 Mpc and a mass consistent with the expected baryonic mass of the Local Group.

On the other hand, if the O VI Kα line does *not* correctly measure $N_{\rm OVI}$, then this absorption can in principle arise in a higher–density Galactic medium with $\log T \sim 6.1$ (as derived from the O VIII/O VII ratio with collisional ionization as the dominant process; Figure 3). Even in this case, a low–density (extragalactic) medium is fully consistent with the data. Furthermore, the contour derived from the measured Ne/O abundance (not shown in the figure) is consistent in the low–density regime if the Ne/O ratio is significantly supersolar, as has been observed in other Galactic and extragalactic absorption systems.

4. THE MRK 279 SIGHTLINE

A full discussion of our analysis of the Mrk 279 *Chandra* and *FUSE* spectra will appear in a forthcoming paper (Williams et al. 2006, in preparation).

4.1. Observations and Measurements

While Mrk 421 was observed for relatively short periods during bright outburst phases, few other bright sources flare this dramatically. We thus searched the *Chandra* archive for long–duration LETG observations of relatively bright background quasars. One such source, Mrk 279 (an AGN at $z = 0.03$) was observed during seven periods in May 2003 for a total exposure time of 340 ks. These seven observations were coadded for a final (unbinned) signal–to–noise ratio of $\rm S/N \sim 6.5$ near 22Å. As with the Mrk 421 spectrum, we again used Sherpa to fit a power law and foreground Galactic absorption to the spectrum over $10 - 100$ Å band (excluding the $49 - 57.5$ Å and $60.5 - 67.5$ Å chip gap regions), leaving the relative Galactic metal abundances as free parameters in order to produce a better fit around the absorption edges. The remaining broad residuals were were corrected by including four broad Gaussians in the source model.

Although several strong lines such as C VI, O VII, and N VII are apparent at the blazar redshift ($z = 0.03$), only O VII Kα $\lambda 21.602$ is unambiguously detected at 21.623 ± 0.012Å ($v = 290 \pm 170\,{\rm km\,s^{-1}}$) with an equivalent width of 25.7 ± 5.3 mÅ. Upper limits are measured for the O VII Kβ and O VIII lines. The *Chandra* LETG wavelength scale contains intrinsic random errors of approximately 0.01Å, on the order of the statistical error on the O VII position measurement, but these errors should not vary with time (J. J. Drake, private communication). To check the absolute wavelength scale near the O VII line, we retrieved the nearest HRC–S/LETG calibration observation of the X-ray bright star Capella (observation 3675, taken on 2003 September 28) from the *Chandra* archive and reprocessed the data in exactly the same manner as the Mrk 279 data. The wavelength of the strong O VII emission line was found to be

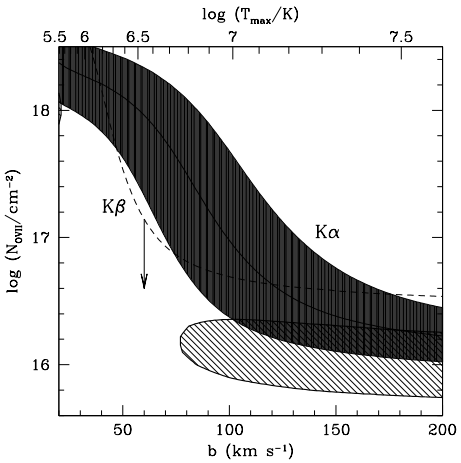

Figure 5. Column density and velocity dispersion diagnostics for the Mrk 279 O VII *absorption. The shaded region is derived from the* 1σ *O* VII *K*α *equivalent width limits, the dashed line is from the O* VII *K*β 2σ *upper limit, and the 95% joint confidence interval is depicted by the dark hatched region.*

21.606 ± 0.002Å or $56 \pm 28\,\mathrm{km\,s^{-1}}$, which is consistent with the $+30\,\mathrm{km\,s^{-1}}$ radial velocity of Capella as listed in the SIMBAD database. Thus, any systematic effects on the measured velocity of the O VII absorption are likely to be insignificant compared to the statistical error.

Mrk 279 was also observed with *FUSE* for a total exposure time of 224 ks (though only 177 ks of these data were usable); all calibrated data from these observations were retrieved and coadded in the same manner as the Mrk 421 *FUSE* data. This spectrum also shows strong Galactic thick–disk O VI absorption at $v \sim 0$, but unlike the Mrk 421 spectrum, the high–velocity O VI is strong and clearly separated from the thick–disk O VI at $v = -160 \pm 2.6\,\mathrm{km\,s^{-1}}$. Figure 4 shows the O VII and O VI absorption systems plotted against velocity. Although the error on the O VII velocity is large, it is nonetheless significantly higher than the O VI HVC velocity by about 2.5σ. Thus, a direct association between the O VI HVC and O VII can be ruled out with reasonably high confidence.

4.2. Doppler parameters

In the Mrk 421 *Chandra* spectrum, three absorption lines from the O VII K-series were strongly detected. While a similar curve–of–growth analysis can be performed for Mrk 279, placing limits on N_{OVII} and b is more difficult because only the O VII Kα line is strongly detected; only an upper limit can be measured for the Kβ line. Since the absorption line properties for various column densities and Doppler parameters are known, limits on these quantities can be determined using the *Chandra* spectrum itself. For each point in the $N_{\mathrm{OVII}} - b$ plane, O VII Kα and Kβ absorption lines with the calculated W_λ and FWHM values were added to the best–fit continuum model, and the χ^2 statistic calculated using the "goodness" command in Sherpa. Since best–fit Kβ line amplitude is zero, the unsaturated case (assuming the O VII line ratio constraint $W_\lambda(K\beta) = 0.15 * W_\lambda(K\alpha)$) produces the best fit to the data. The minimum χ^2 value was taken from such a fit, and $\Delta\chi^2 = \chi^2(N_{\mathrm{OVII}}, b) - \chi^2_{\mathrm{min}}$ calculated for every point. The 95% confidence interval ($\Delta\chi^2 < 6$) calculated with this method is shown in Figure 5 (as well as the $N_{\mathrm{OVII}} - b$ contours derived from each transition); at this confidence level all Doppler parameters between $20 < b < 77\,\mathrm{km\,s^{-1}}$ are ruled out.

Doppler parameters for the O VI absorption were calculated in the same manner as for Mrk 421. In this case, however, two Gaussians are necessary to fit the low–velocity (thick–disk) O VI. The derived velocity dispersions are $b = 61.5 \pm 3.5, 38.8 \pm 2.8$, and 32.0 ± 4.6 for the broad Galactic, narrow Galactic, and high–velocity O VI components respectively (producing the best–fit model shown in Figure 4). These are all strongly inconsistent with the limits found for the O VII velocity dispersion, indicating that the O VII is not related to any of the O VI components. Even if the low–velocity O VI is considered to be one non–Gaussian component and its width is measured directly from the spectrum, its Doppler parameter is $b \sim 80\,\mathrm{km\,s^{-1}}$, barely consistent with the 95% lower limit on the O VII b value.

4.3. Temperature and Density Constraints

An upper limit on the temperature of the absorbing medium of $\log T < 6.3$ can be derived from the O VIII/O VII column density. Since the O VII absorption does not appear to be associated with any of the O VI components, finding a lower limit on the temperature is more difficult. We thus assume that the O VI absorption from the O VII–bearing gas is undetected in the *FUSE* spectrum, and exists as a very broad ($b > 80\,\mathrm{km\,s^{-1}}$) absorption line superposed on the narrower detected components. Limits on the O VI column density associated with the O VII were thus calculated by placing such an absorption line in the *FUSE* spectrum model, one with $b = 100\,\mathrm{km\,s^{-1}}$ and one with $b = 200\,\mathrm{km\,s^{-1}}$, and calculating the corresponding O VI/O VII $T - n_e$ constraint (shown in Figure 6.

The lower limit on temperature derived from the O VI/O VII upper limit is highly dependent on b; in fact, for $b = 100\,\mathrm{km\,s^{-1}}$ the two oxygen line ratios are inconsistent with each other for *all* temperatures and densities. Thus, if the O VII is associated with an undetected broad O VI line, the velocity dispersion of the absorption must be very high (at least $b \sim 200\,\mathrm{km\,s^{-1}}$). Such a high velocity dispersion, if purely thermal, implies temperatures of $T \sim 10^7$ K, which is ruled out by the non–detection of O VIII absorption. This absorber must therefore be broadened primarily by nonthermal processes, perhaps due to the velocity shear of infalling hot gas associated with HVC Complex C.

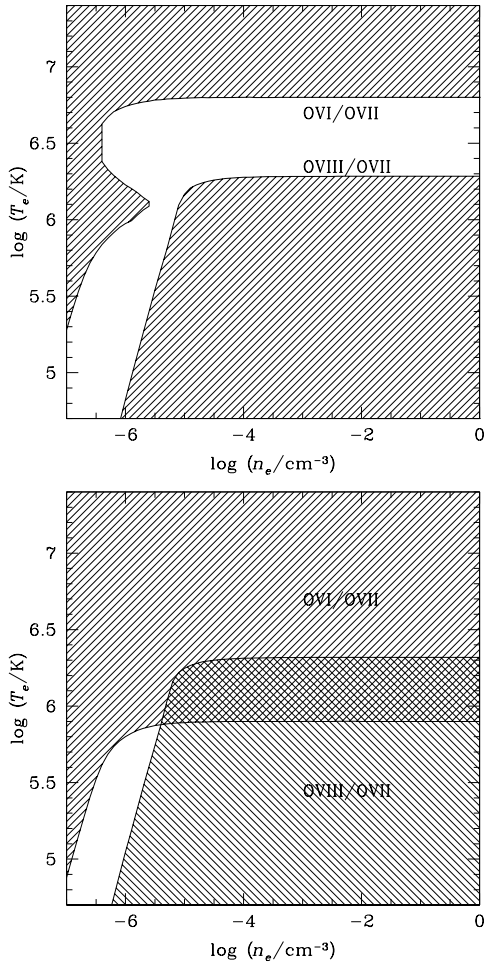

Figure 6. Mrk 279 temperature and density constraints from the O VIII*/O* VII *and O* VI*/O* VII *upper limits, assuming a putative O* VI *absorption line with* $b = 100\,km\,s^{-1}$*(top) and* $b = 200\,km\,s^{-1}$*(bottom).*

5. CONCLUSIONS

We have detected strong $z = 0$ X-ray absorption toward both Mrk 421 and Mrk 279. Both absorption systems appear to exhibit similar column densities and consistent temperature and density limits (albeit with large errors). Additionally, in both cases the detected X-ray absorption does *not* appear to arise in the same phase as the low– or high–velocity O VI absorption seen in the *FUSE* spectra, indicating that the O VII absorption likely comes from either the local WHIM or a heretofore undiscovered hot Galactic component. The Doppler parameters of the Mrk 421 and Mrk 279 absorption are highly inconsistent with each other, perhaps indicating that these two systems originate from entirely different physical processes.

ACKNOWLEDGMENTS

We thank the conference organizers for an enjoyable and informative week, and the *Chandra* and *FUSE* teams for their exceptional efforts on these missions. This work has been supported by *Chandra* award AR5-6017X issued by the *Chandra* X-ray Observatory Center, which is operated by the Smithsonian Astrophysical Observatory for and on behalf of the NASA under contract NAS8-39073. RJW derives additional support from an Ohio State University Presidential Fellowship.

REFERENCES

Cen, R., & Ostriker, J. P. 1999, ApJ, 514, 1

Davé, R., et al. 2001, ApJ, 552, 473

Ferland, G. J., 1996, Hazy, a Brief Introduction to Cloudy 90, University of Kentucky, Physics Department Internal Report

Hellsten, U., Gnedin, N. Y., & Miralda–Escudé, J. 1998, ApJ, 509, 56

Kravtsov, A. V., Klypin, A., & Hoffman, Y. 2002, ApJ, 571, 563

Nicastro, F., et al. 2003, Nature, 421, 719

Nicastro, F., et al. 2005, ApJ, 629, 700

Nicastro, F., et al. 2005, Nature, 433, 495

Rasmussen, A., Kahn, S. M., & Paerels, F. 2003, ASSL Conference Proceedings, 208, 109

Wakker, B. P., et al. 2003, ApJS, 146, 1

Wang, Q. D., et al. 2005, ApJ, accepted (astro-ph/0508661)

Williams, R., et al. 2005, ApJ, 631, 856

INVESTIGATING HEATING AND COOLING IN A SAMPLE OF CLUSTERS

R. J. H. Dunn and A. C. Fabian

Institute of Astronomy, Cambridge, UK

ABSTRACT

We select clusters from the Brightest 55 sample which have a short central cooling time and a large central temperature drop as these require some form of heating. 20 clusters meet this requirement, of which at least 14 contain clear bubbles. The median radius out to which the bubble power can offset the X-ray cooling is $0.98r_{\rm cool}$. Using these average values for the clusters with bubbles, the expected size of bubbles in the clusters in the B55 sample which contained a central radio source was calculated. The expected sizes are very similar to the observed radio source lobes in the cases where they are resolved.

Key words: Clusters; Heating; Radio Bubbles.

1. INTRODUCTION

Since the discovery of strong X-ray emission in clusters of galaxies, the thermal plasma which makes up the Intra-Cluster Medium (ICM) has been known to be cooling. As the temperature of the gas falls, it would lose pressure support unless it flows inwards to the centre of the gravitational potential. Such a flow is known as a cooling flow.

However, with the advent of *Chandra* and *XMM-NEWTON*, little X-ray cool gas was found; the cooling flow problem. Cooling appears to terminate at around 1/3 of the virial temperature e.g. Peterson et al. 2001. Various mechanisms have been proposed by which the cool gas could be heated, including thermal conduction, but this doesn't appear to work for clusters below $5\,\mathrm{keV}$ (Voigt & Fabian, 2004). Active Galactic Nuclei (AGN) have been observed at the centre of many clusters. In some clusters there are decrements in the X-ray emission which anti-correlate spectacularly with the extended radio emission. These holes in the X-ray emission have been interpreted as bubbles of relativistic plasma, blown by the AGN. Ghost bubbles, ones without GHz radio emission, have also been discovered, and these are thought to be rising buoyantly up through the ICM. Deep images of the Perseus and Virgo Clusters (Fabian et al., 2003; Forman et al., 2003) show pressure waves which are a mechanism by which the energy contained within the bubble could be transferred to the ICM.

Studying a large sample of clusters would be useful in providing a concept of what an "average" cluster was as many recent studies have concentrated on clusters which are abnormal – the brightest, hottest, closest and morphologically most interesting. Then with the properties for an average cluster the processes occurring at the centres of clusters would be clearer, especially the heating processes. An extension of this cluster survey to higher redshift would allow the study of the evolution of heating processes as clusters continue to form.

2. SAMPLE SELECTION

The sample of clusters from which our subset was taken was the Brightest 55 (B55) sample from Edge et al. (1990), which was further analysed by Peres et al. (1998) using *ROSAT* data. It is a $2-10\,\mathrm{keV}$ flux-limited sample of X-ray clusters which are all close enough to have been imaged at sufficient resolution by the previous generation of X-ray instruments. From this sample we looked at those clusters which had a short central cooling time ($t_{\rm cool} \leq 3\,\mathrm{Gyr}$) and a central temperature drop such that $T_{\rm centre}/T_{\rm outer} < 1.2$ as these are the clusters which are most likely to require some form of heat source to stem cooling.

Out of the 55 clusters, 23 have a short $t_{\rm cool}$ and 21 have a central temperature drop. 20 clusters have both and as such require some form of heating. Of these 14 (almost 75%) have clear X-ray depressions (Dunn et al., 2005). Of the remaining six clusters required heating but containing no clear bubbles, five have radio emission from their core. AWM7 is the only cluster in the sample which requires some form of heating to offset the X-ray cooling but has neither bubbles nor a central radio source. This proportion of clusters containing bubbles matches that from Eilek (2004) and Marković et al. (2004) who selected their clusters using mass deposition rate and the size of the central cluster galaxy.

Table 1. Cluster Sample

Bubbles Heating	Radio		No Radio Heating
	Heating	No Heating	
2A0335+096*	A496	3C129.1	AWM7
A85	A2204†	A399	
A262	PKS0745-191†	A401	
A426		A576	
A478		A754	
A1795		A1644	
A2029		A1650	
A2199		A3112	
A2597		A3391	
A4059		Klem44	
Centaurus			
Cygnus A			
Hydra A			
M87			
MKW3s*			

* These clusters do not have *c*lear bubbles but the X-ray decrements have been interpreted as such.
† These clusters are above $z = 0.1$.

Bîrzan et al. (2004) found that 16 out of 80 clusters in the *Chandra* archive contained bubbles, however their sample contained all clusters, and not just those which are likely to require some form of heating.

Two clusters which require heating but do not have clear bubbles are 2A0335+096 and MKW 3s. 2A 0335+096 has a complicated lumpy core and so contains X-ray depressions, however they do not have much radio emission associated with them. Mazzotta et al. (2003) interpreted these depressions as bubbles and so this cluster is included with the "bubbled" clusters. MKW 3s also has features in the X-ray emission which may be bubbles, though they are a long way out in the cluster (Mazzotta et al., 2002). This cluster is also added into the sample of clusters containing clear bubbles, making 16.

In addition to the clusters which require heating, those clusters in B55 sample which contain a central radio source were also analysed. This adds another 10 clusters into the sample, making 30 in total; 16 have bubbles, 13 have a radio source (of which 10 do not have a short central cooling time *and* a central temperature drop) and AWM7. The total sample is shown in Table 1.

3. BUBBLE ANALYSIS

Using archive data the publicly available dataset with the longest exposure time was obtained for all the clusters in the sample. Standard reprocessing and deprojection was performed, obtaining radial temperature, density and pressure profiles as well as the heating required per annulus to offset the X-ray cooling.

For the clusters containing clear bubbles the energy in the bubbles was determined using the $4pV$ work done, where the factor of 4 is $\gamma/(\gamma-1)$ for a relativistic gas. Using the sound speed timescale for the young active bubbles, and the buoyancy timescale for the ghost bubbles the power deposited by the bubble in the ICM was calculated. A comparison of the bubble power to the heating required per annulus gives the median radius out to which the bubbles offset the X-ray cooling as $0.98r_{\rm cool}$, where $r_{\rm cool}$ has been calculated for a cooling time of $3\,{\rm Gyr}$.

There is a large spread in the distance out to which the bubble power can offset the cooling – almost $4r_{\rm cool}$ for A2052, but only $0.08r_{\rm cool}$ for Centaurus. The spread of the fraction of heat supplied within $r_{\rm cool}$ is also large – $10.5\times$ for Cygnus A, but only $0.03\times$ for Centaurus. Therefore, in order for the bubbles to offset all of the X-ray cooling, on average the AGN have to be active for a large proportion of the time. Some bubbles are sufficiently powerful to provide more heating than required by the X-ray cooling in the region of the cluster currently analysed.

3.1. Perseus

The radio source at the centre of the Perseus Cluster (3C84) has a complicated "S" or "Z" shaped morphology. Dunn et al. (2005) explain this with the central regions of the source containing two pairs of bubbles – an inner and an outer pair. If these bubbles are treated separately then the power supplied by the bubbles goes up by $1.4\times$. This increases the radius out to which the X-ray cooling is offset by the bubbles from $75\,{\rm kpc}$ to $100\,{\rm kpc}$ $(1.3r_{\rm cool})$.

4. BUBBLE PREDICTIONS

The clusters which do not contain clear bubbles were reprocessed and deprojected in the same way, and profiles for the heating required per annulus to offset the X-ray cooling were obtained. The median value for the radius out to which an average bubble offsets the X-ray cooling in the clusters with bubbles were used to calculate the power an average bubble placed at the centres of the clusters with no bubbles would have to produce. In the assumption that all of the bubbles are young and as such expanding at the sound speed, the size of an "average" bubble corresponding to that cluster was calculated. AWM7 was included in this analysis even though it does not appear to contain a central radio source.

Table 2. Bubble Expectations

Cluster	Expected Bubble Radius (kpc)	Observed Radio Radius (kpc)
3C129.1	1.72	2.6×2.6
A399	2.53	
A401	1.44	
A496	2.43	
A576	0.50	
A754	0.78	
A1650	3.61	
A1644	2.32	
A2204	8.46	5.1×4.6
A3112	5.98	
A3391	2.63	$\sim 20 \times 30$
AWM7	3.39	None
Klem44	3.44	
PKS0745	7.61	$9.2 \times 6.0^*$

* full dimensions of the amorphous radio source.
Radio source present in the cluster unless specified.

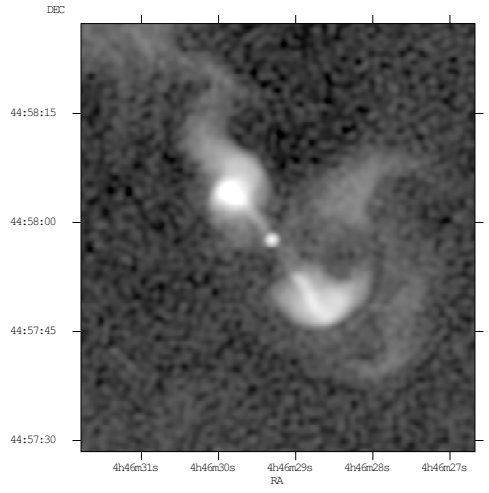

Figure 1. The 5 GHz *radio emission from 3C129.1*

For three of the clusters VLA Radio images show bi-lobed morphologies, very similar to those radio sources in clusters which do show clear bubbles (see Fig. 1); in two of these cases the sizes match very well (see Table 2). These are only average bubbles and so although for A3391 the expected size is much smaller than what is observed, this is not a problem given the range in supplied heating calculated for the clusters with bubbles. The two highest redshift sources (A2204 and PKS 0745-191) along with the others have expected bubble sizes which are only a few *Chandra* pixels in radius and so may not be clearly obvious in short exposure times, especially if their contrast is small. PKS 0745-191 is an amorphous radio source and so describing the interaction of the radio source with the ICM with bubbles may not be correct.

5. FUTURE PROSPECTS

This analysis assumed that the energy contained within the bubble is $4pV$. If the energy is just pV then on average the heating supplied by the bubble is not going to be enough to stem the X-ray cooling. The analysis also assumes that all of the energy within the bubble is transferred to the ICM where it can stem the cooling. However is this reasonable?

It has been shown that the inflation of the bubbles can produce sound waves in the gas (Fabian et al., 2003). These waves can dissipate some of their energy as heat as they travel out in the cluster. However this is going to occur over a much longer timescale than that of the bubble creation.

The bubbles have been assumed to be travelling at the sound speed as there are no strong shocks observed in the rims surrounding them, in fact the rims can contain the coolest gas in the cluster. However, as the jets that create the bubbles are expected to be relativistic then the early expansion of the bubbles would be expected to be supersonic. The buoyancy rise-time for the bubbles was used for the ghost bubbles. For further discussions of the timescales involved see Dunn et al. (2005).

Although the bubbles are created at a rate corresponding to the power described above, the energy they contain is unlikely to be liberated over the same time period as this would imply that the bubbles would dissipate very quickly and so ghost bubbles of the size and scale observed would not be seen. If the bubbles are, on the whole, providing the heating for the central regions of the cluster then if the bubbles dissipate their energy over a longer time, and so larger volume of the cluster, the AGN would have to be active for a large proportion of the time.

This is only a relatively small sample – 16 clusters with bubbles and 14 clusters without. A larger sample, work on which is underway, would improve the confidence in the results. Extending the sample to higher redshifts

would also show the evolution of heating and cooling processes over time.

6. CONCLUSIONS

Out of the Brightest 55 sample, 20 clusters require some form of heating. Of these at least 14 (75%) contain clear bubbles. The bubbles in these clusters, as well as those in two more which have less obvious X-ray depressions, can offset the cooling from X-ray emission out to $0.98r_{\rm cool}$ (median). The 14 clusters which do not have bubbles, of which 10 do not require heating given our selections, all but one contain a central radio source. The average bubbles expected in these clusters are such that with short exposures they may not have been seen as yet. However the sizes match the observed bi-lobed morphologies seen in three of the cluster radio sources.

ACKNOWLEDGEMENTS

We thank Jeremy Sanders and Roderick Johnstone for technical support and interesting discussions during the course of this work. RJHD and ACF acknowledge PPARC and The Royal Society respectively.

REFERENCES

Bîrzan L., Rafferty D. A., McNamara B. R., Wise M. W., Nulsen P. E. J., 2004, ApJ, 607, 800

Dunn R. J. H., Fabian A. C., Sanders J. S., 2005, MNRAS, submitted

Dunn R. J. H., Fabian A. C., Taylor G. B., 2005, MNRAS, accepted, astro-ph/0510191

Edge A. C., Stewart G. C., Fabian A. C., Arnaud K. A., 1990, MNRAS, 245, 559

Eilek J. A., 2004, in The Riddle of Cooling Flows in Galaxies and Clusters of galaxies

Fabian A. C., Sanders J. S., Allen S. W., Crawford C. S., Iwasawa K., Johnstone R. M., Schmidt R. W., Taylor G. B., 2003, MNRAS, 344, L43

Forman W. et al., 2003, astro-ph/0312576

Marković T., Owen F. N., Eilek J. A., 2004, in The Riddle of Cooling Flows in Galaxies and Clusters of galaxies

Mazzotta P., Edge A. C., Markevitch M., 2003, ApJ, 596, 190

Mazzotta P., Kaastra J. S., Paerels F. B., Ferrigno C., Colafrancesco S., Mewe R., Forman W. R., 2002, ApJ, 567, L37

Peres C. B., Fabian A. C., Edge A. C., Allen S. W., Johnstone R. M., White D. A., 1998, MNRAS, 298, 416

Peterson J. R. et al., 2001, A&A, 365, L104

Voigt L. M., Fabian A. C., 2004, MNRAS, 347, 1130

THE INTERACTION BETWEEN THE CENTRAL GALAXY AND THE INTRACLUSTER MEDIUM IN COOL CLUSTER CORES.

N.A. Hatch and C.S.Crawford, A.C Fabian, R.M.Johnstone, J.S. Sanders

Institute of Astronomy, University of Cambridge, Madingley Road, UK

ABSTRACT

The extended emission-line nebulae surrounding the central galaxies of the Perseus and Centaurus clusters show a direct association with soft X-ray filaments indicating an energy exchange between the hot intracluster medium and the warm ionized gas. Radial gradients in the [NII]/Hα ratio imply the ionization state of the line-emitting gas is coupled to the global properties of the intracluster medium or the gas contains significant metallicity variations. The velocity field of filaments within the Perseus cluster core indicate that the filaments are most likely to be galactic gas drawn out of the central galaxy by the buoyant rise of under-dense bubbles.

Key words: ICM; central cluster galaxies.

1. INTRODUCTION

At the centre of galaxy clusters in which the X-ray emitting intracluster medium has a short radiative cooling time, lies the most massive galaxies known. Approximately a third of these central cluster galaxies exhibit line-emission, emitting predominantly in Lyα, Hα and collisionally excited lines e.g. [NII] (Crawford et al., 1999). Deep narrow-band imaging has revealed that these emission-line nebulae can extend over 30 kpc from the central galaxy core in the form of long, narrow filaments (e.g. Perseus: Conselice et al. (2001) [Fig. 1]; M87: Sparks et al. (2004); Centaurus: Crawford et al. (2005)[Fig. 1]). The emission line nebulae are extremely luminous, requiring a constant source of excitation. Despite many studies (e.g. Hu et al. (1985); Heckman et al. (1989); Donahue et al. (2000)) the origin, nature and excitation of these nebulae remain a mystery.

Two well-studied clusters which host line-emitting nebulae around their central galaxies are the Perseus cluster with NGC 1275 residing in the core, and the Centaurus cluster with NGC 4696 in the core. Both clusters have centrally peaked X-ray emission with a short radiative cooling time and like $\sim$70 per cent of central cluster galaxies, they both harbour an active radio source (Burns, 1990). Both cluster cores exhibit cavities in the X-ray emission that spatially coincide with GHz radio-emission (Fabian et al., 2003a; Sanders & Fabian, 2002); these X-ray cavities are known as radio bubbles. Two ICM-confined bubbles of radio plasma surround NGC 4696 to the east and west, whilst two X-ray cavities exhibiting GHz radio-emission lie to the north and south of NGC 1275 in the Perseus cluster core. In addition to the radio bubbles, there are two outer cavities in the Perseus intracluster medium that lie approximately 30 kpc to the northwest and south which do not exhibit GHz radio emission. These cavities, known as ghost bubbles, are interpreted as radio-bubbles that were inflated during a previous epoch of activity, that have detached and risen buoyantly through the intracluster medium.

NGC 1275 is host to the most spectacular emission line nebula imaged so far (see Fig. 1; Conselice et al. (2001)). The nebula is extremely luminous ($>4.1\times10^{41}$erg s^{-1} in Hα and [NII]; Heckman et al. 1989) and consists mostly of radial filaments. A large reservoir of cool molecular gas has been detected in the core of NGC 1275 as is commonly found in the core of many central cluster galaxies (Edge, 2001; Edge et al., 2002). Warm molecular hydrogen is also observed associated with the outer nebula, 25 kpc from the galaxy core (Hatch et al., 2005a).

2. NEBULA-INTRACLUSTER MEDIUM INTERACTION

High resolution, deep *Chandra* images show that soft X-ray emission is associated with some of the optical and UV line-emitting filaments of the nebula surrounding NGC 1275 (Fabian et al., 2003b). Similar soft X-ray emission is found associated with the nebula surrounding M87 at the core of the Virgo cluster (Sparks et al., 2004) and with the 45 kpc filament trailing the central galaxy of Abell 1795 (Fabian et al., 2001).

In the Centaurus core, filaments of soft X-ray emission are clearly visible spiralling east from NGC 4696, the central cluster galaxy (Sanders & Fabian, 2002; Fabian

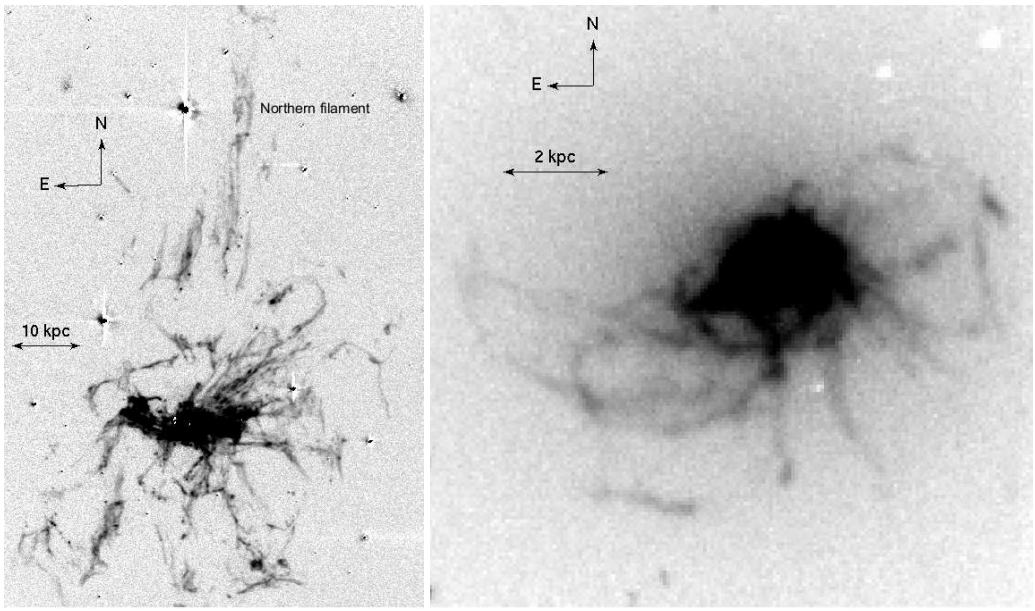

Figure 1. Left: Continuum subtracted Hα emission from NGC 1275 at the core of the Perseus cluster. Data from Conselice et al. (2001). Right: Continuum subtracted Hα emission from NGC 4696 at the core of the Centaurus cluster. Data from Crawford et al. (2005).

et al., 2005a). Comparison with an Hα image of the extended optical nebula that surrounds NGC 4696 shows that the soft X-ray filaments directly align with the optical line-emitting filaments (see Fig. 2). The optical line-emission and the soft X-ray emission share the same spiral structure that is suggestive of a bulk laminar flow and the presence of strong magnetic fields acting on the nebula. Not all bright line-emitting filaments surrounding NGC 4696 have associated soft X-ray emission. Toward the west lies a ring of optical line-emitting gas that surrounds the bubble of radio-emitting plasma. This ring exhibits no clearly associated soft X-ray emission and therefore has a much lower X-ray/Hα ratio than the spiral filaments in the east.

Whereas there is no clear evidence of dust in the nebula surrounding NGC 1275 in the Perseus cluster, the Centaurus core shows clear evidence of dusty filaments. A $B-I$ image of the Centaurus core maps out the distribution of the absorbing dust and shows there are dust features associated with many of the bright nebula filaments (see Fig. 3). The optical/soft X-ray filaments that spiral east match the strong dust features. The prominent innermost dust lane spirals all the way into the galaxy core (Crawford et al., 2005). A bright filament that stretches northwest across the emission-line ring surrounding the radio bubble corresponds to a dust feature, however, there is no absorbing dust associated with the ring of line-emission that also lacks soft X-ray emission. As it is unlikely for dust to form within gas that is condensing from the intracluster medium, the presence of dust within the filaments means it is probable that the Centaurus filaments were not formed *in situ*, but were extracted from a reservoir within the dusty galaxy environment.

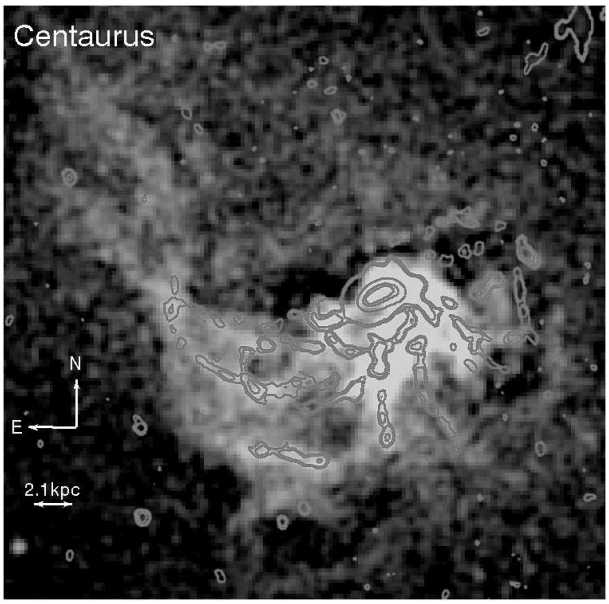

Figure 2. Contours of Hα emission from NGC 4696 overlaid on a soft X-ray image of the core of the Centaurus cluster. X-ray data from (Fabian et al., 2005a). The Hα filaments that spiral east from the central galaxy have spatially associated soft X-ray emission. The filaments are X-ray bright rather than UV bright (unlike the Perseus cluster core).

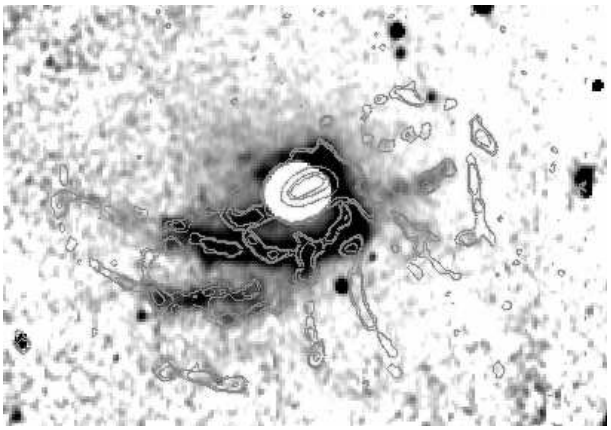

Figure 3. Contours of Hα emission from NGC 4696 in the Centaurus cluster overlaid on B-I greyscale indicating presence of dust. North is up, east is right. The two filaments stretching east from the central galaxy show correlations with strong dust features, as does a shorter filament that stretches west across the ring of Hα emission surrounding the radio bubble. The ring itself does not correlate with any clear dust features.

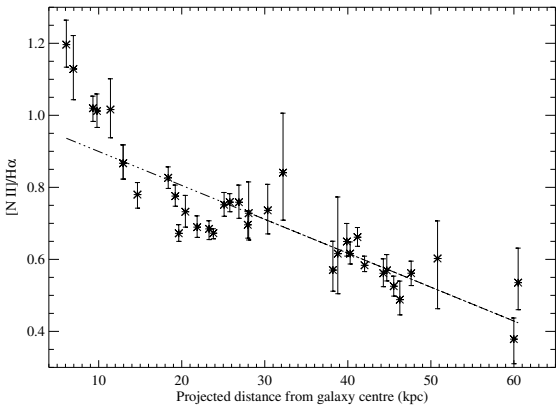

Figure 4. [NII]λ6584/Hα line intensity ratio against projected distance from the core of NGC 1275. The clear radial gradient is difficult to produce from metallicity variations alone, therefore the correlation implies the excitation of the nebula gas is connected to the global properties of the surrounding intracluster medium.

The direct spatial correlation between the optical line-emitting gas and the soft X-ray emission implies an energy exchange between the nebula gas and the surrounding intracluster medium. The intracluster medium that surrounds the central galaxy is very hot, having a temperature greater than 10^7 K, whereas the temperature of the ionized optical and UV line-emitting gas is cooler at $\sim 10^4$ K. Such large temperature gradients may cause conduction to be an efficient heat transport mechanism. Conduction could transfer heat to the optical nebula from the intracluster medium where there is enough energy to ionize the extended nebula (Sparks et al., 2004). Alternatively the energy exchange can be due to a mixing process which would produce the same features (Fabian et al., 2005b). Whilst both the Perseus and Centaurus cluster cores have soft X-ray emission associated with some of the optical line-emitting filaments, the soft X-ray luminosity of the Perseus filaments is only a few per cent of the total optical and UV line-emission luminosity, whereas the Centaurus filaments are twice as luminous in soft X-rays compared to optical and UV line-emission. Neither of these values have been corrected for intrinsic absorption, therefore this variation may be due to the large dust content of the Centaurus nebula reducing the observed Hα flux relative to the X-ray flux. The dusty regions (spiral features) exhibit strong soft X-ray emission, whereas the regions apparently free from large quantities of dust (western ring) do not exhibit strong X-ray emission.

Whilst the process by which the nebula interacts with the intracluster medium is uncertain, it is probable that the nebula cools the intracluster medium in its vicinity, producing the soft X-ray emission observed. The effect of the interaction on the nebula is apparent through the variation in the nebula ionization state. The nebula of NGC 1275 in the Perseus cluster displays a radial variation of the line intensity ratio [NII]λ6584/Hα implying that the intracluster medium affects the excitation of the nebula (see Fig. 4). [NII]λ6584 line emission is produced through collisional excitation, hence is a measure of the thermal energy of the ionized gas, whereas the Hα line intensity is a measure of the ionization rate. Therefore the [NII]/Hα line intensity ratio measures the heat input to the gas per hydrogen ionization. The inner nebula displays emission-line ratios of gas in a very low ionization state, whereas the extended regions display emission-line ratios of a much higher ionization state. The large variation in the [NII]/Hα ratio observed in Perseus is difficult to produce through metallicity variations alone. If the relative abundance of oxygen and nitrogen is fixed, an increase in the total metallicity of the gas reduces the [NII]/Hα ratio. In order to produce the observed range in ratio, there must be a radial increase in oxygen abundance with the largest oxygen fraction at the outer edges of the nebula, whilst the nitrogen abundance must fall. Although a certain process may be able to change the relative abundances in such a way to produce the ratio variation, it seems plausible that the radial gradient in the [NII]λ6584/Hα ratio is a product of an interaction between the nebula and the global properties of the surrounding intracluster medium which vary smoothly (Hatch et al., 2005b).

3. ORIGIN OF THE PERSEUS-NGC 1275 NEBULA

The nebulae surrounding both the Perseus and Centaurus central galaxies have a filamentary morphology, which implies that the intracluster medium cannot be turbulent on scales grater than a few kpcs (Fabian et al., 2003b). On larger scales the emission-line filaments are coupled

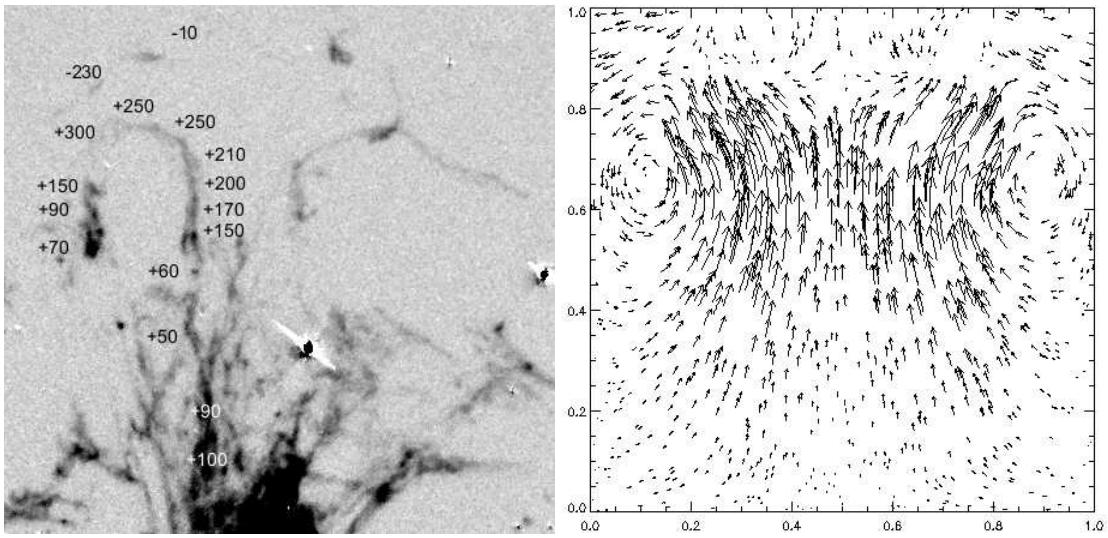

Figure 5. Left: Detail of northwest filaments that lie beneath the ghost bubble. Numbers indicate approximate line-of-sight velocities of the long radial filament. Data from Hatch et al. (2005b). Right: Simulated velocity field of a bubble rising buoyantly through a viscous fluid. Adapted from data of Reynolds et al. (2005)

to the motion of the intracluster medium, therefore they may act as streamlines tracing the bulk flow of the intracluster medium. Fabian et al. (2003b) remark on the similarity of the northwest filaments that lie underneath the ghost bubble to streamlines of flow beneath a spherical cap bubble rising through a fluid. As these ghost bubbles rise they may entrain significant quantities of cool metal-rich intracluster medium from the core (Churazov et al., 2001). The long narrow structure of the filaments suggest that the primary direction of flow is along the filament's length. Doppler shifts of the emission-line gas can be used to measure the velocity field, which can determine whether the filaments have condensed from the intracluster medium and are accreting onto the galaxy, or whether they are galactic gas drawn out from the central galaxy by buoyantly rising ghost bubbles.

Fig. 5 details the heliocentric line-of-sight velocities of the horseshoe shaped filament that lies beneath the northwest ghost cavity. From the bottom of the image, the filament emission is redshifted with a line-of sight velocity of $\sim$+100 kms^{-1} with respect to the central galaxy. The velocity dips slightly before increasing rapidly to $\sim$+250 kms^{-1} further up the filament. The highest velocity occurs on the curved part of the loop, with velocities reaching +300 kms^{-1}. Above the loop (and ghost bubble) lies line-emitting gas which exhibits blueshifted emission with a line-of-sight velocity of -230 kms^{-1}. This flow pattern qualitatively matches the velocity field of simulations made by Reynolds et al. (2005) of a bubble rising through a viscous intracluster medium. The similarities include:

- The velocity of gas within the filament increases with distance from the central galaxy, with the highest velocities occurring directly underneath the rising bubble/ghost cavity
- The gas flow above the bubble is in the opposite direction to gas flow below the bubble
- The short side of the horseshoe loop is blueshifted relative to the long-side of the loop as expected if the gas flows up the long straight side, over the loop and down the short straight side.

Both the morphology and velocity field of these filaments suggest that they were drawn out of the central galaxy by the rise of the northwest ghost bubble. The spherical cap appearance of the ghost bubble, the morphological structure and the low line-of-sight velocities suggest that the northwest filaments are orientated such that they are close to being in the plane of the sky. Within the interpretation that the filaments are entrained by the ghost bubble, the Doppler shifts indicate that the filaments must be orientated slightly away from the observer.

Direct outflow from NGC 1275 in the Perseus cluster can be observed in a 35 kpc long, thin ($<$1 kpc) filament that stretches radially north from the central galaxy (filament marked in Fig. 1). The filament is unlikely to be in projection with another filament as it is the only structure detected so far out from the central galaxy, and we assume the filament is intrinsically straight as it is improbable that we are observing an intrinsically-curved filament at a particular angle such that it appears straight. Fig. 6 details the line-of-sight velocity of the filament. The upper half of the filament (above a projected distance of 40 kpc from the galaxy centre) displays blueshifted emission whereas the lower half displays redshifted emission. As the predominant flow direction is along the filament, the gas in the lower half must be moving in the opposite direction to the gas at the top of the filament. If the filament is orientated toward the observer, the filament will be collapsing. If the filament is orientated away from the

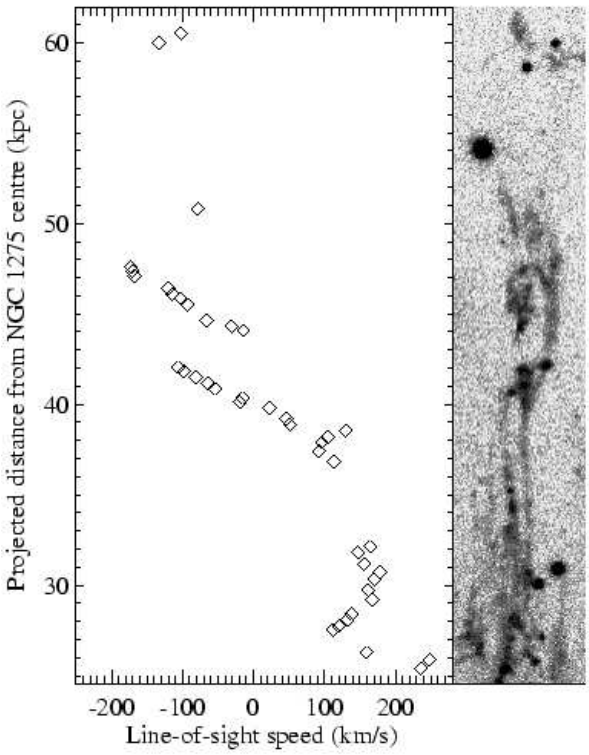

Figure 6. Line-of-sight velocity of the northern filament. Above 40 kpc the filament exhibits blueshifted emission, below 40 kpc, the filament exhibits redshifted emission. Data from Hatch et al. (2005b).

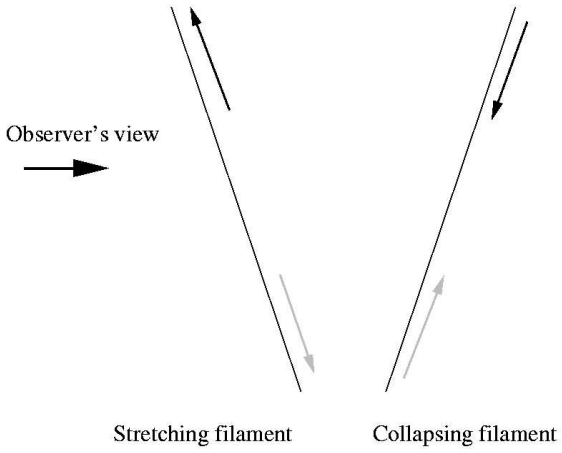

Figure 7. Graphic representing the possible configurations of the northern filament. The bottom of the filament exhibits redshifted lines, the top exhibits blueshifted emission lines. Thus the filament may be stretching or collapsing depending on the orientation. In both scenarios line-emitting gas must have been drawn away from the galaxy.

observer, the filament will be in the process of stretching (see Fig. 7). In both stretching and collapsing scenarios a portion of the filament is flowing away from the central galaxy. In addition to outflowing gas, part of the filament is falling back into the galaxy. These extended nebulae are complex dynamical systems; if the filaments survive in the intracluster medium, we may be observing filaments drawn out from the galaxy over 2 (if not 3; Fabian et al. 2005b) epochs of bubble formation. These filaments may eventually fall back into the galaxy, evaporate due to interactions with the intracluster medium or condense into stellar clusters.

4. SUMMARY

The velocity structure of the northern filament shows that gas more than 30 kpc from the central galaxy is flowing away from the galaxy. The morphology and velocity field of the filaments suggests the most probable dynamical model is one in which the filaments are galactic gas entrained by buoyantly-rising bubbles inflated by the central engine. As the nebula's filaments are coupled to the bulk flow of the intracluster medium on scales larger than a few kpc, the filaments may trace a larger flow of the intracluster medium away from the cluster core.

Direct spatial correlation between the optical line-emitting filaments and soft X-ray emission in both the Perseus and Centaurus cluster cores, imply that an energy exchange is occurring between the two gas phases. Conduction by thermal electrons (Sparks et al., 2004) or mixing (Fabian et al., 2005b) are both possible mechanisms by which the optical nebula can cool the surrounding intracluster medium. Although the mechanism by which the Perseus intracluster medium interacts with the line-emitting nebula is uncertain, the radial gradient in the [NII]/Hα line intensity ratio indicates a possible link between the global properties of the intracluster medium and the ionization state of the nebula gas.

ACKNOWLEDGEMENTS

NAH and RMJ acknowledge support from PPARC and ACF and CSC thank the Royal Society for support.

REFERENCES

Burns J. O., 1990, AJ, 99, 14

Churazov E., Brüggen M., Kaiser C. R., Böhringer H., Forman W., 2001, ApJ, 554, 261

Conselice C. J., Gallagher J. S., Wyse R. F. G., 2001, AJ, 122, 2281

Crawford C. S., Allen S. W., Ebeling H., Edge A. C., Fabian A. C., 1999, MNRAS, 306, 857

Crawford C. S., Hatch N. A., Fabian A. C., Sanders J. S., 2005, MNRAS, 363, 216

Donahue M., Mack J., Voit G. M., Sparks W., Elston R., Maloney P. R., 2000, ApJ, 545, 670

Edge A. C., 2001, MNRAS, 328, 762

Edge A. C., Wilman R. J., Johnstone R. M., Crawford C. S., Fabian A. C., Allen S. W., 2002, MNRAS, 337, 49

Fabian A. C., Sanders J. S., Allen S. W., Crawford C. S., Iwasawa K., Johnstone R. M., Schmidt R. W., Taylor G. B., 2003a, MNRAS, 344, L43

Fabian A. C., Sanders J. S., Crawford C. S., Conselice C. J., Gallagher J. S., Wyse R. F. G., 2003b, MNRAS, 344, L48

Fabian A. C., Sanders J. S., Ettori S., Taylor G. B., Allen S. W., Crawford C. S., Iwasawa K., Johnstone R. M., 2001, MNRAS, 321, L33

Fabian A. C., Sanders J. S., Taylor G. B., Allen S. W., 2005a, MNRAS, 360, L20

Fabian A. C., Sanders J. S., Taylor G. B., Allen S. W., Crawford C. S., Johnstone R. M., Iwasawa K., 2005b, preprint, astro-ph/051047

Hatch N. A., Crawford C. S., Fabian A. C., Johnstone R. M., 2005a, MNRAS, 358, 765

Hatch N. A., Crawford C. S., Johnstone R. M., Fabian A. C., 2005b, MNRAS, submitted

Heckman T. M., Baum S. A., van Breugel W. J. M., McCarthy P., 1989, ApJ, 338, 48

Hu E. M., Cowie L. L., Wang Z., 1985, ApJS, 59, 447

Reynolds C. S., McKernan B., Fabian A. C., Stone J. M., Vernaleo J. C., 2005, MNRAS, 357, 242

Sanders J. S., Fabian A. C., 2002, MNRAS, 331, 273

Sparks W. B., Donahue M., Jordán A., Ferrarese L., Côté P., 2004, ApJ, 607, 294

GAS ENTROPY IN NEARBY GALAXY CLUSTERS

G.W. Pratt[1], M. Arnaud[2], and E. Pointecouteau[3]

[1]MPE Garching, Giessenbachstraße, Garching, Germany
[2]CEA/Saclay Service d'Astrophysique, L'Orme des Merisiers, Bât. 709, 91191 Gif-sur-Yvette Cedex, France
[3]CEA/Saclay Service d'Astrophysique & Astrophysics, University of Oxford, Keble Road, Oxford OX1 3RH, UK

ABSTRACT

We investigate the scaling properties of the ICM entropy using *XMM-Newton* observations of a sample of ten nearby ($z < 0.2$) galaxy clusters covering a decade in mass ($\sim 10^{14} - 10^{15}\,M_{\odot}$). We examine the scaling properties of the entropy with system temperature, and explore the structural properties of the scaled entropy profiles. We discuss our results in the context of the effect of non-gravitational processes on observed cluster X-ray properties.

Key words: Cosmology: observations, Galaxies: cluster: general, (Galaxies) Intergalactic medium, X-rays: galaxies: clusters.

1. INTRODUCTION

Observations of the entropy of the hot, X-ray emitting intracluster medium (ICM) of galaxy clusters are fundamental for understanding the thermodynamic history of the gas. Entropy is generated in shocks as the gas is drawn into the potential well of the cluster halo, thus the quantity reflects the accretion history of the ICM. However, the entropy distribution also preserves key information regarding the influence and effect of non-gravitation processes on the properties of the ICM.

Observations with *ROSAT* and *ASCA* indicated an excess in entropy in the coolest systems at $0.1R_{200}$ (hereafter $S_{0.1}$). The entropy at that radius is considerably higher than that available from gravitational collapse (Ponman et al., 1999; Lloyd-Davies et al., 2000), leading to a shallower entropy-temperature (S–T) relation than expected. More recent spatially resolved entropy profiles indicate that the entropy is higher *throughout* the ICM, and that, outside the core regions, entropy profiles are structurally similar (Ponman et al., 2003; Voit & Ponman, 2003; Pratt & Arnaud, 2003, 2005; Piffareti et al., 2005). At the same time the scatter in $S_{0.1}$ at a given temperature can be up to a factor of three (Ponman et al., 2003).

Preheating, where the gas has been heated before being accreted into the potential well, by early supernovae and/or AGN activity (e.g., Kaiser, 1991; Evrard & Henry, 1991; Valageas & Silk, 1999), internal heating after accretion (e.g., Metzler & Evrard, 1994), and cooling (e.g., Pearce et al., 2000) can all have different effects on the structure and scaling of the entropy in clusters. The lack of isentropic core entropy profiles in groups and poor clusters has shown that simple preheating is unlikely to be the sole explanation of the observations (Ponman et al., 2003; Pratt & Arnaud, 2003, 2005). Since cooling-only models generally predict a higher stellar mass fraction than observed (e.g., Muanwong et al., 2002), attention is now focussing on the interplay between cooling and feedback. Further high quality observations are needed in order to distinguish between these different entropy modification mechanisms.

Here we present a summary of results from *XMM-Newton* observations of ten nearby morphologically relaxed systems: A1983 (z = 0.0442), A2717 (z = 0.0498), MKW9 (z = 0.0382), A1991 (z = 0.0586), A2597 (z = 0.0852), A1068 (z = 0.1375), A1413 (z = 0.1427), A478 (z = 0.0881), PKS0745-191 (z = 0.102) and A2204 (z = 0.1523). Full results can be found in Pratt et al. (2006) (astro-ph/0508234).

2. RESULTS

2.1. Entropy scaling

In Fig 1, the entropy profiles are shown plotted in terms of the measured virial radius, R_{200} (see Pointecouteau et al. 2005 for details). All profiles increase monotonically with radius and, while the slope of the profile becomes shallower towards the centre in some of the clusters, none shows an isentropic core.

Estimating the entropy at various fractions (0.1, 0.2, 0.3 and 0.5) of the virial radius, we plot in Figure 2 the relation between entropy and global temperature. A power-law fit to the data at each radius yields the results shown

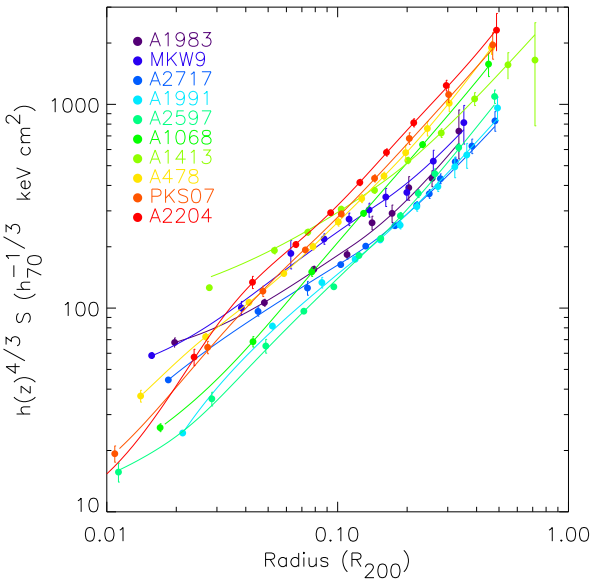

Figure 1. *Cluster entropy profiles obtained from the deprojected, PSF corrected temperature profiles and the best fitting analytical model for the gas density. Solid lines, included to improve visibility, are entropy profiles obtained from analytic model fits to the temperature and density information.*

Table 1. *The S–T relation. Data were fitted with a power-law of the form* $h(z)^{4/3}\ S = A\times(kT/5\mathrm{keV})^{\alpha}$, *where* kT *is the overall spectroscopic temperature in the* $0.1-0.5\ R_{200}$ *region. Errors in entropy and temperature are taken into account. Results are given BCES regression method (see text). Statistical and intrinsic scatter about the best fitting relation in the log-log plane are given in the last columns.*

Radius	A	α	σ_{log}	
R_{200}	keV cm^{-2}		stat	int
BCES				
0.1	230 ± 17	0.49 ± 0.15	0.082	0.076
0.2	485 ± 22	0.62 ± 0.11	0.063	0.052
0.3	798 ± 44	0.64 ± 0.11	0.078	0.065
0.5	1560 ± 83	0.62 ± 0.08	0.074	-

in Table 1. The slope of the entropy-temperature relation is incompatible with the standard self-similar prediction at all radii at which we have measured it, confirming the results of Ponman et al. (2003). The slope of the $S_{0.3}$-T relation, obtained using the BCES method, is $S_{0.3} \propto T^{0.64\pm0.11}$, in excellent agreement with that found by Ponman et al. (2003). Figure 2 shows that there is noticeable scatter about the S–T relation at $0.1\,R_{200}$. Table 1 makes clear that the scatter is reduced at larger scaled radius. The intrinsic scatter remains the dominant contributor to the dispersion in all relations, except at $0.5\ R_{200}$.

2.2. Entropy structure

In Fig. 3 we show the profiles scaled using the relation $S \propto h(z)^{-4/3}\,T_{10}^{0.65}$, where T_{10} is the global temperature measured in units of 10 keV. This relation is consistent

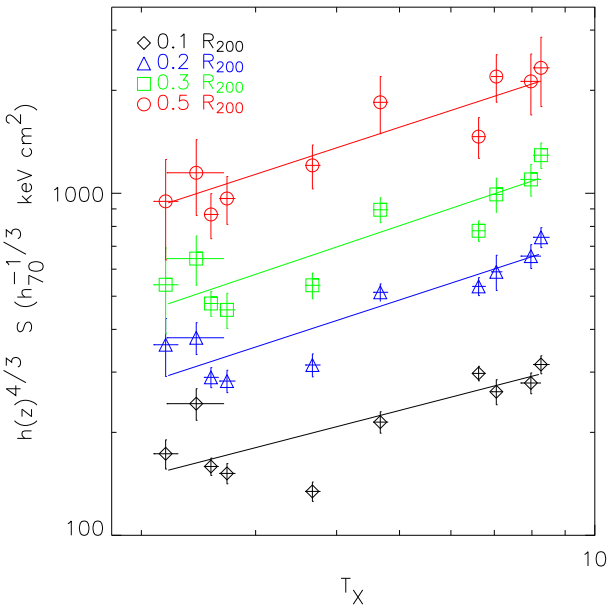

Figure 2. *The S-T relation measured from a sample of 10 clusters covering a temperature range from 2 to 9 keV. The S-T relation is shown for different fractions of* R_{200}. *Measurements are plotted with error bars. At each radius, the best-fitting power-law relation, derived taking account the errors in entropy and temperature, is overplotted; slopes and intercepts are given in Table 1.*

with our data (Table 1), and allows us to compare our results with previous work. As an initial measure of the scatter in scaled entropy profiles, we estimated the dispersion at various radii in the range 0.02–$0.45\,R_{200}$. The shaded area in Fig 3 shows the region enclosed by the mean plus/minus the 1σ standard deviation. Figure 3 shows that, outside the core regions, the entropy profiles present a high degree of self-similarity. The relative dispersion in scaled profiles remains approximately constant at $\lesssim 20$ per cent for $r \gtrsim 0.1\,R_{200}$, in excellent agreement with the dispersion found in a smaller subsample by Pratt & Arnaud (2005). In the core regions, however, the dispersion increases with decreasing radius to reach $\gtrsim 60$ per cent at $\sim 0.02\,R_{200}$.

Fitting the scaled profiles with a power law using the BCES method in the radial range $r \geq 0.01\,R_{200}$ we find a slope of 1.08 ± 0.04, with a dispersion of $\sim$ 30 per cent about the best fitting line. The slope is not significantly changed (1.14 ± 0.06) if the data are fitted in the radial range $r \geq 0.1\,R_{200}$, but the intrinsic dispersion is two times smaller (14 per cent).

3. DISCUSSION

Our results put into evidence two main departures from the standard self-similar model of cluster formation. First, beyond the core region ($r \gtrsim 0.1\,R_{200}$) the entropy profiles obey self-similarity, having a shape consistent with expectations, but with a modified temperature (or

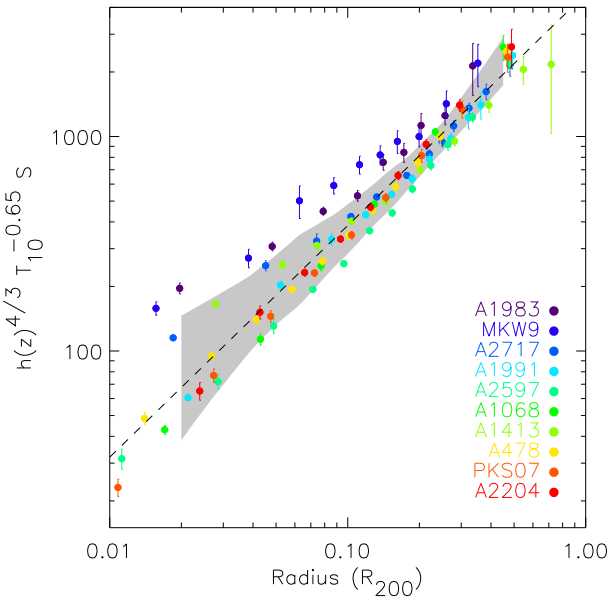

Figure 3. *Scaled entropy profiles. The radius is scaled to R_{200} measured from the best-fitting mass models. The entropy is scaled using the empirical entropy scaling $S \propto h(z)^{-4/3} T_{10}^{0.65}$, using the global temperature in units of 10 keV. The shaded grey area corresponds to the region enclosed by the mean plus/minus the 1σ standard deviation. The dashed line denotes $S \propto R^{1.08}$.*

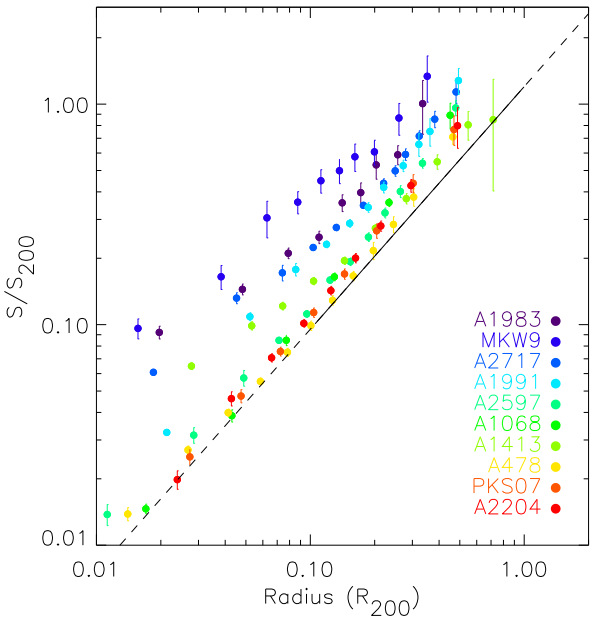

Figure 4. *A comparison of our observed entropy profiles with the prediction from the adiabatic numerical simulations of Voit (2005). The observed entropy profiles have been scaled to S_{200} using Equation 1. The solid line represents the best-fitting power law relation found by Voit (2005) from fitting adiabatic numerical simulations of 30 clusters in the radial range $0.1 < R_{200} < 1.0$.*

mass) scaling. The scaling relations are shallower than expected. Second, there is a break of similarity in the core region: the dispersion in scaled profiles increases with decreasing radius.

3.1. Entropy normalisation

The modified entropy scaling indicates that there is an excess of entropy in low mass objects *relative* to more massive systems, as compared to the expectation from pure shock heating. A comparison with adiabatic numerical simulations allows us to quantify the *absolute* value of the excess and to examine whether an entropy excess is also present for the most massive systems. Voit (2005) shows the results of adiabatic numerical simulations of 30 clusters spanning a mass range of more than a factor of ten. Once scaled by the characteristic entropy of the halo S_{200}, the simulated profiles are closely self-similar, and can be well fitted in the radial range $\sim 0.1 - 1.0\ R_{200}$ by the power-law relation $S/S_{200} = 1.26(R/R_{200})^{1.1}$. Assuming $f_b = 0.14$ ($\Omega_b h^2 = 0.02$ and $\Omega_m = 0.3$) and typical elemental abundances, we can scale our observed entropy values to S_{200} using the expression

$$S/S_{200} = \left(\frac{S}{2471\ \mathrm{keVcm}^2}\right)\left(\frac{M_{200}}{1\times 15 M_\odot}\right)^{-2/3} h(z)^{2/3}. \quad (1)$$

Further scaling the radius by the measured value of R_{200} allows us to compare our results directly with the adiabatic simulations. In Figure 4, our observed entropy profiles are compared with the prediction of Voit (2005).

The richer systems all have entropies which are in good agreement (both in slope and normalisation) with the adiabatic prediction, denoted by the solid line in Fig. 4. On average, their entropy is only slightly higher than predicted (by $\sim$ 20 per cent), although the effect is not very significant. We recall that there is also a $\sim$ 30 per cent difference in normalisation between the observed M–T relation and that predicted by adiabatic simulations (Arnaud et al., 2005). Interestingly, this corresponds to a $\sim$ 20 per cent entropy excess at a given mass for $T \propto M^{2/3}$. The (slight) excess of entropy in massive systems is thus consistent with a simple increase of the mean temperature, i.e., of the internal energy of the ICM. However, Fig. 4 shows explicitly that the poorer systems have a systematically higher entropy normalisation than the richer systems. There is approximately 2.5 times more entropy at $0.2\,R_{200}$ in the ICM of A1983, the poorest cluster in our sample, than that predicted by gravitational heating. This excess shows that the density of the ICM is also affected at lower mass.

Voit et al. (2003) and Ponman et al. (2003) independently noted that the ICM entropy is highly sensitive to the density of the incoming gas and suggested that a smoothing of the gas density due to pre-heating in filaments and/or infalling groups would boost the entropy production at the accretion shock. Recent numerical simulations which mimic preheating by imposing a minimum entropy floor at high z have confirmed the entropy amplification effect

due to smooth accretion (Borgani et al., 2005). However, the effect seems to be substantially reduced when cooling is also taken into account. Furthermore, the physical origin of the preheating is still unclear.

3.2. Localised modification

The adiabatic numerical simulations of Voit (2005) show both a flattening of the slope and an increase in the dispersion of the scaled entropy profiles in the central regions ($< 0.1\ R_{200}$). However, the dispersion in our observed profiles (~ 60 per cent) greatly exceeds that of the simulations (~ 30 per cent, cf Fig. 4 and Fig. 11 of Voit 2005). Six clusters out of our total sample of ten (A1991, A2597, A1068, A478, PKS0745 and A2204) have remarkably similar scaled entropy profiles, displaying power-law behaviour down to the smallest radii measured. These six clusters all appear to host a bona fide cooling core, each having a central temperature decrement of a factor ~ 2. Strong radiative cooling thus appears to generate entropy profiles which display power-law behaviour down to very small radii (Fig. 4).

The other four clusters in our sample are characterised by a smaller central temperature decrement, larger cooling times and shallower entropy profiles. Clearly, some mechanism has modified the cooling history of these clusters. Energy input from AGN is regularly invoked as a way of moderating cooling at the centres of galaxy clusters. Our sample contains four clusters which have X-ray evidence for interactions between radio and X-ray plasma (A478, A2204, A2597, and PKS0745), and yet the entropy profiles of all of these clusters increase monotonically outward in the canonical fashion. It is possible that the heating is distributed via e.g., weak shocks (Fabian et al., 2003), thus preserving the generally increasing form of the entropy profile.

Merging events can result in substantial mixing of high and low entropy gas. Such redistribution of entropy will depend on the scale of the merger, whether the merger has disrupted the structure of the cool core, and the timescale for re-establishment of the cool core if disrupted. In the current sample MKW9, A2717, A1413 and A1983 all have flatter core entropy profiles. We note that the morphological information for the present sample would argue against recent merger activity in these clusters (Pratt & Arnaud 2005; Arnaud et al. 2005; Pointecouteau et al. 2005). However, this does not rule out entropy modification due to a more ancient merger, particularly if the relaxation time is less than the cooling time.

These will be interesting questions to address with numerical simulations. On the observational side, comparison with a larger, unbiased, sample of clusters is ongoing.

ACKNOWLEDGMENTS

GWP thanks E. Belsole and J.P. Henry for useful discussions, and acknowledges funding from a Marie Curie Intra-European Fellowship under the FP6 programme (Contract No. MEIF-CT-2003-500915). EP acknowledges the financial support of CNES, the French Space Agency, and of the Leverhulme trust (UK).

REFERENCES

Arnaud, M., Pointecouteau, E., Pratt, G.W., 2005, A&A, 441, 893

Borgani, S., Finoguenov, A., Kay, S.T., Ponman, T.J., Springel, V., Tozzi, P., Voit, G.M., 2005, MNRAS, 361, 233

Evrard A.E., Henry J.P, 1991, ApJ, 383, 95

Fabian, A.C., Sanders, J.S., Allen, S.W., Crawford, C.S., Iwasawa, K., Johnstone, R.M., Schmidt, R.W., Taylor, G.B., 2003, MNRAS, 344, L43

Kaiser, N. 1991, ApJ, 383, 104

Lloyd-Davies E.J., Ponman, T.J., Cannon, D.B., 2000, MNRAS, 315, 689

Metzler, C.A., Evrard, A.E., 1994, ApJ, 437, 564

Muanwong, O., Thomas, P.A., Kay, S.T., & Pearce, F.R. 2002, MNRAS, 336, 527

Pearce, F.R., Thomas, P.A., Couchman, H.M.P., Edge, A.C., 2000, MNRAS, 317, 1029

Piffaretti, R., Jetzer, P., Kaastra, J.S., Tamura, T., 2005, A&A, 433, 101

Pointecouteau, E., Arnaud, M., Pratt, G.W., 2005, A&A, 435, 1

Ponman, T.J., Cannon, D.B., Navarro, J.F., 1999, Nature, 397, 135

Ponman, T.J., Sanderson, A.J.R., Finoguenov, A., 2003, MNRAS, 343, 331

Pratt, G.W., Arnaud, M., 2003, A&A, 408, 1

Pratt, G.W., Arnaud, M., 2005, A&A, 429, 791

Pratt, G.W., Arnaud, M., & Pointecouteau, E. 2006, A&A, in press (astro-ph/0508234)

Valageas, P., & Silk, J. 1999, A&A 347,1

Voit, G.M., Balogh, M.L., Bower, R.G., Lacey, C.G., Bryan, G.L., 2003, ApJ, 593, 272

Voit, G.M., Ponman, T.J., 2003, ApJ, 594, L75

Voit, G.M. 2005, Rev. Mod. Phys., 77, 207

TEMPERATURE AND ENTROPY PROFILES OF NEARBY COOLING FLOW CLUSTERS OBSERVED WITH XMM-NEWTON AND THE EFFERVESCENT HEATING MODEL

R. Piffaretti[1], J. S. Kaastra[2], Ph. Jetzer[3], and T. Tamura[4]

[1]Institute for Astrophysics, Leopold-Franzens University of Innsbruck, Technikerstraße 25, A-6020 Innsbruck, Austria
[2]SRON National Institute for Space Research, Sorbonnelaan 2, 3584 CA Utrecht, The Netherlands
[3]Institute of Theoretical Physics, University of Zürich, Winterthurerstrasse, 190, CH-8057 Zürich, Switzerland
[4]Institute of Space and Astronautical Science, 3-1-1 Yoshinodai, Sagamihara, Kanagawa 229-8510, Japan

ABSTRACT

We present temperature and entropy profiles of 13 nearby cooling flow clusters observed with *XMM-Newton*. When normalized and scaled by the virial radius the temperature profiles turn out to be remarkably similar and at large radii the temperature profiles show a clear decline. The entropy S of the plasma increases monotonically moving outwards almost proportional to the radius. The dispersion in the entropy profiles is smaller if the empirical relation $S \propto T^{0.65}$ is used instead of the standard self-similar relation $S \propto T$ and no entropy cores are observed. In addition to these results we present recent observational constraints on the "effervescent heating" model derived from *XMM-Newton* observations of 16 cooling flow clusters.

Key words: ESA; X-rays; Cluster of galaxies; cooling flows.

1. INTRODUCTION

Temperature and entropy profiles of the X-ray-emitting intracluster medium (ICM) provide crucial information on the thermodynamic history of the plasma and the comparison between observed profiles and theoretical predictions is an essential test for any model of structure formation of groups and clusters of galaxies. Cooling flow (CF) clusters are of particular interest: gas cooling is of great importance in their cores, since the gas is dense enough to radiate an amount of energy equal to its thermal energy in less than a billion years. *XMM-Newton* observations have greatly improved our understanding of CF clusters. In Sects. 2 and 3 we show results from spatially resolved spectroscopy for a sample of nearby CF clusters observed with *XMM-Newton* and comment on the shape of temperature and entropy radial profiles, respectively. *XMM-Newton* spectra failed to detect the emission lines that dominate the emission from gas below 2 keV (e.g., Peterson et al. (2003)), therefore ruling out the standard CF model. Spatially resolved spectroscopy shows that the temperature in CF clusters drops towards the center to approximatively one third of the cluster mean temperature, indicating that the gas is prevented from cooling below these cutoff temperatures (Kaastra et al. (2004) and Sect. 2). This recent evidence of lack of cool gas shows that the dynamics of the ICM in CF clusters in not solely governed by cooling of the ICM and that some heating mechanisms must be investigated. Recent observations of the interaction between active galactic nuclei (AGN) at the center of CF clusters with the surrounding gas (i.e., Blanton (2004)), has motivated the development of models incorporating AGN feedback. Ruszkowski & Begelman (2002) (RB02, hereafter) have recently proposed such a model, which in addition to AGN heating incorporates heating by thermal conduction. In Sect. 4 we investigate whether RB02's model (or effervescent heating model, hereafter) can provide a satisfactory explanation of the observed structure of CF clusters using *XMM-Newton* observations.

2. TEMPERATURE PROFILES

Various observational studies have found different and conflicting results regarding temperature gradients in the outer regions of galaxy clusters. In Piffaretti et al. (2005) we have investigated temperature profiles of 17 cooling flow clusters using the results from the spatially resolved spectra taken with the EPIC cameras of *XMM-Newton* (Kaastra et al. (2004)). In Fig. 1, we present the deprojected radial profiles of 13 clusters plotted against the radius in units of $r_{\rm vir}$ ($\approx r_{101}$ for ΛCDM cosmology at $z = 0$), where the temperature has been normalized by the mean emission-weighted temperature $< T_{\rm X} >$. The virial radius has been computed from the mass profile determined through the assumption of hydrostatic equilibrium and spherical symmetry. For 4 objects (Virgo, MKW 9, Hydra A and A 399) this estimate is not possible and therefore their scaled profiles are not presented.

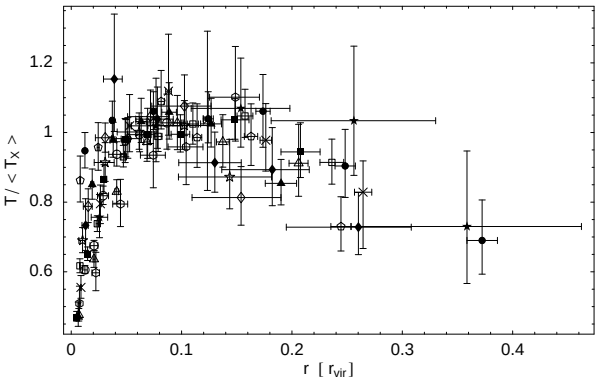

Figure 1. Scaled temperature profiles (deprojected) in a ΛCDM70 cosmology ($\Omega_{\rm m} = 0.3$, $\Omega_\Lambda = 0.7$, with $H_0 = 70\ km\,s^{-1}\,Mpc^{-1}$). The radius is scaled with the virial radius $r_{\rm vir}$, while the temperature is normalized by the mean emission-weighted temperature $< T_{\rm X} >$. Clusters are related to symbols as follows: NGC 533 (crosses), A 262 (filled squares), A 1837 (filled diamonds), Sérsic 159−3 (filled circles), 2A 0335+096 (open triangles), MKW 3s (open pentagons), A 2052 (filled triangles), A 4059 (open diamonds), A 496 (open hexagon), A 3112 (open stars), A 1795 (open squares), Perseus (open circles) and A 1835 (filled stars).

From a visual inspection of Fig. 1 it is evident that a temperature gradient is present at large radii and that when normalized and scaled by the virial radius, temperature profiles are remarkably similar. The individual profiles clearly show a break radius $r_{\rm br}$, a decrease of temperature from $r_{\rm br}$ inwards typical of CF clusters, and the decline at radii larger than $r_{\rm br}$. We have measured the break radius in units of the virial radius for each individual object and we find a mean value $r_{\rm br} \sim 0.09\, r_{\rm vir}$ with a standard deviation of 0.01. We have compared our scaled profiles with the results of Markevitch et al. (1998), De Grandi & Molendi (2002) and Vikhlinin et al. (2005), since these are studies which used fairly large samples and a scaling procedure similar to ours, and found good agreement. The size of our sample, along with the good temperature determination within the cooling radius, allows us to study the shape of the profiles in this region. We have modeled the central temperature drop using:

$$T(r) = T_c + (T_h - T_c)\frac{(r/r_{\rm c})^2}{1 + (r/r_{\rm c})^2}, \qquad (1)$$

with $T_{\rm c}$ set equal to the temperature of the innermost bin. We have fitted each individual and determined the best fit parameters $T_{\rm h}$ and $r_{\rm c}$. A correlation between the fitting parameters of the form $r_c \propto T_h^{1.84\pm0.14}$, with r_c in kpc and T_h in keV, is found. Assuming that r_Δ scales with $T_h^{1/2}$ (i.e., the size-temperature relation, since T_h is equivalent to the cluster mean temperature) one concludes that the characteristic radius r_c, and therefore the temperature profile, does not simply scale with the virial radius of the cluster.

3. ENTROPY PROFILES

The ICM entropy distribution has been shown to be a very powerful tool to study non-gravitational processes such as radiative cooling, preheating and feedback from supernovae and active galactic nuclei (e.g., Voit (2004)).
For our sample of CF clusters we have derived entropy profiles and studied they scaling properties (Piffaretti et al. (2005)). We define the entropy as $S = kT/n_{\rm e}^{2/3}$, where T and $n_{\rm e}$ are the deprojected electron temperature and density, respectively. In the standard self-similar scenario, one predicts $S \propto h^{-4/3}(z)\,T$, where $h^2(z) = \Omega_{\rm m}(1+z)^3 + \Omega_\Lambda$. On the other hand, recent results by Ponman et al. (2003) suggest that entropy scales with temperature as $S \propto T^{0.65}$, the so-called "entropy ramp", instead of $S \propto T$. While both scalings $S \propto h^{-4/3}(z)\,T$ and $S \propto h^{-4/3}(z)\,T^{0.65}$ considerably reduce the dispersion of the profiles, we investigated which of these scalings reduces it the most. Using $r_{\rm vir}$ to scale radii, we quantify the dispersion of the scaled profiles using the standard deviation and the mean of the scaled entropy values at a fixed scaled radius. As mean cluster temperature T, we use the mean emission-weighted temperature. The scaled entropy values are evaluated at fractions of $r_{\rm vir}$ for which no extrapolation is needed and we compute the ratio between their standard deviation σ and mean m to quantify the relative dispersion of the scaled profiles. We find that the dispersion is less if the "entropy ramp" scaling is used: $\sigma/m = 0.37$ and $\sigma/m = 0.29$ at $0.1 r_{\rm vir}$ for the $S \propto T$ and $S \propto T^{0.65}$ temperature scaling, respectively. This result does not depend on the fraction of the virial radius at which the entropy is determined and the adopted cosmology. In Fig. 2 we show entropy profiles scaled according to the "entropy ramp" relation. We fit these data with a line in log-log space (with errors in both coordinates) and find, in excellent agreement with the value found by Pratt & Arnaud (2005), a slope equal to 0.95 ± 0.02. Similarly, using *Chandra* data, Ettori et al. (2002) find a slope equal to 0.97 for the entropy profile of A 1795. Therefore, our analysis gives additional evidence for a slope close to, but slightly shallower than 1.1, the value predicted by shock dominated spherical collapse models (Tozzi & Norman (2001)). The normalization of the S-T relation we derive from the scaling of the entropy profiles is in excellent agreement with the one found by Ponman et al. (2003). Pratt et al. (2005) (see G. Pratt's proceedings of this conference), using a complementary sample of 10 nearby relaxed clusters, presented results on entropy profiles and their scaling properties in excellent agreement with ours.

4. HEATING COOLING CORES

The lack of evidence for cool gas below approximatively one third of the cluster mean temperature has motivated the development of many CF heating models. AGN heating is the most appealing candidate. In fact, most of CF clusters host an AGN with strong radio activity at their

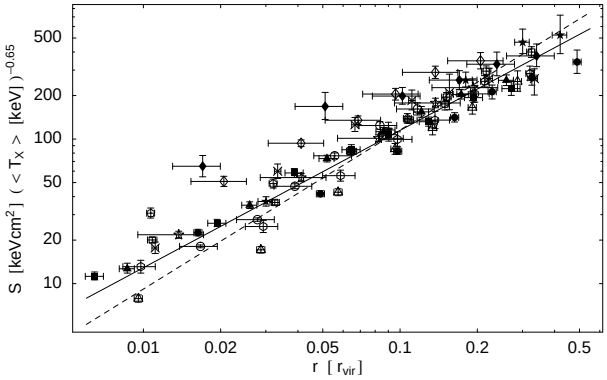

Figure 2. Entropy profiles in a SCDM50 cosmology ($\Omega_{\rm m} = 1$ with $H_0 = 50$ km s^{-1} Mpc^{-1}). The radius is scaled with the radius $r_{\rm vir}$, while the scaling $S \propto h^{-4/3}(z)\,T^{0.65}$ has been applied to the entropy values. Clusters are related to symbols as in Fig. 1. The solid line indicates the best fit power-law (best fit power index 0.95) and the dashed one the best fit power-law with the power index value fixed to 1.1, i.e. the value predicted by shock dominated spherical collapse models.

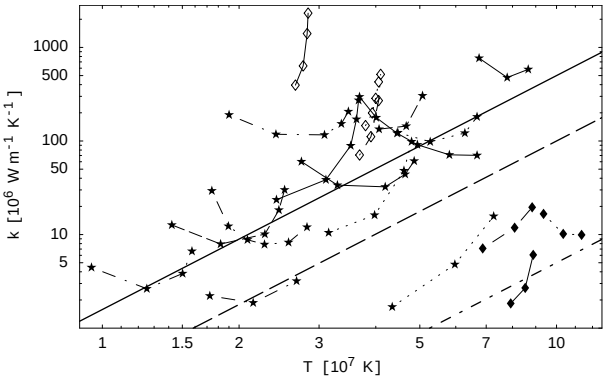

Figure 3. The conduction coefficients κ required for heat conduction to balance radiation losses as a function of temperature. The solid line is the Spitzer conductivity, the dashed lines are one fifth and one hundredth of the Spitzer conductivity, respectively. Filled diamonds represent the values for the three clusters without cooling flow (Coma, A 3266 and A 754), while open diamonds represent the values for the clusters with a shallow temperature profile (MKW 3s, Sérsic 159-3 and Hydra A). Filled stars represent the remaining clusters. Values for the same cluster are joined by a line and values are given only for bins with cooling times less than ∼30 Gyr.

centers and, most important, recent observations show that these radio sources are interacting with the ICM and are often displacing the hot gas leaving cavities in their wakes. The class of models in which the AGN energy input alone balances radiative losses is however thought to be unable to quench the CF (Brighenti & Mathews (2002); Zakamska & Narayan (2003)). Thermal conduction by electrons might also play a very important role in CFs. In Kaastra et al. (2004) we have computed, using the sample of 17 CF clusters mentioned above and in addition for 3 non-CF cluster (Coma, A 3266 and A 754), the conduction coefficients κ required to balance radiative losses completely. Our estimates of the conduction coefficients κ are shown in Fig. 3. The estimated conduction coefficients must be compared to theoretical calculations to see whether heat conduction from the outer regions can totally balance radiative losses. For a highly ionized plasma such as the ICM, the maximum rate is expected to be the Spitzer conductivity:

$$\kappa_S = \frac{1.84 \times 10^{-5}\,(T)^{5/2}}{\ln\Lambda}\,\mathrm{erg\,cm^{-1}\,s^{-1}\,K^{-1}}\,, \quad (2)$$

where $\ln\Lambda \sim 40$ is the Coulomb logarithm. In the presence of a homogeneous magnetic field, the conductivity is the Spitzer rate only along the field, but severely decreased in the transverse direction. The suppression of conductivity below the Spitzer rate, which can be written as $\kappa = f_c \times \kappa_S$, therefore depends on the strength and topology of the magnetic field. For tangled magnetic field at the level observed in CF clusters thermal conductivity is below the Spitzer level by a factor of order 10^2 to 10^3, depending on the assumed field tangling scale. Conductivity is less severely decreased if the magnetic field behaves chaotically over a wide range of scales: Narayan & Medvedev (2001) estimate that in this case conductivity is only a factor ∼5 below the Spitzer rate and Gruzinov (2002) pointed out that the effective heat conduction in a random variable magnetic field is boosted to a factor of 3 below the Spitzer value. In Fig. 3 we therefore show the Spitzer conductivity $\kappa_{\rm S}$, $\kappa_{\rm S}/5$ and $\kappa_{\rm S}/100$ for comparison. For the three non cooling clusters we find very low values for the conductivity coefficients: the absence of significant cooling allows even inefficient heat conduction to remove temperature inhomogeneities. For the cooling clusters we see that clusters with shallow temperature profile show a very different trend and relatively high conductivity because of the small temperature gradients. Since the thermal conductivity in the ICM is estimated to be below the Spitzer rate by at least a factor of 3-5, we conclude that in general heat conduction alone is insufficient to balance radiative losses in cooling clusters. The exception is the CF cluster A 399 (see the 3 data points in the lower right corner of Fig. 3), where conduction is very efficient, owing to its relatively high temperature and very steep temperature profile. In addition to this observational evidence, it has been shown that models with heat conduction as the only heating source are unstable (Soker (2003)).

While models with either heat conduction or AGN feedback acting as the sole heating source fail in supplying the needed heat to balance radiative cooling losses, models with both these mechanisms acting together are more attractive due to the complementary nature of the two processes: thermal conduction is effective/ineffective in the outer/inner regions of the cluster and AGN heating effective/ineffective in the inner/outer part. Ruszkowski & Begelman (2002) (RB02) have recently proposed such a model. The ICM density and temperature evolved according to their model reach a final stable configuration in agreement with the general shape of observed density and temperature profiles in CF clusters. RB02's model is the

only proposed theoretical model that can be effectively tested against observations. Unfortunately this has only been done for the cluster M87 (Ghizzardi et al. (2004)) and it is not clear whether the model can give a satisfactory explanation to the dynamics of CF clusters in general. In Piffaretti & Kaastra (2005) we have addressed the latter question using our sample of CF clusters observed with *XMM-Newton* (see Table 1 for the objects we used for this analysis). The heating sources present in the effervescent heating model are: AGN feedback, thermal conduction and the energy due to the inflow of the gas. In Piffaretti & Kaastra (2005) we have taken into account all of then, but here we present results for models without gas mass dropout of outflow. In this case, of the thermodynamic equations describing the ICM, only the energy equation is of interest. Assuming spherical symmetry, we have:

$$H = \varepsilon - \varepsilon_{cond}. \tag{3}$$

$\varepsilon = n_{\rm e}^2 \Lambda(T)$ ($n_{\rm e}$ is the electron density and $\Lambda(T)$ the cooling function) is the plasma emissivity and ε_{cond} is the heating due to thermal conduction, which is given by:

$$\varepsilon_{cond} = \frac{1}{r^2}\frac{d}{dr}\left(r^2 \kappa \frac{dT}{dr}\right), \tag{4}$$

where $\kappa = f_c \times \kappa_S$ is the conductivity and T is the gas temperature. As a consequence, H in the energy equation (Eq. 3) is an extra heating term, which, in the effervescent heating model developed in RB02, is provided by buoyant bubbles injected into the ICM by the central AGN.
The suppression of thermal conduction is taken into account by investigating models with thermal conduction varying from zero to the maximum level of $1/3$ times the Spitzer value ($0 \leq f_c \leq 1/3$). The RB02 heating function H^{AGN} can be expressed according to:

$$H^{AGN} = -h(r)\left(\frac{p}{p_0}\right)^{(\gamma_b - 1)/\gamma_b} \frac{1}{r}\frac{d\ln p}{d\ln r}, \tag{5}$$

with

$$h(r) = \frac{L}{4\pi r^2}\left(1 - e^{-r/r_0}\right) q^{-1} \tag{6}$$

and where

$$q = \int_0^{+\infty} \left(\frac{p}{p_0}\right)^{(\gamma_b - 1)/\gamma_b} \frac{1}{r}\frac{d\ln p}{d\ln r}\left(1 - e^{-r/r_0}\right) dr\,. \tag{7}$$

p_0 is some reference ICM pressure (here its value at the cluster center) and L the *time-averaged* luminosity of the central source. The term $1 - \exp(-r/r_0)$ introduces an inner cutoff which fixes the scale radius where the bubbles start rising in the ICM.
From the observed gas temperature and density profiles the required extra heating H can be computed for fixed values of the conduction efficiency f_c and then fitted using the AGN heating function H^{AGN}. For each bin with measured gas density and temperature we compute the gas emissivity ε. The conductive heat ε_{cond} is computed using the temperature profile given in Eq. 1 and then evaluated at the radius where the gas emissivity is computed, to finally obtain, through Eq. 3, the extra heating H.
Finally the AGN heating function given in Eq. 5 is fitted to the extra heating data points using a χ^2 minimization. The gas pressure and pressure gradients in Eq. 5 are evaluated using Eq. 1 and a β-model for the gas density profile. For any fixed f_c parameters are therefore r_0 and the luminosity of the central AGN L. The bubbles adiabatic index γ_b is fixed to $4/3$.
In Fig. 4 we illustrate results for the cluster A 1795 and discuss them in the following, since the model outcome for this object highlights the features also found for most of the clusters in the sample. $f_{\rm c} = 1/3$ is the maximum value we consider and therefore corresponds to the maximum energy yield by heat conduction from the outer parts of the cluster. From a visual inspection of Fig. 4 it is clear that heat conduction is not able to lower the extra heating in the outermost bins. As a consequence, if the extra heating curve is fitted with Eq. 5 the resulting best fit parameter r_0 (the scale radius where the bubbles start rising in the ICM) is unphysically large ($r_0 = 176$ kpc) and the *time-averaged* AGN luminosity $L = 3.3 \times 10^{45}\,{\rm erg\,s^{-1}}$ quite large. On the other hand, if the effervescent heating is assumed to be efficient in the region within the cooling radius only, one can notice that heat conduction is effective in lowering the extra heating so that the resulting extra heating curve is monotonically falling with radius. In this case one therefore expects that the extra heating supplied by the raising relativistic bubbles must be distributed over smaller distances and that the total AGN energy output is lower. This is indeed reflected in the much different best fit parameters $r_0 = 14$ kpc and $L = 8 \times 10^{44}\,{\rm erg\,s^{-1}}$. This feature indicates that, as expected, the effervescent heating model strongly depends on how much and at which radial distance heat conduction is efficient. Therefore, we have performed fits using the whole observed radial range and the radial range delimited by the cooling radius.
Another common feature is the effect of the variation of the conduction efficiency. If $f_{\rm c} = 0$ the extra heating curve is simply equal to the gas emissivity and the increase of $f_{\rm c}$ from 0 to $1/3$ gives a decrease of the extra heating curve from the emissivity curve to the data points marked in Fig. 4. The increase of $f_{\rm c}$ should hence lead to a decrease of the AGN energy requirement. In fact we find that, within the cooling radius, both *time-averaged* AGN luminosity and inner cutoff radius r_0 decrease monotonically with increasing $f_{\rm c}$. This opposite effect is seen if the fits are performed over the whole radial range: an increase of $f_{\rm c}$ leads to an increase in both L and r_0, showing again the inadequacy of applying the model over the whole radial range.
For the majority of the objects in our sample we find that the effervescent heating model provides results when the radial range used to fit the extra heating curve with Eq. 5 is not simply the whole range observed but the radial range inside the cooling region. For A 399 no results are obtained for neither of the two radial ranges. The reason for the lack of convergence of the fits is that in A 399 heat conduction is very efficient, owing to its relatively high temperature and very steep temperature profile. The results for the sample are summarized in Table 1. While for most of the clusters we find a solution for L and r_0

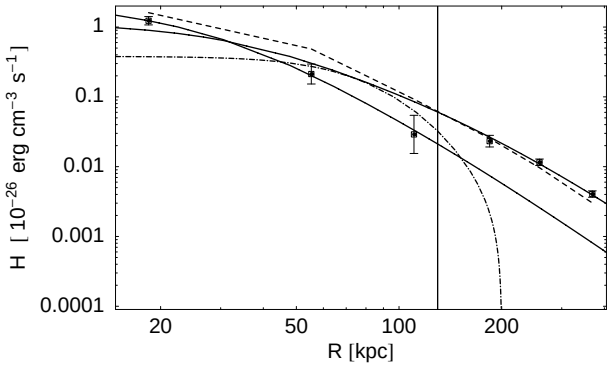

Figure 4. Energy requirements in A 1795: the plasma emissivity (for simplicity shown by the dashed line joining the data points) and heating due to thermal conduction (dot-dashed line) as a function of radius. The he extra heating curve (open squares) is determined by $f_{\rm c}\times$ Spitzer. Here $f_{\rm c} = 1/3$, the maximum value allowed in the models. The three bins inside the cooling radius (vertical line) alone are best fitted by an inner cutoff radius $r_0 = 14$ kpc and time-averaged AGN luminosity $L = 8.0 \times 10^{44}\,{\rm erg\,s^{-1}}$. For the same model all six bins are best fitted by an unphysical $r_0 = 179$ kpc and very high AGN luminosity $L = 3.3 \times 10^{45}\,{\rm erg\,s^{-1}}$. The two solid curves are the best fit functions for the two cases.

Table 1. The results for the effervescent heating model with no mass dropout (see text for comment).

Cluster	$f_{\rm c}^{\rm min,max}$	$r_0^{\rm min,max}$ (kpc)	$L^{\rm min,max}$ (erg s^{-1})
NGC 533*	0.00,0.26	0.3,1.5	$1.6, 2.6 \times 10^{42}$
Virgo*	0.03,0.26	0.6,18	$3.8, 21 \times 10^{42}$
A 262*	0.12,0.33	6.6,60	$8.1, 47 \times 10^{42}$
Sérsic 159*	0.00,0.33	22,23	$5.8, 5.8 \times 10^{44}$
MKW 9*	0.08,0.10	15,15	$5.7, 6.5 \times 10^{42}$
2A 0335*	0.00,0.33	15,16	$6.1, 6.8 \times 10^{44}$
MKW 3s	0.00,0.33	37,94	$4.3, 5.8 \times 10^{44}$
A 2052	0.00,0.33	6.6,21	$2.6, 3.4 \times 10^{44}$
A 4059*	0.00,0.33	4.7,54	$7.4, 50 \times 10^{43}$
Hydra A*	0.00,0.33	27,29	$7.0, 7.7 \times 10^{44}$
A 496*	0.07,0.28	11,86	$1.2, 5.7 \times 10^{44}$
A 3112	0.00,0.33	30,59	$1.3, 1.4 \times 10^{45}$
A 1795*	0.00,0.33	14,49	$8.0, 24 \times 10^{44}$
A 399	-	-	-
Perseus*	0.01,0.18	40,73	$1.6, 2.5 \times 10^{45}$
A 1835*	0.00,0.33	33.2,38	$1.0, 1.1 \times 10^{46}$

for every value of $0 < f_c < 1/3$, for some objects the fits converge only for models with f_c in a narrower interval ($f_{\rm c}^{\rm min}$-$f_{\rm c}^{\rm max}$, see Table 1). In particular in clusters where conduction is high (MKW 9 and Perseus), the solutions have conduction efficiency substantially lower than the maximum allowed value $f_c = 1/3$. In Sérsic 159−3, 2A 0335+096, Hydra A, A 3112 and A 1835 the conductivity yield is low and, as expected, different models (i.e. different values of f_c) give almost identical results.

It is crucial to highlight the trend of the best fit parameters of the different models with model parameter f_c. For most of the clusters the model with $f_{\rm c} = f_{\rm c}^{\rm max}$ is the one for which the values for both L and r_0 are smallest and for $f_{\rm c} = f_{\rm c}^{\rm min}$ the largest ($L^{\rm min,max}$ and $r_0^{\rm min,max}$ in Table 1). In addition L and r_0 vary monotonically with f_c within these limits. The clusters which exhibit this trend are labeled by an asterisk Table 1. For MKW 3s, A 2052 and A 3112 the trend just described is reversed. In these objects heat conduction lowers the extra heating curve especially in the cluster center. This implies more and more flattening of the extra heating curve at the center with increasing f_c which is finally reflected in the increase of both r_0 and L. Our conclusions are:

- for 4 clusters (Sérsic 159−3, 2A 0335+096, Hydra A and A 1835) the conductivity yield is extremely low and, as expected, different models (i.e. different values of f_c) give almost identical results,
- for 3 objects (MKW 3s, A 2052 and A 3112) we find that heat conduction plays an important role only at the cluster center and that, as a consequence, the trend between the fitted AGN parameters and conduction efficiency is not the one expected (i.e. conduction and AGN feedback do not co-operate),
- for one object (A 399) we do not find any solution for the effervescent heating model because heat conduction is very efficient,
- for the remaining 8 clusters (NGC 533, Virgo, A 262, MKW 9, A 4059, A 496, A 1795 and Perseus) conduction and AGN feedback are found to be co-operating as expected.

Since it has been shown that AGN heating alone is not able to quench CFs, it is fair to assume that thermal conduction, although operating at different rates from cluster to cluster, must play an important role as a heating mechanism, at least, of course, in the framework of the effervescent heating model. While this is found for 8 clusters in our sample, we have shown that heat conduction is either completely unrelevant in 4 clusters, too high for one object or high enough to play an important role but peaked at the cluster center in 3 clusters. Hence, if we assume that the effervescent heating provides a satisfactory explanation for the observed structure of CF clusters only in the case when AGN and conduction heating are effectively co-operating, we conclude that for half of the objects in the sample the effervescent heating does not provide a satisfactory explanation.

These findings prompt us to posit that, at least for

these objects, the description of their thermal structure through a *steady state* solution of the thermodynamic equations is not viable and that we are observing them at an evolutionary stage far from equilibrium. A clearer picture can be of course achieved by studying a much larger sample using the procedure employed in this work.

ACKNOWLEDGMENTS

This work is based on observations obtained with *XMM-Newton*, an ESA science mission with instruments and contributions directly funded by ESA Member States and the USA (NASA). RP acknowledges support from the Swiss National Science Foundation and the Tiroler Wissenschaftsfond. SRON is supported financially by NWO, the Netherlands Foundation for Scientific Research.

REFERENCES

Blanton, E. L. 2004, The Riddle of Cooling Flows in Galaxies and Clusters of galaxies

Brighenti, F., & Mathews, W. G. 2002, ApJ, 573, 542

De Grandi, S., & Molendi, S. 2002, ApJ, 567, 163

Ettori, S., Fabian, A. C., Allen, S. W., & Johnstone, R. M. 2002a, MNRAS, 331, 635

Ghizzardi, S., Molendi, S., Pizzolato, F., & De Grandi, S. 2004, ApJ, 609, 638

Gruzinov, A. 2002, astro-ph/0203031

Kaastra, J. S., Tamura, T., Peterson, J. R., et al. 2004, A&A, 413, 415

Markevitch, M., Forman, W. R., Sarazin, C. L., & Vikhlinin, A. 1998, ApJ, 503, 77

Narayan, R., & Medvedev, M. V. 2001, ApJ, 562, L129

Peterson, J. R., Kahn, S. M., Paerels, F. B. S., et al. 2003, ApJ, 590, 207

Piffaretti, R., Jetzer, Ph., Kaastra, J. S., & Tamura, T. 2005, A&A, 433, 101

Piffaretti, R. & Kaastra, J. S. 2005, submitted to A&A

Ponman, T. J., Sanderson, A. J. R., & Finoguenov, A. 2003, MNRAS, 343, 331

Pratt, G. W., & Arnaud, M. 2005, A&A, 429, 791

Pratt, G. W., Arnaud, M., & Pointecouteau, E. 2005, to appear in A&A, astro-ph/0508234

Ruszkowski, M., & Begelman, M. C. 2002, ApJ, 581, 223 (RB02)

Soker, N. 2003, MNRAS, 342, 463

Tozzi, P., & Norman, C. 2001, ApJ, 546, 63

Vikhlinin, A., Markevitch, M., Murray, S. S., Jones, C., Forman, W., & Van Speybroeck, L. 2005, ApJ, 628, 655

Voit, M. G. 2005, Rev. Mod. Phys., 77, 207

Zakamska, N. L., & Narayan, R. 2003, ApJ, 582, 162

AGN FEEDBACK AND EVOLUTION OF RADIO SOURCES: DISCOVERY OF AN X-RAY CLUSTER ASSOCIATED WITH Z=1 QUASAR

A. Siemiginowska[1], C. C. Cheung[2,3], S.LaMassa[1], D.Burke[1], T.L.Aldcroft[1], J.Bechtold[4], M.Elvis[1], and D.M.Worrall[5]

[1]Harvard-Smithsonian Center for Astrophysics, 60 Garden St., Cambridge, MA 02138, USA
[2]Jansky Postdoctoral Fellow; National Radio Astronomy Observatory, USA
[3]Kavli Institute for Particle Astrophysics & Cosmology Stanford University, Varian Physics, Stanford, CA 94305, USA
[4]Steward Observatory, University of Arizona, Tucson, AZ, USA
[5]Department of Physics, University of Bristol, Tyndall Ave., Bristol, UK

ABSTRACT

We report the first significant detection of an X-ray cluster associated with a powerful ($L_{bol} \sim 10^{47}$ erg sec^{-1}) radio-loud quasar at high redshift (z=1.06). Diffuse X-ray emission is detected out to $\sim$ 120 kpc from the CSS quasar 3C 186. A strong Fe-line emission at the $z_{rest} = 1.06$ confirms its thermal nature. We find that the CSS radio source is highly overpressured with respect to the thermal cluster medium by 2-3 orders of magnitude. This provides direct observational evidence that the radio source is not thermally confined as posited in the "frustrated" scenario for CSS sources. Instead, the radio source may be young and at an early stage of its evolution. This source provides the first detection of the AGN in outburst in the center of a cooling flow cluster. Powerful radio sources are thought to be triggered by the cooling flows. The evidence for the AGN activity and intermittent outbursts comes from the X-ray morphology of low redshift clusters, which usually do not harbour quasars. 3C186 is a young active radio source which can supply the energy into the cluster and potentially prevent its cooling. We discuss energetics related to the quasar activity and the cluster cooling flow, and possible feedback between the evolving radio source and the cluster.

Key words: quasars: individual (3C 186) - X-rays: galaxies: clusters.

1. INTRODUCTION

Quasars are luminous ($L_{tot} > 10^{45}$ erg sec^{-1}) and compact in the sense that the entire quasar luminosity originates within an unresolved core region (e.g. radius smaller than $r < 1$ pc). Large scale powerful outflows in a form of winds and jets are also observed. Such quasar activity is usually associated with an accretion process onto a supermassive black hole in the center of the a host galaxy (Silk & Rees 1998). This accretion process is not fully understood, however it is clear that a large fuel supply is needed to power a quasar. Where does the fuel come from and how quasars are born? The two scenarios involve a rich environment of clusters of galaxies: (1) a merger event can initiate a rapid fuel supply and efficient accretion; (2) large deposits of gas in the centers of cooling flow clusters can ignite the quasar (Fabian & Nulsen 1977).

There is a growing evidence for the past quasar activity in many X-ray clusters observed recently with *Chandra* X-ray Observatory. For example X-ray morphology of M87 in the Virgo cluster (Forman et al 2005) and Perseus A (Fabian et al 2003) shows large scale jets, signature of shocks and "bubbles" filled with radio plasma. Such X-ray morphology suggests a dissipation of energy into the cluster medium which prevents its cooling. Detailed studies of several clusters show the intermittent activity of a supermassive black hole of the central galaxy, with an average total outburst power reaching $\sim 10^{60}$ ergs. However, in all these systems the supermassive black hole of the cD galaxy is in the quiescence with the nucleus luminosity $L_{tot} < 10^{42}$ erg sec^{-1}. On the other hand one would expect that some powerful quasar should reside in clusters. Thus where are the clusters associated with the quasars?

Quasars are rare at low redshift, where most of X-ray clusters have been studied in details. The quasar density increases with redshift and in fact the quasars are seen in rich environment of clusters of galaxies in optical surveys (Ellingson, Yee & Green 1991). Over the last decade attempts have been made to find X-ray clusters associated with radio-loud quasars at high redshift. The limited capabilities of the available X-ray telescopes allowed only for a few detections of extended X-ray emission around radio sources at redshifts $z > 0.3$ (Hardcastle & Worrall 1999, Worrall et al. 2001, O'Dea et al 2000, Crawford

& Fabian 2003). High dynamic range observations are required to detect faint diffuse emission in the vicinity of a bright powerful source. Now *Chandra* can resolve spatially distinct X-ray emission components in the vicinity of a strong X-ray source with $\sim$1 arcsec resolution and a high dynamic range, as evidenced, for example, by the discovery of many resolved quasar X-ray jets (e.g. Schwartz et al. 2000, Siemiginowska et al. 2002, Sambruna et al. 2004, Marshall et al. 2005).

2. COMPACT RADIO SOURCES AND 3C 186 QUASAR

A large fraction of the radio source population is comprised of powerful compact sources (10-20%, O'Dea 1998). Their radio morphologies show a compact emission on arcsec (VLA resolution) scales while on milliarcsec scales (VLBI) the sources look remarkably like scaled down large radio galaxies, where the entire radio structure (1-10 kpc) is enclosed within the host galaxy. For more than a decade now there has been a clear controversy regarding their nature (see O'Dea 1998 and references therein). In the *evolution* model (Readhead et al. 1996a, 1996b) the source size and the characteristic spectral break at GHz radio frequencies could be an indication of young age, while in the other model the radio jet could be *frustrated* (Wilkinson et al. 1981, van Breugel et al. 1984) by a confining medium. Although recent studies give more weight to the *evolution* model there has been no definite observational evidence to rule out either of the models and both interpretations are still viable. Because these sources are very powerful one would expect that they reside in rich cluster environments. In either scenario the amount of fuel required to power a source is high, while in addition in the frustrated scenario the cluster medium should be dense enough to confine a radio source. Thus these compact radio may reside in clusters and therefore might be suitable candidates for detecting an X-ray cluster emission.

3C 186 is a luminous quasar ($L_{bol} \sim 10^{47}$ erg sec^{-1}). It has a strong big blue bump in the optical-UV band and broad optical emission lines (Simpson & Rawlings 2000, Kuraszkiewicz et al. 2002). It is therefore a typical quasar except for its radio properties. It is classified in radio as a compact steep spectrum (CSS) source. The radio morphology (Cawthorne et al 1986) shows two components separated by $2''$ and a jet connecting the core and NW component (Fig.1). No radio emission was reported on a larger scale. Based on the spectral age the estimated age of the radio source is $\sim 10^5$ years (Murgia et al. 1999).

3. CHANDRA OBSERVATIONS OF 3C 186

3C 186 was observed for $\sim$ 38 ksec with the *Chandra* Advanced CCD Imaging Spectrometer (ACIS-S, Weisskopf et al. 2002) on 2002 May 16 (ObsID 3098). The effective exposure time for this observation was 34,398 sec.

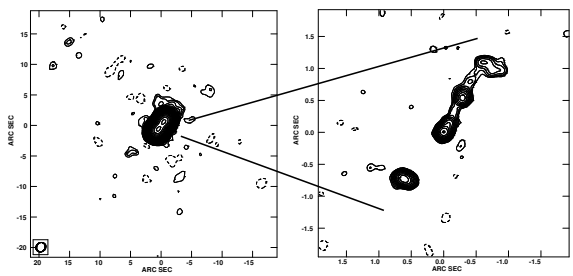

Figure 1. **Left:** *VLA 1.5 GHz image of 3C 186 The restoring beam is shown at the bottom left is 1.62" × 1.44" at PA=42.7 degrees. The image peak is 565 mJy/bm and contour levels begin at 0.5 mJy/beam (2σ) and increase by factors of $\sqrt{2}$. North is up East is left.* **Right:** *High resolution (0.15$''$) VLA 15 GHz image showing the 2" core-jet morphology. The image peak is 21.6 mJy/beam, and contours begin at 0.65 mJy/beam increasing by factors of $\sqrt{2}$.*

The 1/8 subarray CCD readout mode of one CCD only was used resulting in 0.441 sec frame readout time. Given the ACIS-S count rate of 0.025 counts s^{-1} frame^{-1} the pileup fraction was low $< 2\%$ (see PIMMS[1]). The X-ray data analysis was performed in CIAO 3.2[2] with the calibration files from the CALDB 3.0 data base. Spectral and image modeling and fitting was done in *Sherpa* (Freeman et al 2001). The details of the data analysis are presented elsewhere (Siemiginowska et al 2005).

3.1. X-ray Cluster at z=1.063

The *Chandra* observation reveals X-ray cluster emission at the redshift of the quasar 3C 186 (see Fig.2 and Fig.3). The cluster redshift is confirmed by the iron line detected in the spectrum of the diffuse emission. The X-ray properties of the cluster are summarized in Table 1. We compare the cluster temperature and its luminosity with results for the other clusters at high redshift using the MEKAL model with the abundance set to 0.3. The cluster temperature of $\sim 5.2^{+1.2}_{-0.9}$ keV and the total X-ray luminosity of $L_X(0.5-2\ \mathrm{keV}) \sim 6 \times 10^{44}$ erg sec^{-1} agree with the temperature-luminosity relation typically observed in high redshift ($z > 0.7$) clusters (e.g. Vikhlinin et al. 2002, Lumb et al. 2004). Based on the estimated cluster central electron density of approximately 0.044 ± 0.006 cm^{-3} for the best fit beta model parameters we infer the gas mass enclosed within 2 Mpc radius of $\sim 4.9^{\pm 0.7} \times 10^{13} M_\odot$ (the uncertainty only due to the uncertainty on electron density). This is about $\sim 6-10\%$ of the total cluster mass given the uncertainty on the cluster temperature and broadly agrees with the gas fraction usually found in high redshift (z>0.7) clusters. The estimated cooling time for the cluster core

[1] http://asc.harvard.edu/toolkit/pimms.jsp
[2] http://cxc.harvard.edu/ciao/

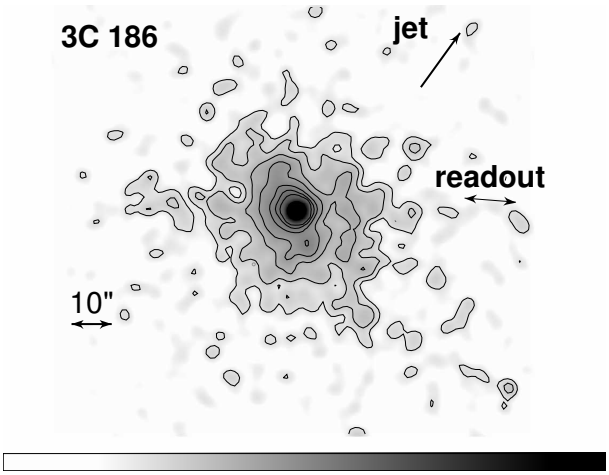

Figure 2. Adaptively smoothed exposure corrected image (photons energies within 0.3-7 keV range) of the Chandra ACIS-S observation of 3C 186 (Q0740+380). The diffuse emission is detected on $>$ 100 kpc scale, 1″=8.2 kpc. North is up and East is left. Contours represent a surface brightness of: (0.046,0.066, 0.13, 0.2, 0.33, 0.46, 0.66, 6.635, 33.175)$\times 10^{-6}$ photons cm^{-2} arcsec^{-2}. The direction of the CCD readout is indicated by arrow on the right side. An arrow in the upper right corner shows the PA=-37 deg of the 2″ radio jet (see Fig 1).

is $\sim 2.6 \times 10^9$ years which implies the cooling rate of ~ 50 M$_\odot$ year^{-1}.

3.2. Quasar in the Cluster

Based on the cluster central density and temperature, we estimate a central thermal pressure of the cluster medium to $\sim 5 \times 10^{-11}$ dyn cm^{-2}. If this pressure is higher than the pressure within the expanding radio components of the CSS source (Fig.1) then the cluster gas may be responsible for confining the radio source and its small size. Based on the radio measurements the minimum pressure in each radio component is of order $\sim 10^{-8}$ dyn cm^{-2}. Thus the radio source is highly overpressured by about 2-3 orders of magnitude with respect to the thermal cluster medium. This indicates that the hot gas cannot suppress the expansion and frustrate the jet, so the radio source is not confined, but it is at its early stage of the evolution into a large scale radio source.

The expansion of the radio source could potentially heat the cluster. The energy dissipated into the cluster by the expanding radio components has been widely discussed in the context of the low redshift clusters, where there is evidence for the repetitive outbursts of an AGN. However, the details of the dissipation process are still being studied (see Churazov review in this proceedings)

We can estimate the energy content of the hot cluster gas assuming a total emitting volume of 2.3×10^{71}cm^3

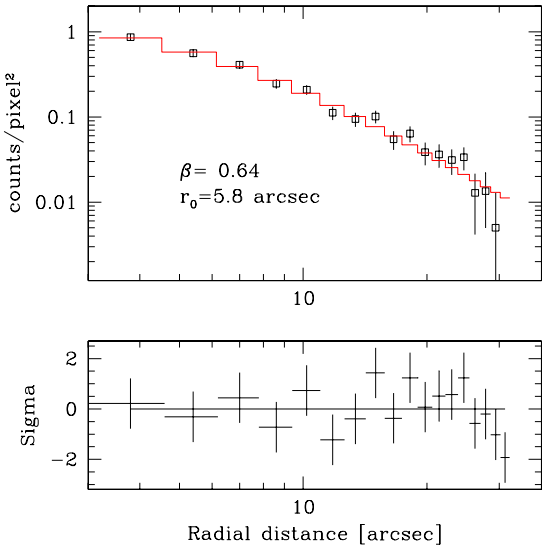

Figure 3. Background subtracted surface brightness profile for radii 3″ to 30″ fit with a beta model. The data are indicated by the square points. The solid line shows the best fit model with parameter $\beta = 0.64^{+0.11}_{-0.07}$ and a core radius of $r_{core} = 5.8''^{+2.1}_{-1.7}$. The bottom panel illustrates the differences between the data and the model in units of σ.

Table 1. Properties of the X-ray Cluster Emission.

Parameter	Property
β-model (1D)	β=0.64$^{+0.11}_{-0.07}$, r_c=5.8$^{+2.1}_{-1.7}$″
β-model (2D)	β=0.58$^{+0.06}_{-0.05}$, r_c=5.5$^{+1.5}_{-1.2}$″
	ellipticity = 0.24$^{+0.06}_{-0.07}$
	PA=47±10 degrees
$E_{\rm obs}$ (Fe-line)	3.18±0.07 keV
EW (Fe-line)	412 eV
$F_{\rm obs}$(0.5–2 keV)	$6.2 \pm 0.3 \times 10^{-14}$ erg sec^{-1} cm^{-2}
$F_{\rm obs}$(2–10 keV)	$5.0 \pm 0.7 \times 10^{-14}$ ergs sec^{-1} cm^{-2}
$F_{\rm nonthermal}$ (1 keV)	$<5.4 \times 10^{-15}$ erg sec^{-1} cm^{-2}
$L_{\rm tot}$(0.5–2 keV)	6×10^{44} erg sec^{-1}
n$_e$	0.044±0.006 cm^{-3}
M$_{gas}$($r < 2$Mpc)	$4.9\pm0.7 \times 10^{13}$ M$_\odot$

Fluxes are unabsorbed. Luminosities are K-corrected and in the source frame.

(contained by an annulus with 3 and 15″ radii, assuming spherical geometry) and $kT \sim 5$ keV, to be of the order of $\frac{3}{2}kTnV \sim 4.5{\times}10^{61}$ ergs (where n is the average gas particle density in the cluster). Assuming that the expanding radio source has been delivering the energy into the cluster at the current level of $L_{jet} \sim 10^{46}$erg sec^{-1} then the heating time is of the order of $\sim 10^8$ years. We can also estimate the amount of mechanical work done by the jet and radio components during the expansion to the current radio size ($2'' \times 0.3'' \sim 2.3 \times 10^{66}$cm^3) as $pdV \sim 2 \times 10^{55}$ ergs. If the expansion velocity is of the order of $0.1c$ then the radio source has been expanding for about 5×10^5 years with an average power of $6{\times}10^{42}$ erg sec^{-1}. The estimated jet power is ~ 3 orders of magnitude higher.

The quasar optical-UV (big blue bump) luminosity of $5.7{\times}10^{46}$erg sec^{-1} (Simpson & Rawlings, 2000) is related to the accretion onto a supermassive black hole, so we can estimate the central black hole mass and required accretion rate. Assuming that the quasar is emitting at the Eddington luminosity the black hole mass should be of the order $\sim 4.5 \times 10^8 M_\odot$. From CIV FWHM measurements of Kuraszkiewicz et al (2002) and the Vestergaard (2002) scaling relationship for the black holes, the estimated mass of the black hole is a factor of 10 higher, $\sim 3.2 \times 10^9 M_\odot$. In any case the accretion rate required by the observed UV luminosity, assuming 10% radiation efficiency is equal to ~ 10 M$_\odot$year^{-1}. Given the age of the radio source of 5×10^5 years, a total of $\sim 5 \times 10^6 M_\odot$ should have been accreted onto the black hole to support the current "outburst". This is only a small fraction of the mass involved in any merger events. Future detailed studies of the host galaxy and the optical field surrounding the quasar could provide more information on a population of galaxies and possible signatures of a merger.

4. SUMMARY

Chandra detected the X-ray cluster emission up to $\sim$ 120 kpc away from 3C 186, the CSS quasar at $z = 1.063$.

- There could be a cooling flow in the cluster, $t_{cool} \sim 1.6 \times 10^9$ years.
- This cluster is associated with the quasar, L$\sim 10^{47}$ erg sec^{-1}. Low redshift clusters show evidence of the past AGN outbursts, while their central AGN is typically quiet.
- Thermal pressure of the cluster gas is $\sim 2-3$ orders of magnitude lower than the pressure in the radio components. Hot cluster gas does not confine the jet.
- Future XMM observations would allow for studying a large scale cluster emission.
- Deep optical imaging could provide details on properties of the host galaxy and the population of galaxies in this high redshift cluster at the early stage of its formation.

ACKNOWLEDGMENTS

This research is funded in part by NASA contract NAS8-39073. Partial support for this work was provided by the National Aeronautics and Space Administration through Chandra Award Number GO-01164X and GO2-3148A issued by the Chandra X-Ray Observatory Center, which is operated by the Smithsonian Astrophysical Observatory for and on behalf of NASA under contract NAS8-39073. The VLA is a facility of the National Radio Astronomy Observatory is operated by Associated Universities, Inc. under a cooperative agreement with the National Science Foundation.

This work was supported in part by NASA grants GO2-3148A, GO-09820.01-A and NAS8-39073.

REFERENCES

Cawthorne, T. V., Scheuer, P. A. G., Morison, I., & Muxlow, T. W. B. 1986, MNRAS, 219,883

Crawford, C. S. & Fabian, A. C. 2003, MNRAS, 339, 1163

Ellingson, E., Yee, H. K. C., & Green, R. F. 1991, ApJ, 371, 49

Fabian, A. C., Sanders, J. S., Crawford, C. S., & Ettori, S. 2003, MNRAS, 341, 729

Fabian, A. C., & Nulsen, P. E. J. 1977, MNRAS, 180, 479

Forman, W. et al. 2005, astro-ph/0312576

Freeman, P., Doe, S., & Siemiginowska, A. 2001, Proc. SPIE, 4477, 76

Hardcastle, M. J., & Worrall, D. M. 1999, MNRAS, 309, 969

Kuraszkiewicz, J. K., Green, P. J., Forster, K., Aldcroft, T. L., Evans, I. N., & Koratkar, A. 2002, ApJS, 143, 257

Lumb, D. H., et al. 2004, A&A, 420, 853

Marshall, H. L., et al. 2005, ApJS, 156, 13

Murgia, M., Fanti, C., Fanti, R., Gregorini, L., Klein, U., Mack, K.-H., & Vigotti, M. 1999, A&A, 345, 769

O'Dea, C. P., De Vries, W. H., Worrall, D. M., Baum, S. A., & Koekemoer, A. 2000, AJ, 119, 478

O'Dea, C. P. 1998, PASP, 110, 493

Readhead, A. C. S., Taylor, G. B., Xu, W., Pearson, T. J., Wilkinson, P. N., & Polatidis, A. G. 1996a, ApJ, 460, 612

Readhead, A. C. S., Taylor, G. B., Pearson, T. J., & Wilkinson, P. N. 1996b, ApJ, 460, 634

Sambruna, R. M., Gambill, J. K., Maraschi, L., Tavecchio, F., Cerutti, R., Cheung, C. C., Urry, C. M., & Chartas, G. 2004, ApJ, 608, 698

Schwartz, D. A., et al. 2000, ApJ, 540, L69

Silk, J., & Rees, M.J., 1998, A&A, 331, L1;

Siemiginowska, A., Bechtold, J., Aldcroft, T. L., Elvis, M., Harris, D. E., & Dobrzycki, A. 2002, ApJ, 570, 543

Siemiginowska, A., Cheung, C. C., LaMassa, S., Burke, D. J., Aldcroft, T. L., Bechtold, J., Elvis, M., & Worrall, D. M. 2005, ApJ, 632, 110

Simpson, C., & Rawlings, S. 2000, MNRAS, 317, 1023

van Breugel, W., Miley, G., & Heckman, T. 1984, AJ, 89, 5

Vestergaard, M. 2002, ApJ, 571, 733

Vikhlinin, A., VanSpeybroeck, L., Markevitch, M., Forman, W. R., & Grego, L. 2002, ApJ, 578, L107

Weisskopf, M. C., Brinkman, B., Canizares, C., Garmire, G., Murray, S., & Van Speybroeck, L. P. 2002, PASP, 114, 1

Wilkinson, P. N., Booth, R. S., Cornwell, T. J., & Clark, R. R. 1984, Nature, 308, 619

Worrall, D. M., Birkinshaw, M., Hardcastle, M. J., & Lawrence, C. R. 2001, MNRAS, 326, 1127

THE TOTAL MASS AND THE GAS FRACTION IN X-RAY GALAXY CLUSTERS: DO WE REALLY KNOW WHAT WE MEASURE ?

Stefano Ettori

INAF, Osservatorio Astronomico di Bologna, Italy

ABSTRACT

I present recent work done to study (1) the systematics that affect the total cluster mass measurements through X-ray analysis and (2) the distribution of baryons in simulated X-ray galaxy clusters.

Key words: X-rays: galaxies: clusters; dark matter; galaxies: clusters.

1. INTRODUCTION

My quick answer to the provocative question in the title is **yes**. I will discuss more extensively on the systematics that affect the total mass and the gas mass fraction measurements obtained through X-ray studies.

2. SYSTEMATICS IN THE X-RAY CLUSTER MASS ESTIMATORS

This work is done in collaboration with Elena Rasia, Lauro Moscardini, Pasquale Mazzotta and others (Rasia, Ettori et al. 2005, MNRAS, submitted). We examine the systematics affecting the X-ray total mass estimators applied to a set of five galaxy clusters resolved at high resolution in hydrodynamic simulations, including cooling, star formation and feedback activities and assuming the standard ΛCDM cosmological model (see Borgani et al. 2004). The simulation has been carried out with the parallel Trees-PH simulation code GADGET-2 (Springel 2005). A first cluster of our sample (C_{Pert}) is directly extracted from the final output of this simulation by using the standard identification criteria based on the spherical over-density. The remaining four objects have been instead obtained by re-simulating at high-resolution galaxy clusters selected from the same simulation. The new initial conditions for these runs have been generated by applying the Zoomed Initial Condition technique (Tormen et al. 1997). This method allows to increase the mass resolution in a suitably chosen high–resolution Lagrangian region surrounding the structure to be re–simulated, and at the same time to correctly describe the large–scale tidal field of the cosmological environment by using low–resolution particles. Notice that we performed a series of DM–only runs to create initial conditions which produce clusters that, at $z = 0$, are not affected by contamination from low-resolution particles out to (4–6) virial radii. These initial conditions, suitably adapted to include the gas component, have been used to obtain the high–resolution re–simulations corresponding to the galaxy clusters C_{Merg}, C_{Rel1}, C_{Rel2} and C_{z05}. To summarize, the following five objects have been selected as examples of clusters with different thermal and dynamic state: C_{Pert} ($T_{\rm sl} = 3.9$ keV, $M_{\rm vir} = 7.0 \times 10^{14}\, M_\odot$), a perturbed cluster which shows in the temperature map a cold substructure infalling toward the center; C_{Merg} ($T_{\rm sl} = 3.6$ keV, $M_{\rm vir} = 4.1 \times 10^{14}\, M_\odot$), an object that experienced a recent major merger; C_{Rel1} ($T_{\rm sl} = 3.3$ keV, $M_{\rm vir} = 3.6 \times 10^{14}\, M_\odot$), a relaxed structure (see Fig. 1; C_{Rel2} ($T_{\rm sl} = 2.7$ keV, $M_{\rm vir} = 2.3 \times 10^{14}\, M_\odot$), a colder relaxed cluster; C_{z05} ($T_{\rm sl} = 2.8$ keV, $M_{\rm vir} = 2.6 \times 10^{14}\, M_\odot$), a medium–temperature cluster at redshift of 0.5 that corresponds to the most massive progenitor of C_{Rel1}.

We obtain mock *Chandra* ACIS-S3 observations of the simulated objects through the X-ray Map Simulator, *X-MAS* (Gardini et al. 2004). This software is constituted from two main units: a *first unit* uses as input the output of a hydro-N-body simulation. For each gas particle, the emissivity is computed and distributed over the corresponding volume. After selecting a line of sight for the simulated observation, (i) the projected spectrum for each pixel and, then, (ii) the differential flux for each angular coordinate in bins of energy are computed. The final step is to add the Galactic absorption. A *second unit* estimates the expected number counts and iteratively subdivide the tile region until the counts become smaller than a given threshold (10 counts). The `XSPEC` command `FAKEIT` is then used to convolve the spectral model of each subregion with the response of the CCD and to add the sky background. A final photon event file is then generated and analyzed with standard tools, like CIAO and `XSPEC`, as done for real observations. Since we want to study the systematic discrepancies between observed and real quantities for ideal observations, we have applied very long exposure times to all the simulated observations aiming to minimize the statistical uncertainties related to the number counts: 1 Msec for C_{Pert}, C_{Merg}, C_{Rel1} and C_{Rel2}, and 1.5 Msec for C_{z05}.

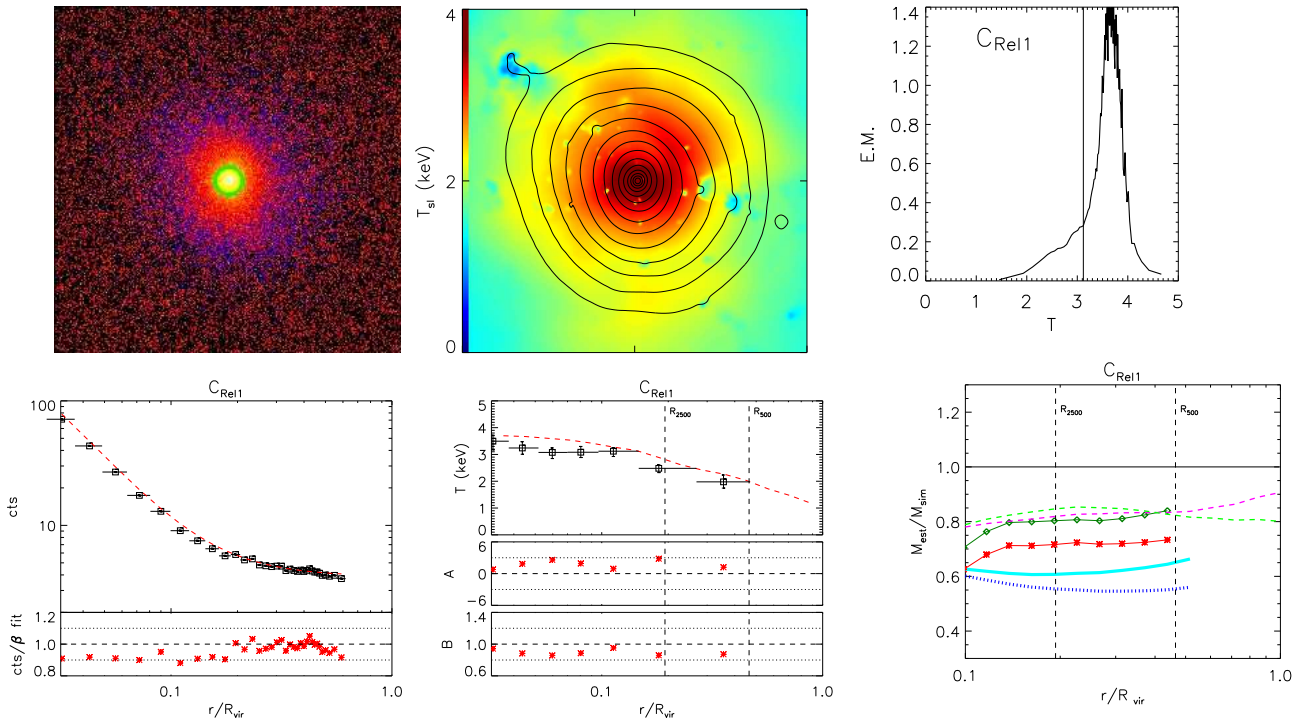

Figure 1. Results for C_{Rel1}. From top-left to bottom-right: (a) photon images in the X-ray soft [0.5-2 keV] energy band The images are 8.3 arcmin-width, exposure-corrected, and binned to $2''$–pixel. The green circles show the regions masked out in the analysis. (b) X-ray logarithmic isoflux contours over-plotted to the spectroscopic-like temperature map, both extracted directly from the hydrodynamic simulations; the temperature scale is shown on the left. (c) Emission measure from region inside R_{500}. The solid vertical black line refers to T_{500}. (d) The surface brightness profile (in units of photon counts) of the simulated cluster C_{Rel1}. Open squares represent the values extracted from the X-ray analysis, the horizontal bars correspond to the bin sizes. The solid curve is the corresponding best-fit β-model, with $\beta = 0.52$ and $r_c = 22$ kpc (= 0.014 $R_{\rm vir}$). The bottom panel shows the ratio between the profile from the X-ray analysis and the best-fit β-model. (e) Deprojected temperature profile. The dashed line represents the profile for the three-dimensional mass-weighted temperature $T_{\rm mw}$ as obtained from the hydrodynamic simulation. The open squares are the values extracted from the X-ray analysis, the vertical bars are 1σ errors ($\sigma_{\rm spec}$), while the horizontal ones correspond to the bin sizes. The bottom graphs in each panel show quantities related to the differences between the two temperatures: $A \equiv (T - T_{\rm mw})/\sigma_{\rm spec}$ and $B \equiv (T/T_{\rm mw})$. The dotted lines indicate $A = (-3, 3)$ and $B = (0.8, 1.2)$. (f) Ratios between the mass profiles derived from the X-ray analysis, $M_{\rm est}$, and the true mass profile of the simulated cluster, $M_{\rm sim}$. The vertical lines indicate R_{500} and R_{2500}. Total mass estimates: red asterisks = M_{HE}, green diamonds = $M_{HE,v}$, solid cyan line = M_β, dotted blue line = $M_{\beta,\gamma}$, green dashed line = $M_{\rm NFW}$, magenta dashed line = $M_{\rm RTM}$.

2.1. X-ray analysis

The surface brightness profiles have been extracted from [0.5-5 keV] images that have been corrected by the corresponding exposure maps. The profiles are build by considering annuli centered on the minimum of the cluster potential well (which is always off-set from the X-ray peak by less than 2 arcsec) and requiring a fixed number of counts per bin (between 2,500 and 10,000). These azimuthally-averaged profiles are then fitted with a β-model.

The overall temperature is measured in spectra extracted from circular regions centered on the cluster center and with $r = R_{500}$. The temperature profiles are measured in spectra extracted from the same annular regions used in the spatial analysis. For each region, the ancillary response file (ARF) and the redistribution matrix file (RMF), weighted by the X-ray brightness in the [0.3–2 keV] energy range, are computed by using the CIAO tools `mkwarf` and `mkrmf`. Source spectra are extracted from the event file, re-binned to have a minimum of 20 counts per bin and analyzed in the [0.6–7 keV] band. Background spectra are extracted from the background event file for the same source regions. A thermal model (`mekal`) absorbed by the Galactic column density is fitted to the data by using the χ^2 statistic in `XSPEC`. The only free parameters are the gas temperature and the normalization, being Galactic absorption $N_{\rm H}$, redshift z and metallicity Z fixed to the input values adopted in the *X-MAS* run: $N_{\rm H} = 5 \times 10^{20}$ cm^{-2}, $z = 0.175$ (or 0.5 in the case of C_{z05}) and $Z = 0.3 Z_{\odot}$.

To compute the mass through the equation of the hydrostatic equilibrium, we need to recover the three-dimensional profiles of the gas temperature and density by deprojecting the quantities measured in the X-ray spectral analysis. We adopt the deprojection technique presented in Ettori et al. (2002). In Fig.1, we compare the deprojected temperature measurements in C_{Rel1}, T, with the three-dimensional mass-weighted estimates, $T_{\rm mw} = \int mTdV / \int mdV$ with m being the mass of each gas particle, as obtained from the simulations. $T_{\rm mw}$ is the proper value that one should use in the hydrostatic equilibrium equation to measure the mass. Note that its profile is in remarkable good agreement with the deprojected spectral one, since the cluster in exam has a quite azimuthally symmetric thermal structure.

2.2. X-ray estimates of the gravitational mass

The "true" mass profile, $M_{\rm sim}(< r)$, of the simulated objects, obtained by summing all the masses of the particles inside a sphere of radius r, can be now compared to several different X-ray mass estimators, $M_{\rm est}$: (1) $M_{\rm HE}$ and $M_{\rm HE,v}$ from the direct application of the hydrostatic equilibrium (HE) equation neglecting and including contributions from the gas motion, respectively; (2) $M_{\beta,\gamma}$ by using a $\beta-$model and both an isothermal ($\gamma = 1$) and polytropic temperature profile; (3) $M_{\rm NFW}$ and $M_{\rm RTM}$ by assuming the analytic mass models in Navarro, Frenk & White (1995) and Rasia, Tormen & Moscardini (2004), respectively, that, combined with the deprojected gas density profile, enable us to recover a temperature profile through the numerical inversion of the HE equation that is then fitted to the observed profile (see Fig. 1).

We find that the main sources of the discrepancy are, in decreasing order of significance, (i) the neglected contribution from the gas motions to the energy budget, (ii) the bias in the X-ray temperature measurements, (iii) the poor determination of the parameters describing the spatially-extended X-ray emission, (iv) a temperature profile assumed to be inappropriately either constant or described by a polytropic relation. In particular, about half of the total error budget of the discrepancy between the true mass and the mass derived from the hydrostatic equilibrium equation is provided from neglecting the kinetic energy still present as bulk motions of the intra-cluster medium. The poorness of the $\beta-$model in describing the gas density profile makes the evaluated masses to be underestimated by ~ 35 per cent with respect to the true mass, both with an isothermal and a polytropic temperature profile. We conclude that the most robust way to recover through X-ray analysis the input radial mass distribution is to adopt an analytic mass model, such as the above-mentioned NFW and RTM, and fit the temperature profile expected from the hydrostatic equilibrium equation to the observed one over a sufficiently large (i.e. $r > R_{500}$) radial range.

3. THE BARYON FRACTION IN SIMULATED GALAXIES CLUSTERS

In this work, Klaus Dolag, Stefano Borgani, Giuseppe Murante and I (Ettori et al. 2005, MNRAS, submitted, astro-ph/0509024) study the baryon mass fraction in a set of hydrodynamical simulations of galaxy clusters performed using the Tree+SPH code `GADGET-2` (Springel 2005) that includes an entropy-conserving formulation of SPH, radiative cooling, heating by a UV background, and a treatment of star formation and feedback from galactic winds powered by supernova explosions. The purpose of the present work is to use an extended set of hydrodynamical simulations of galaxy clusters, treating a variety of physical processes, to study how the spatial distribution of the baryons, as contributed from both the stellar component and the hot X-ray emitting gas, are affected by the physical conditions within clusters at different redshift. The following physical schemes are considered: *Gravitational heating only (code=G)*; *Gravitational heating only with low viscosity scheme (code=GV)*, where an alternative implementation of artificial viscosity is used and clusters are found to have up to 30 per cent of their thermal energy in the turbulent motion of the ICM; *Cooling + Star Formation + Feedback with weak winds (code=FwW)*, where the wind speed is fixed at ≈340 km s^{-1}; *Cooling + Star Formation + Feedback with weak winds and Conduction (code=FwWC)*, where the conduction efficiency is set to be $1/3$ of the Spitzer rate; *Cooling + Star Formation + Feedback with no winds (code=F)*, that is like *FwW*, but with winds switched off;

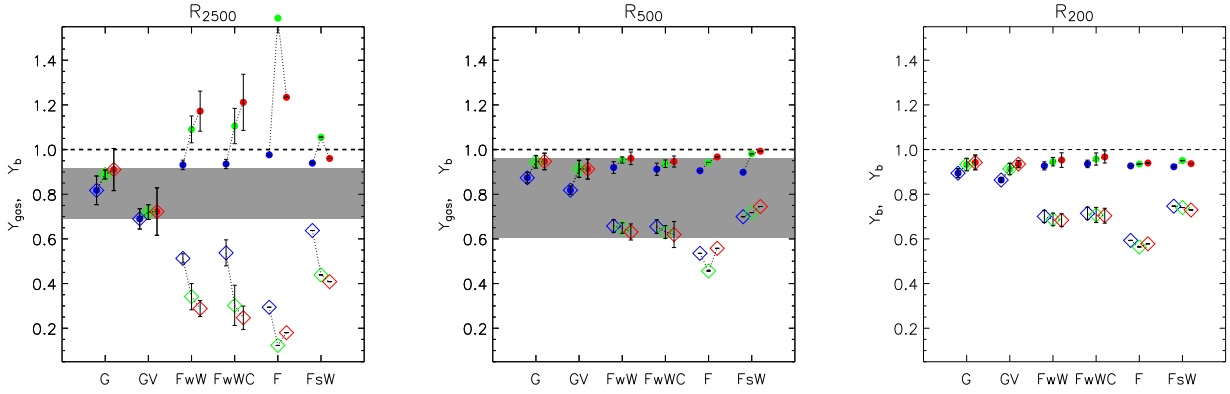

Figure 2. The gas (diamonds) and total baryon (dots) mass fractions, in unit of the cosmic baryonic value at R_{2500} (left panel), R_{500} (central panel) and R_{200} (right panel). For each physical case considered, we plot the mean and standard deviation values measured at $z = 0$, 0.7 and 1. The shaded region show the error-weighted mean and standard deviation of (1) $f_{\rm gas}(R_{2500})$ estimated from 26 X-ray luminous galaxy clusters in Allen et al. (2004, quoted in Table 2 for a LCDM universe), (2) $f_{\rm gas}(R_{500})$ from 35 highly luminous ($L_{\rm X} > 10^{45}$ erg s^{-1}) objects in Ettori & Fabian (1999). The observational data are normalized to $\Omega_{\rm b}h^2 = 0.0214 \pm 0.0020$ (Kirkman et al. 2003), $H_0 = 70$ km s^{-1} Mpc^{-1} and $\Omega_{\rm m} = 0.3$.

Cooling + Star Formation + Feedback with strong winds (code=FsW), where the winds have a speed of ≈480 km s^{-1}, corresponding to a supernova efficiency of unity.

We consider two sets of clusters, which have been selected from different parent cosmological boxes. The first set is extracted from the large–scale cosmological simulation presented in Borgani et al. (2004). The second one is a re-simulation of 9 galaxy clusters, extracted from a pre-existing lower–resolution DM–only simulation. The center of each cluster is defined as the position of the particle having the minimum value of the gravitational potential. Starting from this position, we run a spherical overdensity algorithm to find the radius R_{Δ_c} encompassing a given overdensity Δ_c, with respect to the critical one at the redshift under exam, and the mass M_{Δ_c} enclosed within this radius. In the present work, we consider values of the overdensity Δ_c equal to 2500, 500 and 200. The corresponding radii relate to the virial radius, which defines a sphere with virial overdensity (of $\approx$ 101 at $z = 0$ and $\approx$ 157 at $z = 1$ for our cosmological model and with respect to the critical value), as $(R_{2500}, R_{500}, R_{200}) \approx (0.2, 0.5, 0.7) \times R_{\rm vir}$. For each cluster, the hot gas mass fraction and the stellar mass fraction within a given radius r are then calculated as $f_{\rm gas}(< r) = M_{\rm gas}(< r)/M_{\rm tot}(< r)$ and $f_{\rm star}(< r) = M_{\rm star}(< r)/M_{\rm tot}(< r)$, respectively.

For the sake of clarity, we define the quantities $Y_{\rm gas}$, $Y_{\rm star}$ and $Y_{\rm b}$ as the ratios between $f_{\rm gas}$, $f_{\rm star}$ and $f_{\rm b} = f_{\rm gas} + f_{\rm star}$, and the cosmic value adopted in the present simulations, $\Omega_{\rm b}/\Omega_{\rm m} = 0.13$. The quantities $Y_{\rm gas}$ and $Y_{\rm b}$ at R_{2500}, R_{500} and R_{200}, as a function of redshift and physics included in the simulations, are plotted in Fig. 2. In the inner cluster regions, the dissipative action of radiative cooling enhances the average $Y_{\rm b}$ to super-cosmic values at high redshift. At late times cooling is less efficient, and $Y_{\rm b}$ declines, although to values (~ 0.9 at $z = 0$) that remain higher than those of the non-radiative runs. A smaller scatter and more widespread agreement among the different physical regimes are instead found in the outskirts ($r \approx R_{500}$ and above). The gas fraction within R_{2500} is about 0.3 times the cosmic value at $z = 1$ and 0.6 at $z = 0$, whereas is more tightly distributed around $0.6 - 0.7$ at larger radii, with evidence of larger values in the presence of strong winds. We also compare in Fig. 2 our simulation results with the observed $f_{\rm gas}$ distribution in highly X-ray luminous clusters. Simulations clearly indicate a sizeable underestimate of the hot baryons budget, both at R_{2500} and at R_{500}. When extra physics is added to the action of gravitational heating, lower hot gas fractions result. The discrepancy with the inferred observed fraction signals the existence of systematic errors, either in our physical treatment, or in estimates of the observed fraction, or possibly both. It is worth noticing that total mass estimates, for instance, suffer from systematic differences when measured from X-ray analysis and from dark matter particles in simulations, mainly owing to bias in the X-ray spectral temperature measurements (see, e.g., Mazzotta et al. 2004 and, specifically related to the systematics in X-ray mass estimates, Rasia et al. 2005 and previous section).

As for the cluster set extracted from a cosmological box, which are simulated by including cooling, star formation and feedback with weak (340 km s^{-1}) winds, we find at R_{200} $Y_{\rm b} = 0.93$, $Y_{\rm gas} = 0.74$ and $Y_{\rm star} = 0.20$, with scatter around these values of 2, 4 and 8 per cent, respectively. These results are virtually independent of the cluster mass over the range $M_{\rm vir} \approx (0.5-13) \times 10^{14} h^{-1} M_\odot$. The dispersion relative to the mean value measured at R_{2500} is a factor of about 3 larger than R_{200}.

In the four massive ($M_{200} > 10^{15} h^{-1} M_\odot$) galaxy clus-

ters simulated with 6 different physical schemes, we find that the cosmic value of the baryon fraction $\Omega_{\rm b}/\Omega_{\rm m}$ is reached at about $3 \times R_{200}$. The gas fraction increases radially, reaching 50 (80) per cent of the value measured at R_{200} at $r \approx 0.1(0.3)R_{200}$ at $z = 0$. At $z = 1$ the same values are reached at radii which are about 40 per cent larger. This indicates that $f_{\rm gas}$ tends to be less concentrated at higher redshift, where the more efficient star formation causes a more efficient removal of gas from the hot phase in the central cluster regions. We also find that in these clusters the amount of hot baryons, in unit of the cosmic value, is less scattered and less dependent on the particular physics adopted when it is measured over larger cluster regions. In the runs with *Gravitational heating only*, $Y_{\rm b} = f_{\rm bar}/(\Omega_{\rm b}/\Omega_{\rm m})$ ranges between 0.82 ± 0.06 (at R_{2500}) and 0.89 ± 0.02 (at R_{200}) at $z = 0$. It increases at $z = 1$ to 0.91 ± 0.10, 0.95 ± 0.04 and 0.94 ± 0.03 at R_{2500}, R_{500} and R_{200}, respectively.

3.1. Implications for the constraints on cosmological parameters

Our results have a direct implication on the systematics that affect the constraints on the cosmological parameters obtained through the cluster baryon mass fraction (e.g. White et al. 1993, Ettori 2003, Allen et al. 2004 and references therein). We remind that, once a representative gas fraction, denoted here $\hat{f}_{\rm gas}$, is directly measured from X-ray observations and a statistical relation between the average $\hat{f}_{\rm star}$ and $\hat{f}_{\rm gas}$ is adopted, the cosmic mass density parameter can be then evaluated as

$$\Omega_{\rm m} = \frac{Y_{\rm b}\ \Omega_{\rm b}}{\hat{f}_{\rm gas}\left(1 + \hat{f}_{\rm star}/\hat{f}_{\rm gas}\right)}, \qquad (1)$$

where the "hat" indicates the observed quantities and the cosmic baryon density $\Omega_{\rm b}$ is assumed from primordial nucleosynthesis calculations or the measured anisotropies in the cosmic microwave background. In recent years this method has been also extended to the measure of the dark energy density parameters (Ω_Λ, w; see, e.g., Ettori et al. 2003, Allen et al. 2004) under the assumption that the gas fraction remains constant in redshift (Sasaki 1996). Since the gas fraction scales with the angular diameter distance as $f_{\rm gas} \propto d_{\rm A}^{1.5}$, the best choice of cosmological parameters is defined as the set of values that minimizes the χ^2 distribution of the measured gas fraction at different redshifts.

Despite its conceptual simplicity and straightforward application, this method makes some assumptions that have to be tested before the error bars estimated for the matter and dark–energy density parameters can be accepted as robust and reliable determination of both statistical and systematic uncertainties. In the present discussion, we highlight two of the assumptions generally adopted, but never verified: (1) the mean value of $Y_{\rm b}$ does not evolve with redshift, (2) a fixed ratio between $f_{\rm star}$ and $f_{\rm gas}$ holds in a cluster at any radius and redshift. As we have shown here, both these assumptions are not valid in our simulated dataset whatever is the physics included in the simulations, in particular when considering the inner part of the clusters. Allen et al. (2004) use the simulation results by Eke et al. (1998) to fix $Y_{\rm b} = 0.824 \pm 0.033$ at $r \approx R_{2500}$ for their sample of *Chandra* exposures of the largest relaxed clusters with redshift between 0.07 and 0.9. We notice, for instance, that, while this value is in agreement with our simulation results at $z = 0$ in the runs with *Gravitational heating only* ($Y_{\rm b} = 0.82 \pm 0.06$), it is definitely lower than what we estimate at higher redshift (e.g. $Y_{\rm b} = 0.86, 0.89, 0.91$ at $z = 0.3, 0.7, 1$, respectively). This increase of $Y_{\rm b}$ with redshift is the consequence of the different accretion pattern of shock-heated baryons at different epochs. At later times, accreting gas had more time to be pre-shocked into filaments. As a consequence, they have a relatively higher entropy, thus relatively increasing the radius (in unit of the virial radius) where accretion shocks take place.

Since the tighter cosmological constraints provided by the cluster gas fraction alone are on $\Omega_{\rm m}$ (of the order of 16 per cent at 1σ level; e.g. Allen et al. 2004), we try to quantify the effect of the variation of the baryonic components with the radius and the redshift on this estimate. To this purpose, we use equation 1 and evaluate first how $\Omega_{\rm m}$ changes by varying $Y_{\rm b}$. The increasing baryon fraction with redshift induces larger estimate of $\Omega_{\rm m}$ with respect to what obtained from local measurements of $Y_{\rm b}$:

$$\frac{\Omega'_{\rm m} - \Omega_{\rm m}}{\Omega_{\rm m}} = \frac{\Delta\Omega_{\rm m}}{\Omega_{\rm m}} = \frac{Y_{\rm b}(< R_\Delta, z = z_o)}{Y_{\rm b}(< R_\Delta, z = 0)} - 1 \qquad (2)$$

is $+0.09$ at $R_\Delta = R_{2500}$ and $z_o = 0.7$ for the case with gravitational heating only and $+0.11$ at $z_o = 1$. (Here the prime symbol $'$ indicates the corrected value with respect to the reference one). Using instead the runs with reduced viscosity, the deviation decreases to about $+0.05$. As for the radiative runs, the bias is of the order of 20 per cent, that reduces to 2 per cent in presence of strong winds at $z = 1$. When outer cluster regions are mapped (i.e. $r \sim R_{500}$), the deviation converges to similar amounts due to the limited impact of cooling and feedback over large volumes: variations between $+0.03$ (weak winds) and $+0.10$ (strong winds) become comparable to $\Delta\Omega_{\rm m}/\Omega_{\rm m} \approx +0.08$ as measured in non–radiative runs.

A further contribution to the uncertainties comes from the dependence upon the radius and redshift of the ratio $f_{\rm star}/f_{\rm gas}$. In the observational determination of the baryon fraction from Eq. 1, this quantity is generally assumed to be 0.16, as measured in the Coma cluster within the virial radius (e.g. White et al. 1993). Note that our estimate from Lin et al. (2003) and adopting the total mass measurements in Arnaud et al. (2005) is 0.11 ± 0.04 or $M_{\rm gas}/M_{\rm star} \approx 8.7$ (r.m.s. $= 2.7$) at R_{500} in systems with gas temperatures larger than 3 keV. The latter value is a factor between 2.5 and 6 larger than what obtained in our simulated objects, thus witnessing the presence of significant overcooling. If we compare the ratio $\phi = f_{\rm star}/f_{\rm gas}$ measured for a Coma–like simulated cluster at R_{200} and

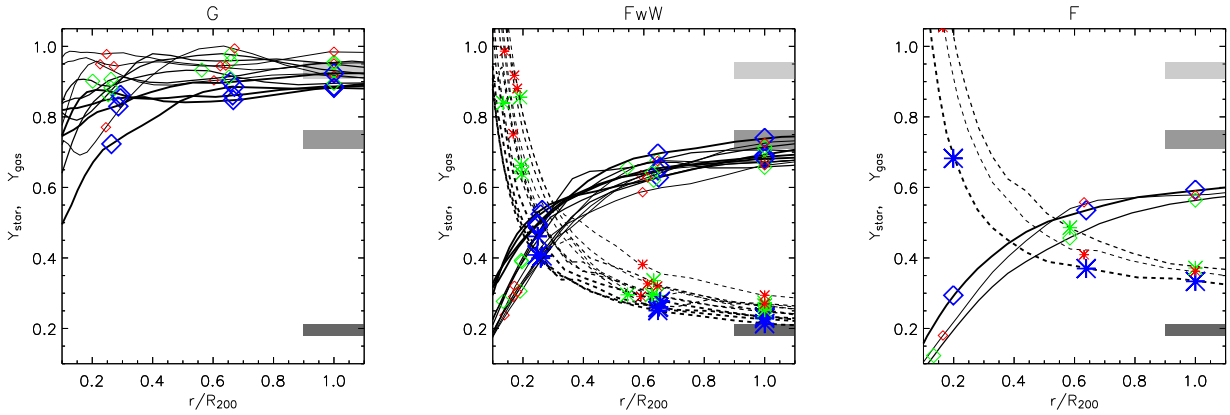

Figure 3. The comparison between the outputs of 3 different physical schemes out of the 6 investigated. The gas (solid line) and stellar (dashed line) mass fractions, normalized to the cosmic value, are plotted at $R_{2500}(\approx 0.3R_{200})$, $R_{500}(\approx 0.7R_{200})$ and R_{200}. Their evolution with redshift is indicated by the thickness of the lines (from thickest line/larger symbols to thinnest line/smaller symbols: $z = 0,\ 0.7,\ 1$). The shaded regions indicate the 1σ range of $Y_{\rm star}$, $Y_{\rm gas}$ and $Y_{\rm b}$ measured at R_{200} and $z = 0$ for the cluster set extracted from the cosmological box.

$z = 0$ with the estimates at other redshifts ($z_o = 0.7$ and 1; see, e.g., Fig. 3), we evaluate from equation 1

$$\frac{\Omega'_{\rm m} - \Omega_{\rm m}}{\Omega_{\rm m}} = \frac{\Delta\Omega_{\rm m}}{\Omega_{\rm m}} = \frac{1 + \phi(< R_\Delta, z = 0)}{1 + \phi(< R_\Delta, z = z_o)} - 1\,, \quad (3)$$

that is about -0.05. When $\phi = f_{\rm star}/f_{\rm gas}$ measured locally at R_{2500} is compared with the corresponding value at different redshifts, the deviation ranges between -0.74 (when winds are excluded) and -0.38 (when strong winds are present), whereas it is about -0.10 at R_{500}.

As for the runs with gravitational heating only the effect of the variation of $Y_{\rm b}$ with redshift and overdensity implies $\Delta\Omega_{\rm m}/\Omega_{\rm m} < +0.11$, thus comparable to the current statistical uncertainties from *Chandra* observations of the massive clusters out to $z = 1.3$ (Ettori et al. 2003, Allen et al. 2004). However, when the extra-physics of the radiative runs is included, $\Delta\Omega_{\rm m}/\Omega_{\rm m}$ has two contributions of $\approx +0.10$ and < -0.05, due to an increase with redshift of (1) $Y_{\rm b}$ (see Fig. 2) and (2) the stellar to gas mass fraction ratio (see Fig. 3). Both these effects are caused by a more efficient star formation in high redshift clusters.

In general, our results indicate that it may be dangerous to use simulations to calibrate observational biases for precision determination of cosmological parameters from the gas fraction in clusters. Although none of our simulation models includes a fair description of the actual ICM physics, it is interesting that different models provide different redshift–dependent corrections for the estimate of the cosmic baryon fraction from observations of the gas and star density distribution within clusters. If applied to observational data, such corrections would induce sizeable differences in the determination of the matter and dark energy density parameters.

ACKNOWLEDGMENTS
REFERENCES

[1] Allen S.W. et al., 2004, MNRAS, 353, 457

[2] Arnaud M., Pointecouteau E., Pratt G.W., 2005, A&A, 441, 893

[3] Borgani S. et al., 2004, MNRAS, 348, 1078

[4] Eke V.R. et al., 1998, ApJ, 503, 569

[5] Ettori S., Fabian A.C., 1999, MNRAS, 305, 834

[6] Ettori S., De Grandi S., Molendi S., 2002, A&A, 391, 841

[7] Ettori S., 2003, MNRAS, 344, L13

[8] Ettori S., Tozzi P., Rosati P., 2003, A&A, 398, 879

[9] Gardini A. et al., 2004, MNRAS, 351, 505

[10] Kirkman D. et al., 2003, ApJS, 149, 1

[12] Lin Y.T., Mohr J.J., Stanford S.A., 2003, ApJ, 591, 749

[12] Mazzotta P. et al., 2004, MNRAS, 354, 10

[13] Navarro J.F., Frenk C.S., White S.D.M., 1995, MNRAS, 275, 720

[14] Rasia E., Tormen G., Moscardini L., 2004, MNRAS, 351, 237

[15] Springel V., Hernquist L., 2003, MNRAS, 339, 289

[16] Springel V., 2005, MNRAS, in press (astro-ph/0505010)

[17] Tormen G., Bouchet F.R., White S.D.M., 1997, MNRAS, 286, 865

[18] White S.D.M. et al., 1993, Nature 366, 429

SEARCHING FOR SHARP SURFACE BRIGHTNESS DISCONTINUITIES: A SYSTEMATIC STUDY OF COLD FRONTS IN GALAXY CLUSTERS

S. Ghizzardi, S. Molendi, A. Leccardi, M. Rossetti

IASF Milano, Istituto Nazionale di Astrofisica, Milano, Italy

ABSTRACT

We perform a systematic search of cold fronts in a sample of 62 clusters observed with XMM-Newton with redshift ranging from 0.01 to 0.3. We detect one or more cold fronts in 21 (34%) of our objects. A large fraction (87.5%) of nearby clusters $0.01 < z < 0.04$ host a cold front while only 20% of the distant clusters, mostly merging clusters, do so. The absence of sharp surface brightness discontinuites in distant cool cores is most likely a consequence of the insufficent spatial resolution of our images. Some nearby cool core clusters show a dislocation between the surface brightness and the pressure peak. This implies that the cool central gas is displaced from the bottom of the gravitational potential well and likely sloshing.

Key words: cold fronts; clusters of galaxies; X-rays.

1. INTRODUCTION

The high spatial resolution of the Chandra X-ray telescope has led to the discovery of several phenomena within galaxy clusters. In particular, Chandra observations revealed the existence of very sharp discontinuities in the X-ray surface brightness of several clusters. The drop in the X-ray surface brightness is accompanied by a jump of similar magnitude in the gas temperature, so that the pressure does not change drastically across the front. This feature has been named "cold front" (Vikhlinin, Markevitch & Murray, 2001).

Cold fronts have been initially observed in merging clusters. The prototype cold fronts are hosted in A2142 (Markevitch et al., 2000), A3667 (Vikhlinin, Markevitch & Murray, 2001) and 1E0657-56 (Markevitch et al., 2002). In these clusters, the cold front delineates the edge of the cool core of the merging substructures which have survived the merger and is rapidly moving throughout the shock-heated ambient gas (Markevitch et al., 2000).

Cold fronts have been detected also in the core of some relaxed clusters (e.g. A1795: Markevitch, Vikhlinin & Mazzotta, 2001; RX J1720.1+2638: Mazzotta et al, 2001; A496: Dupke & White III, 2003; 2A 0335+096: Mazzotta, Edge & Markevitch, 2003). The presence of cold fronts in cool cores provides evidence of gas motions and possiblly of departures from hydrostatic equilibrium. Cold fronts represent a unique tool of investigation of the internal dynamics of clusters, especially in the regrettable absence of instrumentation capable of a direct detection of gas motions. To study and characterize cold fronts, we built a sample of 62 clusters observed with XMM-Newton and carried out a systematic search for surface brightness and temperature discontinuities. We studied the occurrence of cold fronts in different redshift ranges and for different types of clusters (merging and cool cores). Particular attention has been devoted to cold fronts in relaxed clusters.

The sample is described in §2. Technical details concerning the procedure used for searching cold fronts are given in §3. In §4, we discuss the occurrence of cold fronts in clusters. The nature of cold fronts in cool cores has been discussed in §5. Finally, in §6 we summarize our results.

2. THE DATA SAMPLE

We have performed a systematic search and characterization of cold fronts from a large sample of clusters observed with XMM-Newton. The large collecting area of the EPIC telescope onboard the XMM-Newton satellite allows a detailed inspection of the spectral properties of the galaxy clusters, which are important to study the dynamics of the core. Namely, we have selected a sample of 62 clusters of galaxies. The sample includes two different subsamples. The first comprises roughly 20 nearby bright clusters with redshifts in the range $[0.01 - 0.1]$. The second subsample comprises all the clusters available in the XMM-Newton public archive up to March 2005, having redshifts in the range $[0.1 - 0.3]$ (Leccardi et al., 2005; in preparation).

The sample (see Fig. 1) includes a wide variety of clusters, both merging and cool cores. It is worth noting that

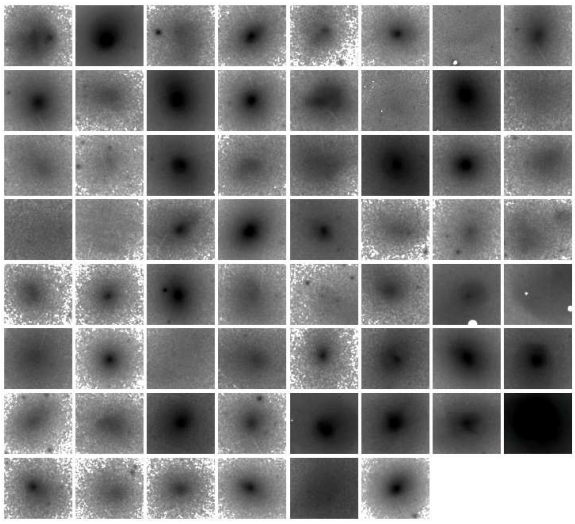

Figure 1. The EPIC surface brightness images for the 62 clusters in our sample. Flux is in units $10^{-15}\mathrm{erg\ cm^{-2}s^{-1}pixel^{-1}}$.

we did not fix an objective selection parameter to build our sample. However, the criteria used for the selection of the clusters are not related to the existence of the cold fronts. Hence, no bias is *a priori* present in our sample as far as cold fronts occurrence is concerned and for our purposes this sample is sufficiently representative of the cluster population up to redshift 0.3.

3. SEARCHING FOR COLD FRONTS.

To find cold fronts and to study their properties, we need accurate surface brightness and temperature maps and profiles. Profiles should be determined in different directions for each cluster. For clusters with good statistics, we have used the algorithm developed by the Milano group to build the maps. The procedure consists in binning the cluster images, using the adaptive binning algorithm developed by Cappellari & Copin (2003) and based on the Voronoi tessellation technique. The temperature (T) and the surface brightness (Σ) values in each bin are determined through a broad band fitting method (Rossetti et al., 2005; in preparation). Errors are determined for both Σ and T in each bin.

As an example, in Fig. 2 we show the maps obtained applying our procedure to the XMM-Newton observation of the galaxy cluster A496. In Fig. 2(a) and (b), we report respectively the EPIC (MOS + PN) surface brightness image and the surface brightness map derived using our procedure. In Fig. 2(c), the A496 temperature map is shown; the central cool core is clearly visible. The quality of the A496 observation is quite good, so the derived maps are very accurate and the surface brightness map is very similar to the surface brightness image.

Once the surface brightness and the temperature have been obtained, other thermodynamic quantities (pressure and entropy) can be derived. Although a deprojection procedure should be applied to derive these quantities, we work in the approximation that the surface brightness is $\Sigma \sim n^2$, where n is the electronic density. The (pseudo)-pressure and the (pseudo)-entropy are correspondingly derived through the projected quantities $P = \Sigma^{1/2}T$ and $S = T/\Sigma^{1/3}$. The (pseudo)-pressure map for A496 is reported in Fig. 2(d). A cold front at roughly 90 arcsec from the peak in the N-NW sector (roughly $60^\circ - 120^\circ$) is clearly observed in the surface brightness and temperature maps. The Σ and T (see Fig. 3) profiles in this sector show that the surface brightness has a sharp discontinuity (approximatively by a factor of 2-3) and that the temperature across the edge varies by a factor of 1.5. Correspondingly the pressure does not show an abrupt drop and there is approximate pressure equilibrium across the front.

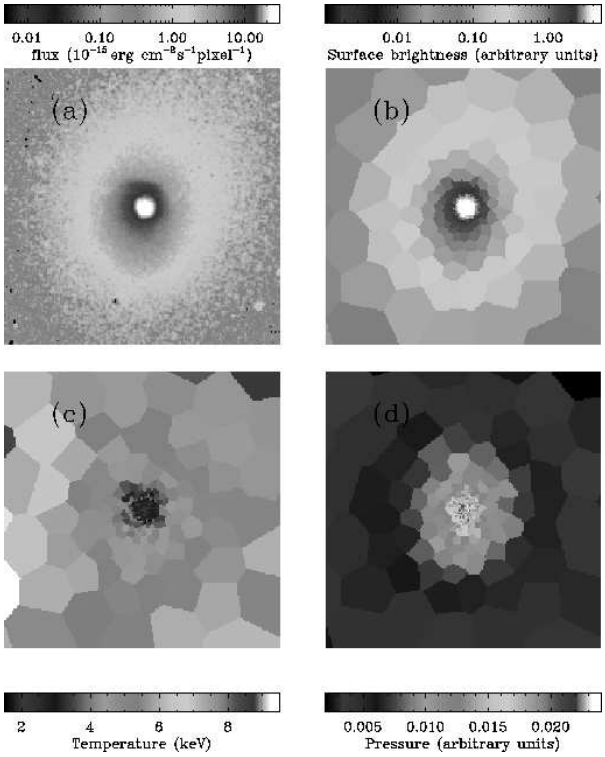

Figure 2. (a) EPIC surface brightness image for A496. (b) Surface brightness map, (c) temperature map and (d) pseudo-pressure map for A496.

Another cluster with high statistics is Centaurus. The surface brightness and the temperature profiles (in Fig. 4 (a) and (b) respectively) of the NE sector ($\sim 120^\circ - 150^\circ$) show that Centaurus hosts a cold front at $\sim$ 90 arcsec from the peak. The surface brightness drops by a factor of 4-5 and the temperature rises by almost a factor of 3. Also in this case the pressure is almost constant across the front.

For clusters having poor statistics the adaptive binning procedure does not allow us to produce detailed maps. Hence, for these clusters the broad band fitting method

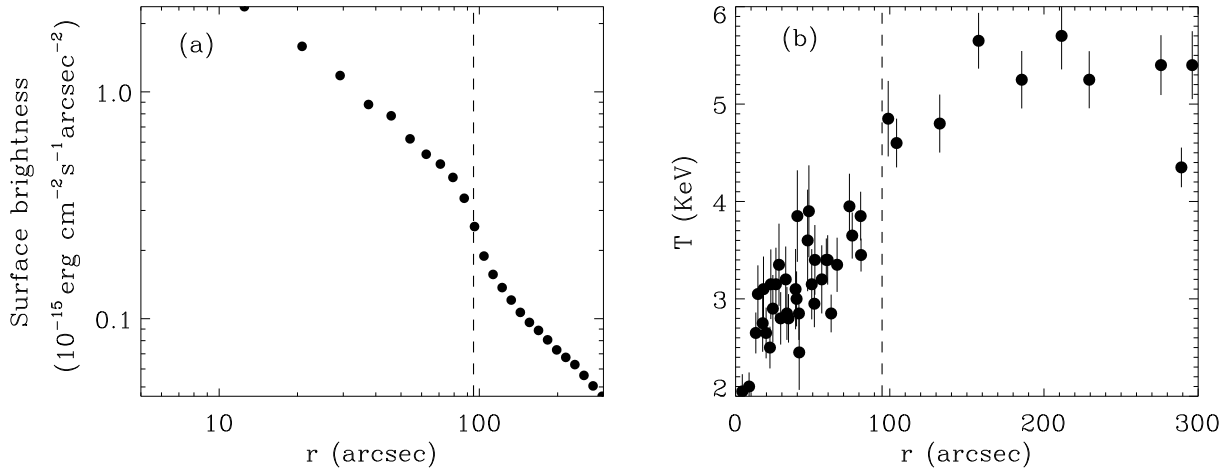

Figure 3. (a) Surface brightness profile and (b) temperature profile for A496. The profiles have been derived in the sector $60^\circ - 120^\circ$. *The dashed line marks the cold front position,* ~ 90 *arcsec from the peak.*

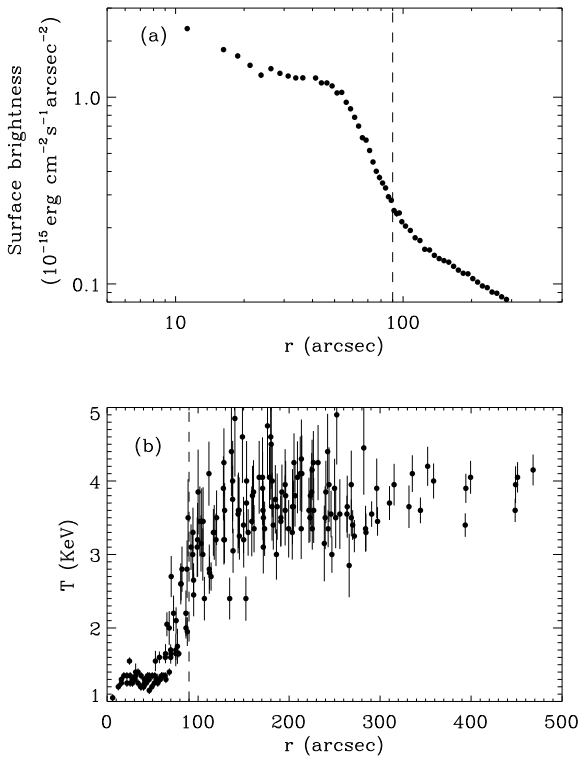

Figure 4. a) Surface brightness profile and (b) temperature profile for Centaurus. The profiles have been derived in the sector $120^\circ - 150^\circ$. *The dashed line marks the cold front position,* ~ 90 *arcsec from the peak.*

has been applied to manually selected macro regions. Regions are built in such a way as to follow the cold front feature so that the temperature profile across the cold front can be determined. This is the case of A1300, where a discontinuity in the surface brightness (see Fig. 5a) is detected at ~ 25 arcsec from the peak (in the W-NW direction). The temperature profile (Fig. 5b) is not as detailed as in the previous cases, nevertheless there is an indication of a temperature rise.

4. OCCURRENCE OF COLD FRONTS IN GALAXY CLUSTERS

The systematic analysis of the surface brightness of the clusters of our sample brought to the detection of cold fronts in 21 objects (and probably also in other 4 clusters where the presence of a cold front is not clear and needs some further investigation). This corresponds to a percentage of 34% (40% if the uncertain cases are also accounted) in the redshift range [0.01-0.3]. It is interesting to study also the frequency of cold fronts in different redshift ranges. Our analysis shows that if we progressively reduce the sample, excluding gradually the more distant clusters, the fraction of clusters having a cold front increases. In particular, in the subsample of the nearby clusters (with redshift in the [0.01-0.04] range), 87.5% of our objects exhibit one or more cold fronts. Considering that projection effects can hide a non-negligible fraction of cold fronts, such frequency implies that probably all the nearby clusters host one or more cold fronts. This result is in agreement with Markevitch, Vikhlinin & Forman (2002) who analyzed a sample of 37 relaxed nearby clusters observed with *Chandra* and find that roughly 70% of the nearby cool core clusters of their sample host a cold front (Markevitch, Vikhlinin & Forman, 2002).

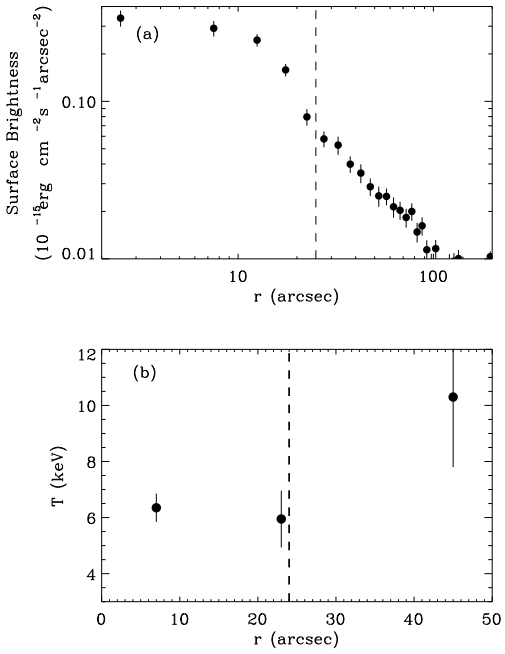

Figure 5. (a) Surface brightness profile and (b) temperature profile for A1300. The temperature profile have been derived applying the broad band fitting procedure to manually selected macro regions. The dashed line marks the cold front position, ~ 25 arcsec from the peak.

While cold fronts are a common feature in nearby clusters, either merging or cool cores, for distant clusters their frequency is different for different types of clusters. For clusters with redshift larger than 0.1, cold fronts are mostly detected in merging clusters, while only few cool core clusters exhibit one. Since cold fronts in cool cores are in general quite near to the peak and less prominent than in merging clusters, it is likely that the resolution of XMM-Newton is not enough to detect sharp discontinuities for this class of clusters at high redshifts.

5. THE COLD FRONTS IN RELAXED GALAXY CLUSTERS

Our sample includes a large number of nearby relaxed clusters and we have already shown that most of them host a cold front. The presence of a cold front in the center of cool core clusters is a clear indication that the ICM in these objects is not completely static. Several Chandra observations of clusters have revealed that relaxed clusters often have disturbed cores with complex morphological structure. Two major pictures have been proposed for cold fronts in cool core clusters. Markevitch, Vikhlinin & Forman (2002) proposed that the central cool gas is sloshing in the underlying gravitational potential well. In this scenario, the cold front is the boundary between the displaced cooler gas and the ambient hot gas. The gas could have been displaced by some AGN central activity or as a consequence of some past minor merging process (Markevitch, Vikhlinin & Forman, 2002; Markevitch, Vikhlinin & Mazzotta, 2001).

An alternative picture has been recently proposed by Tittley & Henriksen (2005). Using numerical simulations, the authors show how the oscillations of the dark matter (and correspondingly of the gravitational potential well) can produce cold fronts. In this scenario, it is the potential well that is oscillating and not the gas within it; the gas and the dark matter are oscillating together, since dark matter movement induces gas motions. The resulting compression of the isodensity contours along the oscillations generates the cold front feature.

A detailed analysis of cold fronts in relaxed clusters can help us improve our understanding of the nature of the phenomenon. We selected from our sample some cool core clusters. For most of them, the derived temperature and (pseudo)-pressure maps are detailed and allow a good inspection of the cool core physics.

2A 0335+096 is a cool core cluster with a cold front in the S-SW sector $\sim$ 60 arcsec from the peak (see also Mazzotta, Edge & Markevitch, 2003). In Fig. 6 we show the maps obtained applying our algorithm to the XMM-Newton data for 2A 0335+096. In Fig. 6(a) and (b), we show respectively the surface brightness and the temperature maps for the central region of the cluster. In Fig. 6(c) the (pseudo)-pressure is reported. Finally, in Fig. 6(d) the optical image of the central cD galaxy observed with HST is shown. This last image has been repeatedly zoomed in, for a better view of the galaxy, while the scales of the three images derived from XMM-Newton observation match each other. The crosshair is centered on the cD galaxy. The circle is an approximation of an isophote of the pressure image. The peak of the pressure perfectly matches the cD galaxy position, while the surface brightness peak and the temperature minimum are significatively displaced in the direction of the cold front (S-SW direction). The same analysis has been applied also to a *Chandra* observation of 2A 0335+096. The corresponding maps are reported in Fig. 7. The panels are as in Fig. 6. The displacement between the surface brightness and the pressure (or the cD galaxy) peak is even more evident here.

The mismatch between pressure and surface brightness can help improve our understanding of cold fronts. Both the gas pressure and the cD trace the gravitational potential of the cluster, while the surface brightness describes the X–ray emitting gas. The dislocation of the surface brightness peak in the direction of the cold front, indicates that the thermal gas is not at the bottom of the gravitational potential well, in agreement with a the sloshing scenario proposed by Markevitch, Vikhlinin & Forman (2002).

A1795 (see Fig. 8) shows a similar mismatch. This cluster has a cold front in the southern sector $\sim$ 70 arcsec from the peak. Markevitch, Vikhlinin & Mazzotta (2001)

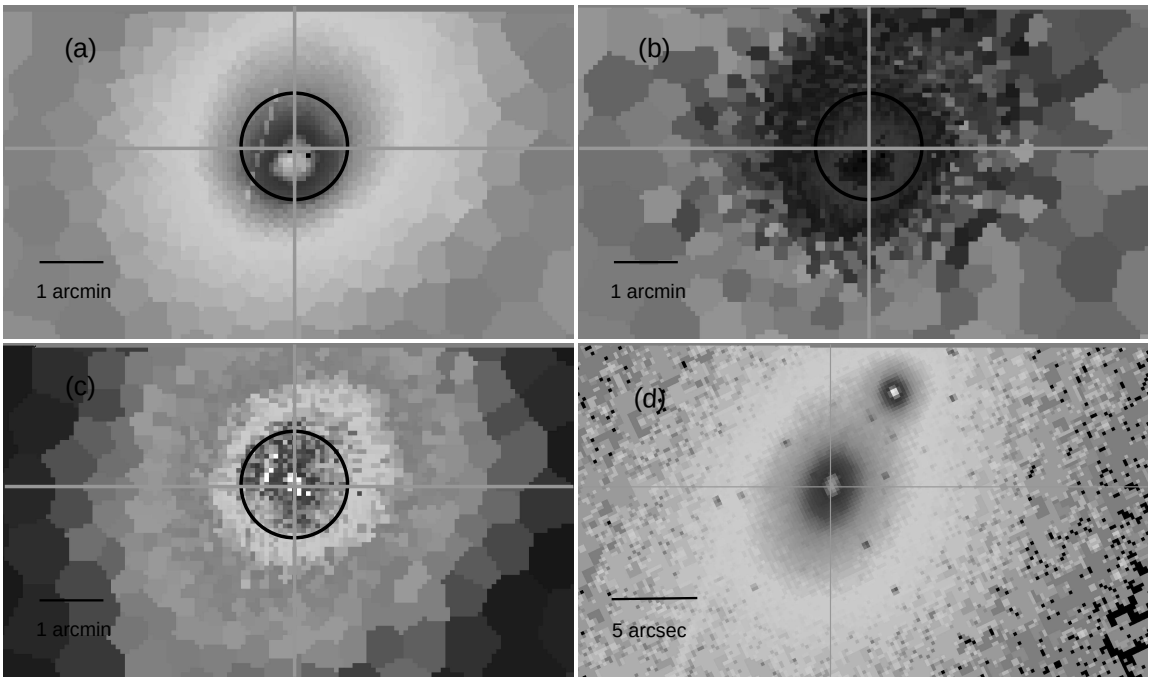

Figure 6. (a) Surface brightness (b) temperature and (c) pseudo-pressure maps for the core of 2A0335+096. The cold front is observed in the S-SW sector ~ 50 arcsec fron the peak. (d) Optical HST image of the central cD galaxy of 2A0335+096. Crosshairs are centered on the cD position. The circle approximates an isocontour in the pressure map. The pseudo-pressure peak matches the cD galaxy position, while the surface brightness and the temperature peaks are displaced in the direction of the cold front.

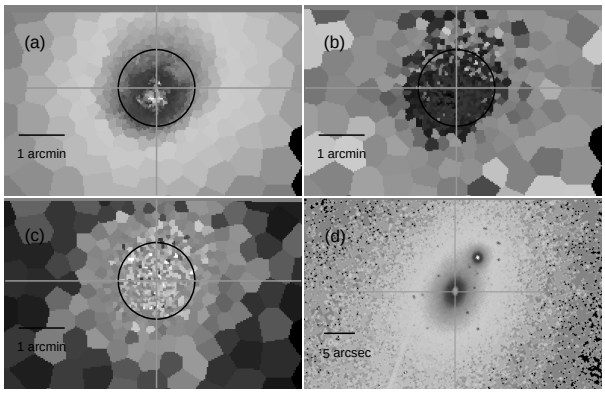

Figure 7. Maps for 2A0335+096 obtained from the analysis of a Chandra observation. Panels are as in Fig. 6. The displacement of the surface brightness peak in the direction of the cold front is even more evident here.

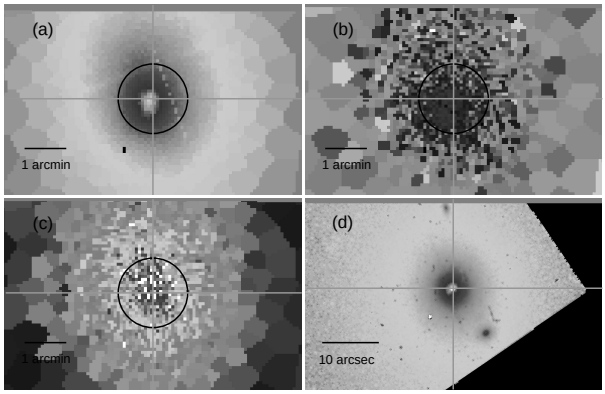

Figure 8. Maps for A1795. Panels are as in Fig. 6. The cold front is in the southern sector ~ 70 arcsec from the peak. The displacement of the surface brightness peak in the direction of the cold front can be observed.

propose that the sloshing gas is now at the maximum displacement from the peak with a zero velocity. The displacement from the bottom of the potential well is visible in Fig. 8 although it is less evident than in 2A 0335+096 maps. As for 2A 0335+096, the position of the cD (in the HST image) and the pressure peak match each other, while the surface brightness peak is displaced towards the southern direction.

A different picture emerges from the analysis of the clus-

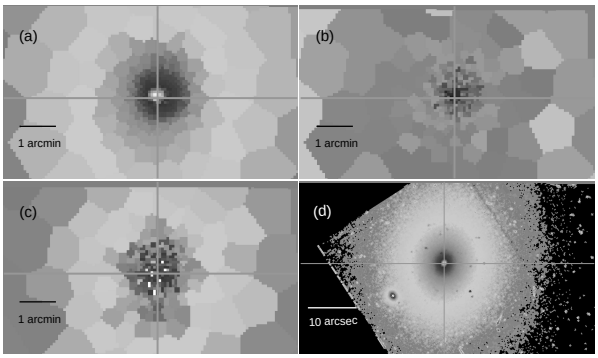

Figure 9. Maps obtained for A496. Panels are as in Fig. 6. The cold front is in the N-NW sector ~ 90 *arcsec from the peak. The displacement of the surface brightness peak in the direction is not observed, at the available resolution of* ~ 2 *kpc.*

ter A496 (see maps in Fig. 9). As already outlined in § 3, A496 is a cool core cluster and exhibits a cold front in the N-NW direction. Fig. 9 shows (at the available resolution ~ 2 kpc) no displacement between the surface brightness and the pressure (or the cD position). This is compatible with a Tittley-Henriksen picture where the dark matter and the ICM oscillate together. However, the Markevitch et al. picture is not ruled out: the oscillating gas may be observed just while passing in the center of the potential well.

At the present time, the analysis of these three clusters leaves room for both the scenarios described above. A systematic analysis of the temperature, pressure and metal maps for all the cool core clusters of the sample is needed to address the nature of this class of cold fronts.

6. SUMMARY

In the absence of instrumentation capable of detecting gas motions, cold fronts are our primary tool to study the internal dynamics of the ICM. We have selected a large sample including 62 galaxy clusters observed with XMM-Newton, having a redshift in the [0.01-0.3] range. The systematic search of surface brightness discontinuities has brought to the detection of cold fronts in 21 (34%) clusters of galaxies. Almost all the nearby clusters (either merging and cool cores) host a cold front while, as far as distant clusters are concerned, cold fronts are mostly detected in merging clusters and only few relaxed clusters host one. Probably, cold fronts are not detected in distant relaxed clusters because of the insufficient resolution of our observations.

Through the analysis of the surface brightness, temperature, (pseudo)-pressure maps for some cool core clusters we have outlined a method which can help us improve our understanding of this phenomenon. In some clusters, (e.g. 2A0335, A1795), the surface brightness peak (which describes the X–ray emitting gas) is displaced from the pressure (and the central cD) peak which traces the gravitational potential well. This is an indication that the thermal gas is displaced from the bottom of the potential well and probably is sloshing (see Markevitch, Vikhlinin & Forman, 2002). On the contrary, in A496 all the peaks (surface brightness, pressure and cD galaxy) match each other. This behavior favors the scenario proposed by Tittley & Henriksen (2005) where the dark matter itself (carrying the gravitational potential and the gas) is oscillating. This is also compatible with the Markevitch, Vikhlinin & Forman (2002) picture as the oscillating gas may be observed just while passing in the center of the potential well.

A systematic study of the dislocation of the surface brightness peak for all the relaxed clusters of our sample will help us address this issue.

REFERENCES

Cappellari M. & Copin Y. 2003, MNRAS, 342, 345

Dupke R. & White III R.E., 2003, ApJ, 583, L13

Leccardi A., et al. 2005, in preparation

Marchevitch M., et al. 2000, ApJ, 541, 542

Markevitch M., Vikhlinin A. & Mazzotta P. 2001, ApJ, 562, L153

Markevitch M., Gonzalez A.H., David L., Vikhlinin A., Murray S., Forman W.R., Jones C. & Tucker W. 2002, ApJ, 555, 205

Markevitch M., Vikhlinin A. & Forman W.R. 2002, *Matter and energy in clusters of galaxies*, ASP Conference Series, Vol. X, Eds. S. Bowyer & C.-Y. Hwang, astro-ph/0208208

Mazzotta P., Markevitch M., Vikhlinin A., Forman W.R., David L.P. & VanSpeybroeck L. 2001, ApJ, 555, 205

Mazzotta P., Edge A.C., Markevitch M. 2003, ApJ, 596, 190

Rossetti M., Ghizzardi S., Molendi S. & Finoguenov A. 2005, in preparation

Tittley E.R. & Henriksen M. 2005, ApJ, 618, 227

Vikhlinin A., Markevitch M. & Murray S.S. 2001, ApJ, 551, 160

CHANDRA OBSERVATION OF THE MOST INTERESTING CLUSTER IN THE UNIVERSE

M. Markevitch

Smithsonian Astrophysical Observatory

ABSTRACT

Chandra has recently observed 1E 0657–56, a hot merging system at $z = 0.3$ (the "bullet" cluster), for 500 ks. I present some of the findings from this dataset. The cluster exhibits a prominent bow shock with $M = 3.0 \pm 0.4$ (one of only two known $M \gg 1$ shock fronts), which we use for a first test of the electron-ion equilibrium in an intergalactic plasma. The temperatures across the shock are consistent with instant shock-heating of the electrons; at 95% confidence, the equilibration timescale is much shorter than the collisional Spitzer value. Global properties of 1E 0657–56 are also remarkable. Despite being extremely unrelaxed, the cluster fits well on the $L_X - T$ relation, yet its total mass estimated from the $M - T$ relation is more than twice the value measured from lensing. This is consistent with simulations predicting that in the middle of a merger, global temperature and X-ray luminosity may be temporarily boosted by a large factor.

Key words: galaxies: clusters: individual (1E0657–56) — plasmas — X-rays: galaxies: clusters.

1. INTRODUCTION

1E 0657–56 is the most interesting cluster in the Universe, as officially confirmed by *Chandra* Peer Review (Anonymous 2003). This system, located at $z = 0.3$, has the highest X-ray luminosity and temperature and the most luminous radio halo of all known clusters. It is also a spectacular merger occurring almost exactly in the plane of the sky (Markevitch et al. 2002), and contains one of only two known cluster shock fronts with a Mach number substantially greater than 1 (the other one is A520 with $M = 2$). *Chandra* has recently observed it with a 500 ks total exposure. The image from that dataset is shown in Fig. 1. It shows a prominent bow shock preceding a small, cool "bullet" subcluster flying west after passing through a core of a bigger cluster and disrupting it. In this paper, two interesting (preliminary) findings from this new dataset are presented, one regarding the global properties of the cluster, and another based on the high-resolution electron temperature profile across the shock front. All errors are 68%; the assumed cosmology is $h = 0.7$, $\Omega_0 = 0.3$ and $\Omega_\Lambda = 0.7$.

2. AN OVERHEATED CLUSTER

A single-temperature fit to the overall ACIS spectrum for the cluster (excluding a small region around the bullet for consistency with the "cooling flow corrected" temperatures for nearby clusters) is $T = 14.1 \pm 0.2$ keV. As shown in Fig. 2, it fits perfectly on the $L_X - T$ relation for local clusters (Markevitch 1998) after a correction for its redshift evolution (Vikhlinin et al. 2002). However, its total mass estimated from an X-ray $M_{500} - T$ relation (Vikhlinin et al. 2005b; Kotov & Vikhlinin 2005), $M_{500} = 1.9 \times 10^{15} M_\odot$, is a factor of 2.4 higher than the value within the same radius estimated from weak lensing (Clowe et al. 2004). Given the ongoing violent merger, this is not unexpected — simulations have predicted (Randall et al. 2002; Rowley et al. 2004) that during a major merger, the cluster may experience a transient

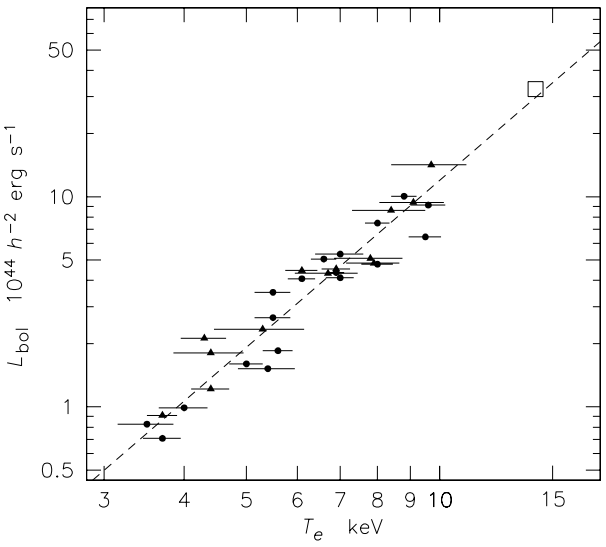

Figure 2. 1E 0657–56, shown as open square, overlaid on the local $L_X - T$ relation, after a correction of L_X of this cluster for redshift evolution of the relation.

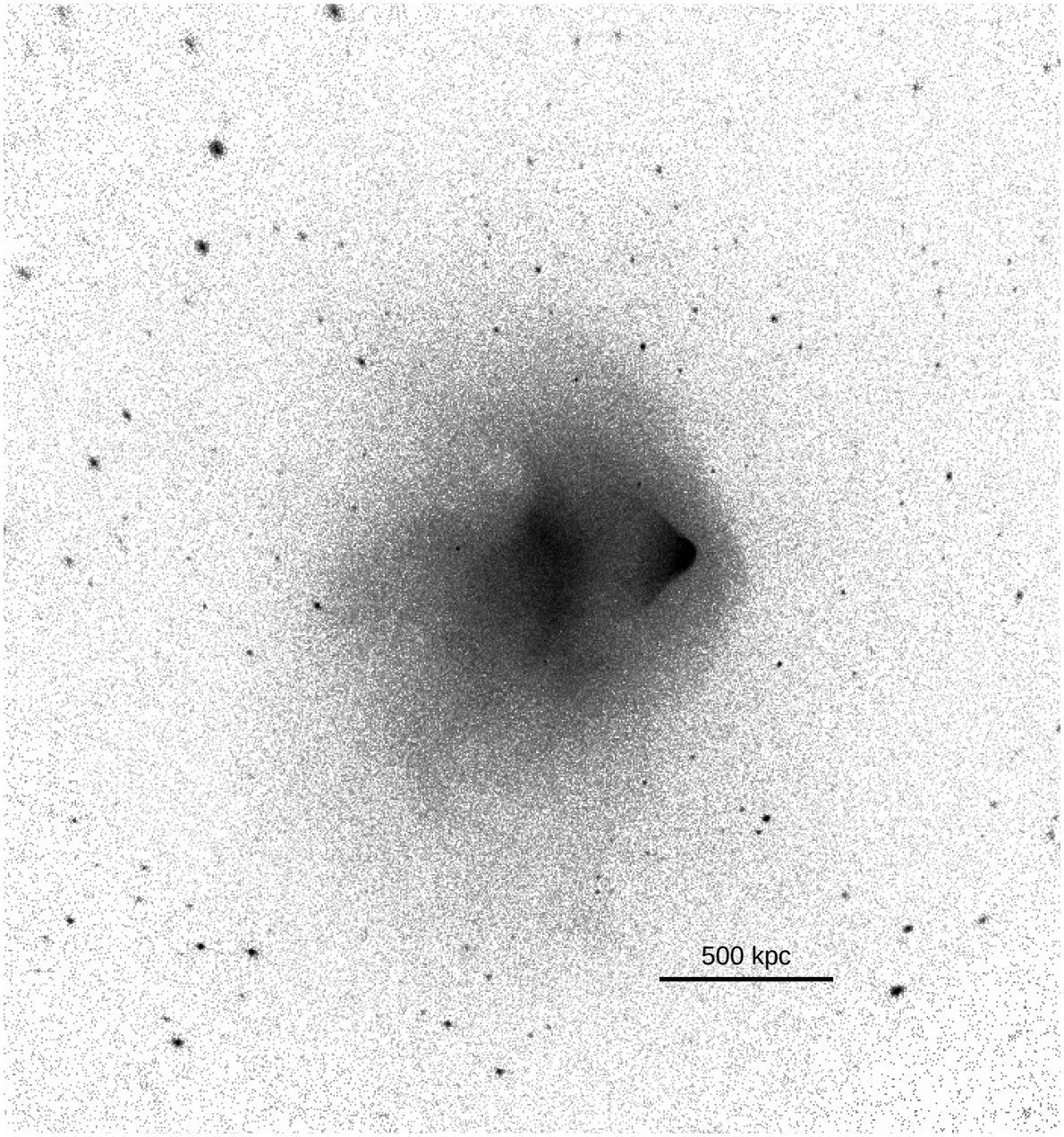

Figure 1. 500 ks Chandra ACIS-I image of 1E 0657–56 in the 0.8–4 keV band.

boost of temperature by a factor of several, lasting of order 0.1 Gyr around the moment of the subcluster core passage. In the course of this rapid change, the cluster moves approximately along the $L - T$ relation. We know from the shock velocity (Markevitch et al. 2002) that the core passage in 1E 0657–56 has indeed occurred about 0.15 Gyr ago, so this cluster appears to illustrate precisely this short-lived phenomenon.

It is interesting to try and recover a "pre-merger" temperature of the main subcluster. The gas before (west of) the shock front should not yet know anything about the merger, and stay undisturbed in the gravitational potential of the main cluster. We have therefore divided the cluster into the post-shock and pre-shock regions (approximately along the bow shock) and extracted radial temperature profiles in these regions, both centered at the mass centroid of the main subcluster (Clowe et al. 2004). The resulting profiles are shown in Fig. 3. If before the merger, the main cluster had a declining radial profile similar to that in most clusters (Vikhlinin et al. 2005a), extrapolating the "pre-shock" profile inwards would give an average temperature around 10 keV or less, compared to the present 14 keV. For such a temperature, M_{500} from the $M - T$ relation is within a factor of 1.5 of the lensing mass, which is within the uncertainty of the Clowe et al. (2004) lensing measurement. (The lensing mass would imply $T \simeq 8$ keV.)

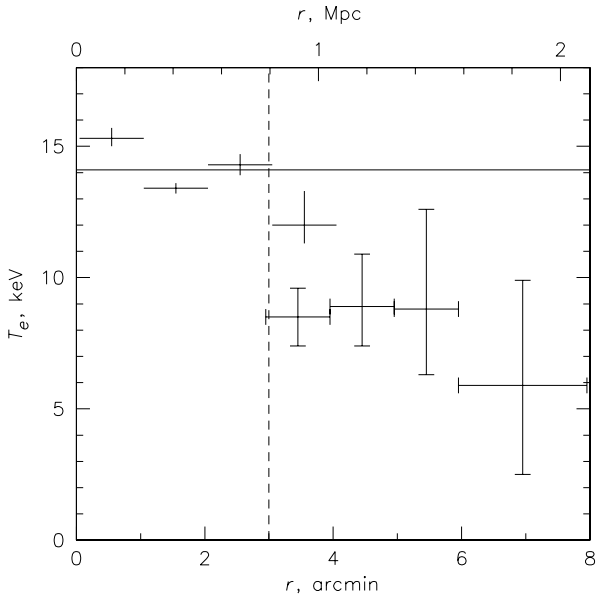

Figure 3. Radial temperature profiles for the disturbed region behind the shock (crosses without bars) and for the undisturbed region in front of the shock (barred crosses). Both profiles are centered on the main subcluster. The vertical dashed line approximately shows the shock front; the horizontal line is the average temperature.

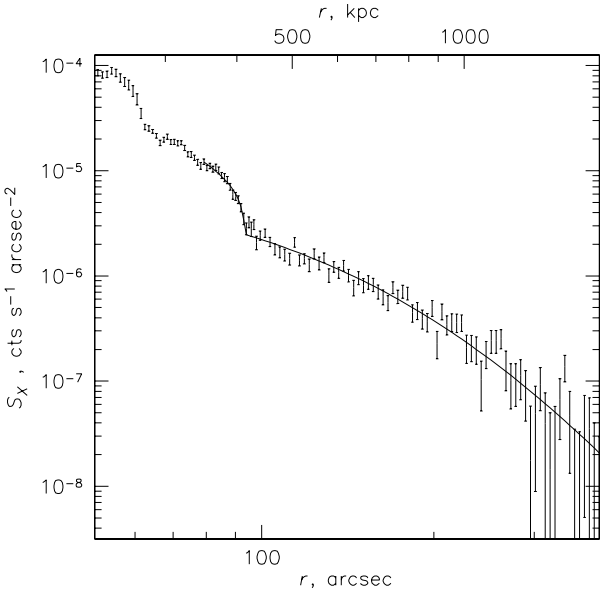

Figure 4. X-ray brightness profile across the shock front. The line shows the best-fit model (a projected sharp spherical density discontinuity at the shock).

The "overheated" cluster 1E 0657–56 may thus serve as a cautionary example for projects involving X-ray surveys of distant clusters, where total masses are proposed to be derived from low-statistics X-ray data using temperature profiles, average temperatures or even fluxes. If 1E 0657–56 was placed at $z = 1$ and observed with *Chandra* with a modest 100 ks exposure, its extremely unrelaxed state would be very difficult to detect from the X-ray image, especially if the merger was not oriented so fortunately in the plane of the sky. Its total mass would then be significantly overestimated.

3. ELECTRON-ION EQUILIBRIUM

The bow shock in 1E 0657–56 offers a unique experimental setup to determine whether electrons in the intracluster plasma are directly heated by shocks, or compressed adiabatically and then heated to an equilibrium temperature via collisions with protons (that are heated dissipatively by the shock). The collisional equilibration occurs on a Spitzer timescale (e.g., Zeldovich & Raizer 1966)

$$\tau_{\rm ep} = 2\times10^8\ {\rm yr}\left(\frac{n_e}{10^{-3}\ {\rm cm}^{-3}}\right)^{-1}\left(\frac{T_e}{10^8\,{\rm K}}\right)^{3/2} \qquad (1)$$

(note that, conservatively for our measurement, this is 3 times shorter than the formula given in Sarazin 1988). We cannot measure T_i in X-rays, only T_e. However, because the shock in 1E 0657–56 propagates in the plane of the sky, we can accurately measure the gas density jump across the front and use it to predict the post-shock adiabatic and shock-heated (dissipative) electron temperatures from the pre-shock temperature (using the adiabat and the Rankine-Hugoniot jump conditions, respectively), and compare it with the observation. Furthermore, we also know the downstream velocity of the shocked gas flowing away from the shock. This flow effectively unrolls the time dependence of the electron temperature along the spatial coordinate for us. The Mach number of the shock is conveniently high, so that the adiabatic and dissipative electron temperatures are sufficiently different for us to distinguish (e.g., for $M \lesssim 2$, they would be almost the same). It is also not a strong shock, for which the density jump would just be a factor of 4 (for ideal monoatomic gas) and would not let us directly determine M. Furthermore, the distance traveled by the post-shock gas during the time given by eq. (1), $\Delta x \simeq 230$ kpc $= 50''$, is well-resolved by *Chandra*. The statistical quality of the 500 ks dataset is just sufficient — in fact, this test was the main science driver for this long observation.

Fig. 4 shows a 0.8–4 keV surface brightness profile in a narrow sector across the shock, centered on the center of curvature of the front. The inner bump is the bullet (its boundary is a "cold front"). The edge at $90''$ is the shock front. There is also a subtle secondary edge between these main features, which may also be seen in the deep image. It is unrelated to the shock, so we should take care to exclude it from any fits aimed at deprojecting the shock temperatures and densities. The line in Fig. 4 shows a best-fit model consisting of the projected abrupt spherical density jump at the shock (by a factor of 3.0), a power-law profile inside the shock and a beta-model outside. The fit is perfect (the inclusion of the secondary edge does not affect it). From this density jump, we de-

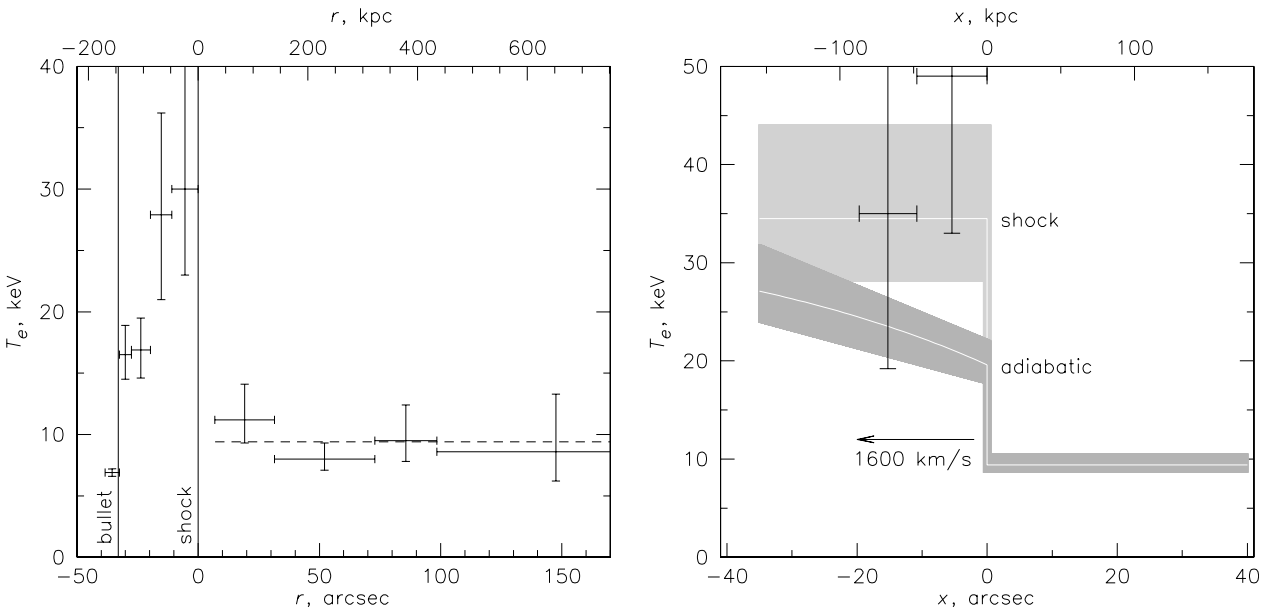

Figure 5. Left: projected temperature profile in a narrow sector across the shock. Two crosses in the shock region with lower temperatures correspond to an apparent additional edge-like structure and are not used. Vertical lines show the boundaries of the cool bullet and the shock; dashed line shows the average pre-shock temperature. Right: deprojected temperatures for the two post-shock bins overlaid on the model predictions (with error bands) for shock-heated and adiabatic electron temperatures. The velocity shown is for the post-shock gas relative to the shock.

termine $M = 3.0 \pm 0.4$, which corresponds to a shock (and bullet) velocity of 4700 km s^{-1}.

In Fig. 5 (left), we show a projected temperature profile in the same sector across the shock. There is a clear jump of the electron temperature. At the secondary edge mentioned above, the temperature goes down, which probably indicates residual cooler gas from the subcluster located ahead of the bullet. Therefore, we can only use the two bins closest to the front. Because we know the gas density profile across the shock, we can accurately subtract the contributions of the cooler pre-shock gas projected into the post-shock bins, assuming spherical symmetry. The large brightness contrast at the shock helps make this subtraction robust.

The deprojected values are shown in Fig. 5 (right). They are overlaid on the two models (gray bands), one assuming instant equilibration (i.e., electrons are heated at the shock), and another assuming adiabatic compression and subsequent equilibration with protons on a timescale given by eq. 1. (The plot assumes a constant post-shock gas velocity, which of course is not correct, but we are only interested in the immediate shock vicinity.) The deprojected gas temperatures are so high for *Chandra* that only their lower limits are meaningful. The temperatures are consistent with instant heating; the "adiabatic" model with the Spitzer timescale is excluded at a 95% confidence.

A few sanity checks have been performed. The high temperatures are not an artifact of the deprojection, because the projected temperatures in those two bins are already higher than the models. We also considered the possibility of a non-thermal contamination. The cluster is known to possess a radio halo (Liang et al. 2000) which has an edge right at the shock front (Markevitch et al. 2002). Therefore, there may be an inverse Compton contribution from relativistic electrons accelerated at the shock. However, the power-law spectrum of such emission for any M would be *softer* than thermal, so should not bias our measurements high. We also extracted a temperature profile in another sector of the shock (away from the nose), where $M \simeq 2$, and made a similar comparison. The recovered post-shock temperatures are lower than those in Fig. 5 and again in agreement with the model predictions (either one; for such M, the difference between them is very small). Thus, albeit at a relatively low significance (95%), we conclude that the electron-ion equilibration should be much faster than collisional.

It is of course unfortunate that a cluster with such a perfect geometric setup and a Mach number is so hot that *Chandra* can barely measure the post-shock temperatures; however, there is no choice of other shock fronts and so improvement upon the above measurement is unlikely in the near future.

There hasn't been a measurement of the electron-ion equilibration timescale in the intergalactic medium before. In the solar wind plasma, the equilibration is believed to be fast compared to the collisional timescale. For supernova remnants, which have strong shocks, conclusions vary between different objects (e.g., Rakowski 2005). Plasma interactions have been suggested as a fast equilibration mechanism for the solar wind, and it probably applies for the intracluster plasma as well.

4. SUMMARY

From the extra-long 500 ks *Chandra* observation of 1E 0657–56, we found that this cluster is observed at a very special, short-lived stage, when its temperature and luminosity are temporarily boosted by the merger by significant factors. The total cluster mass estimate from the X-ray $M - T$ relation turns out to be more than two times higher than the (presumably) true mass determined by lensing, indicating a very strong deviation from hydrostatic equilibrium. If this cluster were at high z and not so well exposed, it would be difficult to detect its disturbed state, thus it is a cautionary example for future high-z surveys.

The temperature profile across the shock offers a first test of the electron-ion equilibrium in the intracluster plasma. The temperatures indicate that electrons are indeed quickly heated at the shock. The slow Spitzer (collisional) equilibration rate is excluded at the 95% confidence.

This unique cluster, well-exposed by *Chandra*, is the subject of several other ongoing studies, the results of which will be reported soon.

REFERENCES

Clowe, D., Gonzalez, A., & Markevitch, M. 2004, ApJ, 604, 596

Kotov, O., & Vikhlinin, A. 2005, astro-ph/0511044

Liang, H., Hunstead, R. W., Birkinshaw, M., & Andreani, P. 2000, ApJ, 544, 686

Markevitch, M. 1998, ApJ, 504, 27

Markevitch, M., Gonzalez, A. H., David, L., Vikhlinin, A., Murray, S., Forman, W., Jones, C., & Tucker, W. 2002, ApJ, 567, L27

Rakowski, C. E. 2005, Adv. Space Research, 35, 1017

Randall, S. W., Sarazin, C. L., & Ricker, P. M. 2002, ApJ, 577, 579

Rowley, D. R., Thomas, P. A., & Kay, S. T. 2004, MNRAS, 352, 508

Sarazin, C. L. 1988, X-ray emission from clusters of galaxies (Cambridge University Press)

Vikhlinin, A., VanSpeybroeck, L., Markevitch, M., Forman, W. R., & Grego, L. 2002, ApJ, 578, L107

Vikhlinin, A., Markevitch, M., Murray, S. S., Jones, C., Forman, W., & VanSpeybroeck, L. 2005a, ApJ, 628, 655

Vikhlinin, A., et al. 2005b, astro-ph/0507092

Zeldovich, Y. B., & Raizer, Y. P. 1967, Physics of Shock Waves (New York: Academic Press)

THE XMM-NEWTON DISTANT CLUSTER PROJECT

G. Lamer[1], A. Schwope[1], H. Böhringer[2], R. Faßbender[2], P. Schuecker[2], C. Mullis[3], and P. Rosati[4]

[1]Astrophysikalisches Institut Potsdam, Potsdam, Germany
[2]Max Planck Institut für Extraterrestrische Physik, Garching, Germany
[3]University of Michigan, Ann Arbor, USA
[4]European Southern Observatory, Garching, Germany

ABSTRACT

We report on an ongoing search for distant clusters of galaxies in archival XMM-Newton observations. The aim of the survey is to establish a sample of ~ 30 clusters at redshifts $z > 1$. Here we describe the strategy of the survey from X-ray source detection to optical follow up observations of distant cluster candidates. First results of a pilot survey and the discovery of the most distant X-ray selected cluster at z=1.4 are presented.

Key words: clusters of galaxies; extragalactic surveys; X-rays.

1. INTRODUCTION

Clusters of galaxies are key probes of cosmic structure formation. Their evolution and space distribution is very sensitive to the cosmological framework and therefore measuring their density out to cosmological distances provides strong constraints to cosmological parameters as the matter density parameter Ω_m and the amplitude parameter σ_8 (e.g. Henry 2000, 2004, Schuecker et al. 2003). Samples used for these cosmological studies have to be large and well defined, at the same time probing higher redshifts greatly improves the levarage to constrain the cosmological parameters.

X-ray selection has several advantages for cosmological cluster surveys: The X-ray luminosity of a cluster is tightly correlated with its total mass, the most fundamental parameter (Reiprich & Böhringer 2002). Since the cluster X-ray emission is strongly peaked at the dense core, X-ray selection reduces projection effects as compared to optical surveys.

Other important applications of distant cluster samples are the investigation of galaxy evolution in the dense environment of clusters (e.g. Yee et al. 1996, Dressler et al. 1999) and the evolution of the X-ray emitting intracluster gas (e.g. Ettori et al. 2004).

So far only few clusters at redshifts $z > 1$ are known. Before we started of this project only 5 X-ray selected clusters in this range were known (Stanford et al. 1997, Rosati et al. 1999, Stanford et al. 2002, Rosati et al. 2004, Hashimoto et al. 2004), all of them selected from deep pointed ROSAT observations.

With the launch of *XMM-Newton* the prospects of finding distant X-ray selected clusters have dramatically increased. The large effective areas of the EPIC cameras provide sensitivities for cluster detection in typical observations ($\sim 10^{-14} erg/(s\ cm^2)$ in 20 ksec), which are comparable to those in the deepest ROSAT fields. At the same time the spatial resolution of the EPIC cameras is sufficient over the whole field of view ($r \sim 12'$) to identify even the most distant clusters of galaxies based on their extended emission.

The identification of galaxy clusters from *XMM-Newton* observations has only just begun (e.g. Romer et al. 2001, Willis et al. 2005, Schwope et al. 2004), recently the first discoveries of $z > 1$ clusters have resulted from the project described here (Mullis et al. 2005) and have been reported by the XMM-LSS project (Pierre 2005).

2. THE XMM-NEWTON DISTANT CLUSTER PROJECT

2.1. X-ray data analysis

The *XMM-Newton* data used for our survey are retrieved from the *XMM-Newton* public archive operated by ESAC. The observations are selected by a minimum EPIC exposure time of 10 ksec at galactic latitudes $|bII > 20^\circ|$. The EPIC images are furthermore inspected for their suitability to detect faint extended sources (i.e. they must be free of very bright target point sources and very extended sources dominating the image.) Presently more than 600

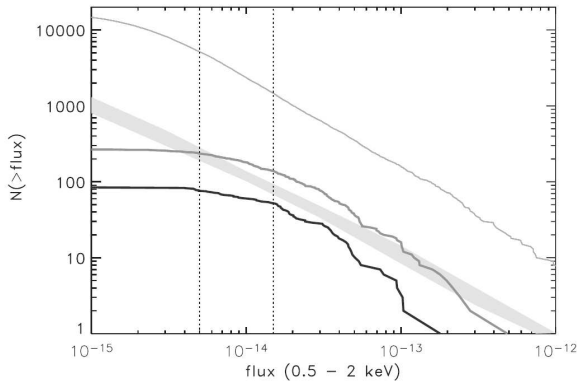

Figure 1. Number counts in the first 12 deg^2 of the survey. Upper line: all sources, middle line: all extended sources, lowest line: Distant cluster candidates (without optical counterparts). The shaded band indicates the cluster logNlogS derived by Rosati et al. (2002) from the RDCS.

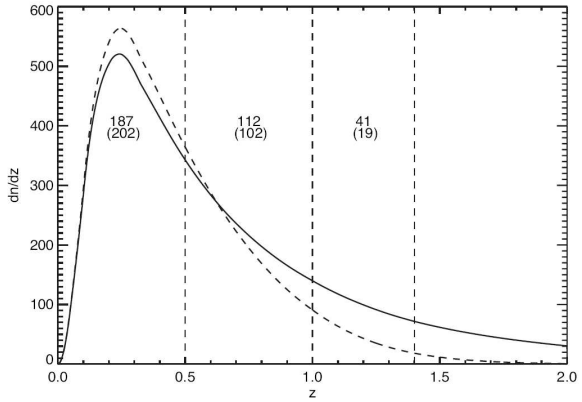

Figure 2. Expected redshift distribution of a 14 deg^2 XMM survey based on the results of the RDCS and 160 deg^2 ROSAT surveys (Rosati et al. 2002, Mullis et al. 2004. The solid line gives the expectations for no evolution and the dashed line and the values in brackets give a realistic prediction including evolutionary effects. (Böhringer et al. 2005)

such observations have been downloaded and processed. We reprocess the data from ODFs with the latest SAS release and apply a strict background flare screening algorithm in order to obtain optimum data quality and sensitivity for source detection.

The images of the 3 cameras are binned into the standard energy bands (0.2-0.5, 0.5-1.0, 2.0-4.5, 4.5-12. keV). For extended source detection we use the standard XMM-SAS source detection package, which uses a sliding-box algorithm (*eboxdetect*) for source detection and PSF-fitting (*emldetect*) for source characterisation. The extent of the sources is determined by fitting a King-profile convolved with the calibration PSF to the source images. Detection and PSF-fitting are performed simultaneously on the 15 (3 cameras $\times$ 5 energy bands) EPIC images in order to reach maximum sensitivity. Simulations of EPIC images including point sources and extended sources show that the source detection method can reliably detect the extent with core radii down to ~ 4 arcseconds and $0.5 - 2$ kev fluxes of $< 10^{-14}\mathrm{erg}/(\mathrm{s\ cm}^2)$ in a typical observation of 20 ksec observation time.

Figure 1 shows the flux distribution in the first 12 deg^2 of the survey, which is consistent with the flux limits derived by the simulations.

The last step of the X-ray data analysis is a visual screening of all extended sources detected by the software in order to remove any spurious extent detection, e.g. in the vicinity of bright point sources, large extended sources or due confusion of several closely spaced point sources.

2.2. Optical follow up observations

Since most new galaxy clusters detected by *XMM-Newton* are expected to have redshifts below z=0.5 (see Figure 2), a strategy is needed to efficiently separate the numerous low redshift clusters from the high-z candidates. We have therefore developed the following method for optical follow up:

The first step is an inspection of second-epoch red digitized sky survey (DSS) images of the X-ray source positions. Most extended X-ray sources outside the galactic plane are clusters of galaxies. Exceptions are nearby galaxies, which can be easily identified on the DSS images. Also low redshift clusters are visible on these images, we have determined that most clusters below $z = 0.5$ are detected on red DSS images. We therefore select only candidates, which appear as blank fields in the DSS for further optical follow-up.

A very efficient method to further classify the remaining candidates is to obtain imaging in the R and z band. Here we make use of the very good red sensitivity of FORS-2 at the ESO VLT. Snapshot images of 20 min in R and 8 min in z are deep enough to detect cluster galaxies out to redshifts of more than z=1.4 and at the same time give us a photometric redshift estimate via the red-sequence technique (Gladders & Yee 2000). The accuracies of the photometric redshifts are expected to of the order $\Delta z = 0.1$. Therefore a spectroscopic confirmation of all candidates with $z > 0.9$ will allow us to identify a complete sample of $z > 1$ clusters.

3. RESULTS OF A PILOT SURVEY

In order to demonstrate the feasibilty of our survey strategy we have undertaken the optical identification of a pilot survey after the first 160 XMM observations had been processed. The effective survey area, where the sensi-

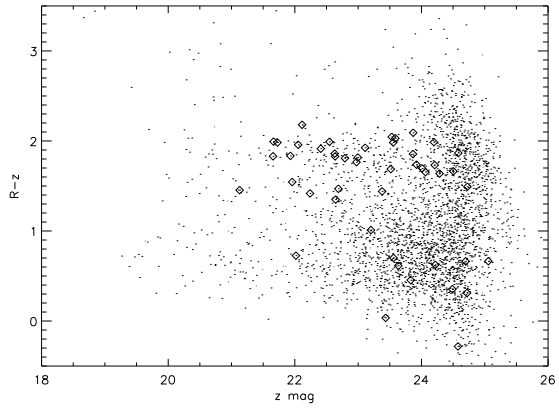

Figure 3. Colour-magnitude diagram of a rich cluster counterpart. Diamonds correspond to galaxies within 30 arcsec of the X-ray position. The red sequence indicates a redshift of $z \sim 1$.

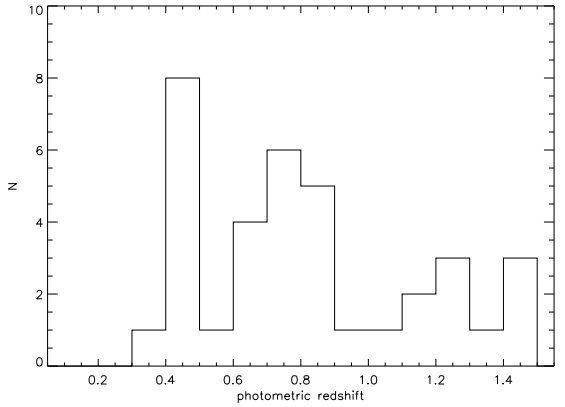

Figure 4. Distribution of photometric redshift derived from the R and z snapshot imaging. Among 36 clusters with a good photometric redshift are 10 candidates for $z > 1$ clusters.

tivity for extended sources exceeded $10^{-14} erg/(s\ cm^2)$, was $\sim 9\ \mathrm{deg}^2$. A total number of 155 extended sources were detected in these fields. After inspection of the source positions on DSS images, we selected 47 positions for R and z band imaging with the VLT in ESO periods P72 and P73. The limiting magnitude of the imaging was typically R=25 and z=24. In most cases a red sequence was detected and a redshift estimate could be derived.

Figure 3 shows an example colour-magnitude plot of a rich cluster at $z \sim 1$ found in the snapshot imaging.

Among the clusters with a photometric redshift are 10 candidates, where the red sequence indicates a redshift $z \geq 1$ (see Figure 4). This result is in good agreement with the prediction of 1 cluster per square degree. The highest estimated redshifts in the sample are $z \sim 1.5$.

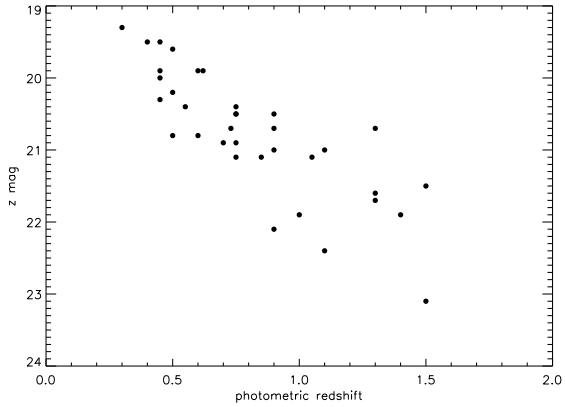

Figure 5. Photometric redshifts vs. z magnitudes of the brightest galaxy on the red sequence.

4. AN X-RAY SELECTED CLUSTER AT Z=1.4

One of the most promising candidates of the pilot survey (XMMU J2235.3-2557) has been observed spectroscopically with FORS-2 at the ESO VLT. Its red sequence colour R-z = 2.1 indicated a redshift of $z \sim 1.4$. The spectraoscopy confirmed this estimate with a $z = 1.393$, based on concordant redshifts of 12 member galaxies (Figure 6, Mullis et al. 2005).

From the measured X-ray flux of XMMU J2235.3-2557 $f_X = 3.6 \cdot 10^{-14} \mathrm{erg(cm^2)s}$ (0.5-2 kev) follows a luminosity of $L_X = 3 \cdot 10^{44} \mathrm{erg/s}$. Together with the X-ray temperature estimate of $6.0^{+2.5}_{-1.8}$ keV this results in a mass estimate of $3 \cdot 10^1 4 M_\odot$. This makes XMMU J2235.3-2557 not only the most distant X-ray cluster, but probably also the most massive distant cluster known so far.

5. CONCLUSIONS

Our pilot survey has shown that our search strategy is very efficient to find very distant clusters with a moderate requirement of telescope time. The relatively short snapshot exposures with the VLT have been proven to be sufficient to detect cluster galaxies and provide redshift estimates up to $z \sim 1.5$. The confirmation of the photometric redshift for XMMU J2235.3-2557 demonstrates the power of the R - z red sequence technique in this redshift range. About tree quarters of the newly deteced XMM clusters can be rejected based on DSS imaging. Of the remaining sources, about one quarter are candidates for $z > 1$ clusters. This is in very good agreement with the predicted surface density of ~ 1 per square degree. In order to construct a larger sample of very distant clusters (~ 50 objects), the large area of an XMM serendipity survey is clearly needed. Our next goal is to use the survey strategy outlined here in order to establish a sample of 30 $z > 1$ clusters in the southern sky.

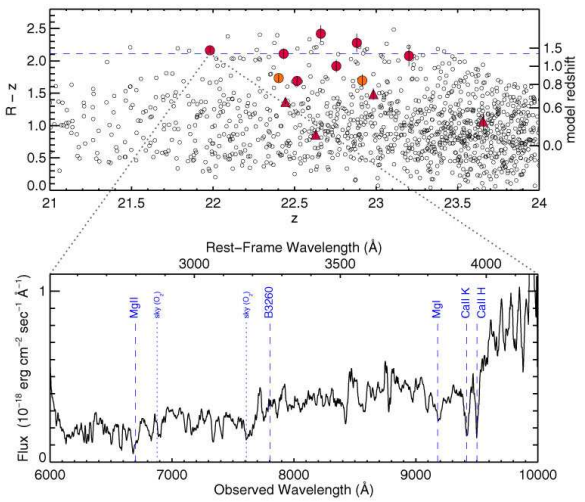

Figure 6. Top: Colour magnitude diagram of XMMU J2235.3-2557, indicating a redshift of $z \sim 1.4$, the filled circles indicate spectroscopically confirmed member galaxies. Bottom: VLT spectrum of the brightest cluster galaxy at $z = 1.39$.

REFERENCES

Böhringer, H., Mullis, C., Rosati, P., et al., 2005, The Messenger, 120, 33

Dressler, A., Smail, I., Poggianti, B., et al. 1999, ApJS, 122, 51

Ettori, S., Tozzi, P., Borgani, S., Rosati, P., 2004, A&A, 417, 13

Gladders, M. & Yee, H., 2000, AJ, 120, 2148

Hashimoto, Y., Barcons, X., Böhringer, H., et al., 2004, A&A, 417, 819

Henry, J.P, 2000, ApJ, 534, 565

Henry, J.P, 2004, ApJ, 609, 603

Mullis, C.R., Rosati, P., Lamer, G., et al. 2005, ApJ, 623, L85

Pierre, M., 2005, this volume

Reiprich, T.H., and Böhringer 2002, ApJ, 567, 716

Rosati, P., Stanford, S.A., Eisenhardt, P.R., et al., 1999, AJ, 118, 76

Rosati, P., Borgani, S., Colin, N., 2002, ARA&A, 40, 539

Rosati, P., et al., 2004, AJ, 127, 230

Schuecker, P., et al. 2003, A&A, 402, 53

Schwope, A., Lamer, G., Burke, D., et al. 2004, Adv. Space Res., 34, 2604

Stanford, S.A., Elston, R., Eisenhardt, P.R., et al., 1997, AJ, 114, 2232

Stanford, S.A., Holden, B., Rosati, P., et al., 2002, AJ, 123, 619

Willis, J.P., Pacaud, F, Valtchanov, I., et al., 2005, MNRAS, in press

Yee, H., Ellingson, E., Carlberg, R., 1996, ApJS, 102, 269

X-RAY AND RADIO OBSERVATIONS OF INTERACTIONS IN COOLING CORE CLUSTERS

Tracy E. Clarke[1,2], Craig Sarazin[3], Elizabeth Blanton[4], and Namir Kassim[1]

[1]NRL, 4555 Overlook Drive SW, Washington, DC, 20375 USA
[2]Interferometrics Inc., 13454 Sunrise Valley Dr., Suite 240, Herndon, VA, 20171 USA
[3]Department of Astronomy, University of Virginia, P. O. Box 3818, Charlottesville, VA 22903-0818
[4]Astronomy Department, Boston University, 725 Commonwealth Ave., Boston, MA 02215, USA

ABSTRACT

We present a study of the radio and X-ray interactions in the cores of two dense cooling flow clusters. Our recent low frequency radio observations of these systems reveal low energy relativistic plasma which appears to connect the central radio source to the outer ghost cavities seen in Chandra images. We present details of the radio and X-ray observations of Abell 2597 which reveal several outburst episodes of the central AGN and provide the first suggestion of an X-ray tunnel which may be maintained over multiple outburst episodes. New radio observations of Abell 4059 reveal complex source morphology extending into the southeast ghost bubble. This synchrotron emission was not detected in previous higher frequency observations.

Key words: Galaxies: Cooling Flows, galaxies: clusters: individual (A2597, A4059); Radio Continuum: Galaxies.

1. INTRODUCTION

X-ray observations of the central regions of cooling core clusters such as Perseus (Böhringer et al. 1993; Fabian et al. 2000), Hydra A (McNamara et al. 2000), and Abell 2052 (Blanton et al. 2001) have revealed a wealth of detail in the thermal gas. One of the most spectacular results is the profound effect that the central radio sources in these systems have on the structure of the thermal gas. In most cases the active radio sources appear to expand subsonically or mildly transonically into the ICM and slowly displace the thermal gas (Fabian et al. 2000; McNamara et al. 2000). In a few clusters X-ray data reveal depressions or "ghost cavities" which are located well beyond the currently active radio galaxy. These cavities may delineate the location of old radio lobes which have detached and buoyantly risen in the cluster potential (Reynolds et al. 2005). The presence of numerous structures in cluster cores suggests that the central AGN may play a significant role in offsetting cooling in cores.

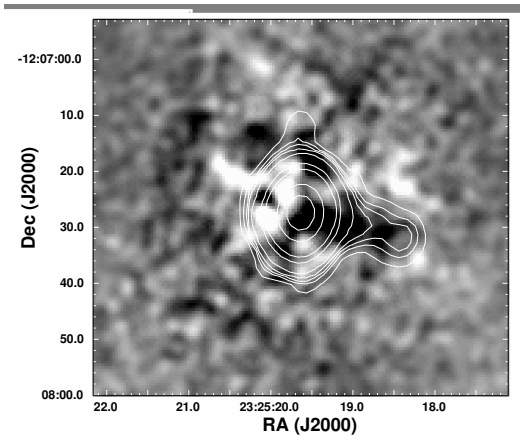

Figure 1. Greyscale shows X-ray residual image of $Chandra$ data for Abell 2597 obtained after subtracting a smooth elliptical model fit from the data. The residuals show significant structure and appear to reveal a tunnel connecting the AGN to the outer western ghost hole. Overlaid are the 330 MHz radio contours showing a low frequency extension running from the compact central galaxy to western hole.

2. ABELL 2597

Abell 2597 is a nearby cluster which contains a compact central radio galaxy (Sarazin et al. 1995) as well as optical and UV emission line filaments. The $Chandra$ X-ray observations of the system by McNamara et al. (2001) revealed the presence of X-ray depressions to the west and northeast located well beyond the active central radio galaxy. We investigated the cluster core structure in more detail by subtracting a smooth elliptical model fit to the $Chandra$ data (Clarke et al. 2005). In our residual map, the cavity to the west appears to be part of an X-ray tunnel running from the central AGN to the western cavity described by McNamara et al. We also see some evidence for a possible inner bubble located to the northeast.

We have analyzed archival VLA 1.4 GHz radio data of the central source and find a radio extension the fills the inner northeastern cavity. Further, a comparison of the 1.4 GHz radio data with the Ly_α filaments from O'Dea et al. (2004) shows that one of the filaments traces the outer edge of the radio extension. This 1.4 GHz data also shows some evidence (at a very low level) of emission extending along the X-ray cavity.

To further study this system we have undertaken new low frequency observations of the central radio galaxy using the 330 MHz system on the VLA. Although we do not resolve the compact central radio source, we find that there is a clear radio extension from the inner source extending to the west giving a total source size of $\sim$ 68 kpc (compared to 8 kpc for the compact source). In Figure 1 we show an overlay of the 330 MHz contours on the $Chandra$ residual image showing that the radio emission is co-incident with the X-ray tunnel.

Using the observed separation between the inner radio source and edge of the 330 MHz extension we expect a buoyancy rise time of $\tau_{buoy} \sim 2 \times 10^8$ yr if the emission represents a detached buoyant lobe from a past outburst of radio activity. The current radio data do not have sufficient resolution to determine whether the radio extension is connected to the central radio source, or whether it represents a detached buoyant radio lobe.

3. ABELL 4059

ROSAT HRI images of the thermal gas in Abell 4059 by Huang & Sarazin (1998) revealed the presence of X-ray cavities roughly aligned with the central radio source. More recently, the analysis of the $Chandra$ images by Heniz et al. (2002) has revealed complex structure in the cluster core which appears to be the result of significant interactions between the ICM and the radio galaxy. Although they find a clear correspondence between the northwest cavity and the 8 GHz radio lobe, there is no evidence of radio emission toward the southeast cavity. Lower frequency radio observations at 1.4 GHz by Choi et al. (2004) also failed to find emission extending into the southeastern cavity leading to the suggestion that the cavity is a ghost cavity from a previous radio outburst.

We have continued our low frequency observations of cooling cores by taking deep 330 MHz observations of Abell 4059. We show these radio contours overlaid on the $Chandra$ X-ray emission in Figure 2 (Clarke et al., in prep.). At low frequencies, the radio source reveals significant extended emission filling the ghost cavity to the east of the southern 1.4 GHz radio lobe.

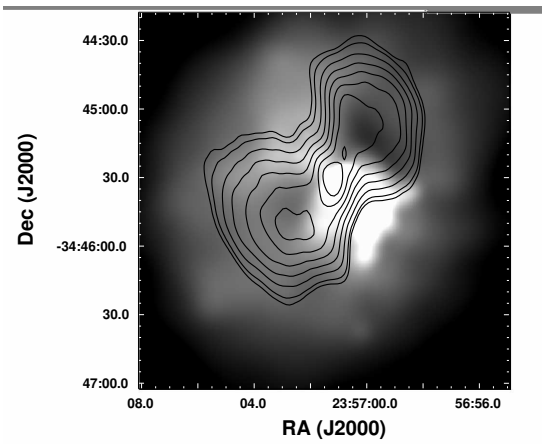

Figure 2. The adaptively smoothed $Chandra$ X-ray image of Abell 4059 is shown in greyscale with the VLA 330 MHz radio contours overlaid. The low frequency radio emission extends well beyond the higher frequency emission seen by Choi et al. (2004) and Heinz et al. (2002) and appears to fill both ghost cavities.

ACKNOWLEDGMENTS

The National Radio Astronomy Observatory is a facility of the National Science Foundation operated under a cooperative agreement by Associated Universities, Inc. Basic research in radio astronomy at NRL is supported by the office of Naval Research.

REFERENCES

Blanton, E. L., Sarazin, C. L., McNamara, B. R., & Wise, M. W. 2001, ApJ, 558, L15

Böhringer, H., Voges, W., Fabian, A. C., Edge, A. C., & Neumann, D. M. 1993, MNRAS, 264, L25

Choi, Y.-Y., Reynolds, C. S., Heinz, S., Rosenberg, J. L., Perlman, E. S., & Yang, J. 2004, ApJ, 606, 185

Clarke, T. E., Sarazin, C. L., Blanton, E. L., Neumann, D. M., & Kassim, N. E. 2005, ApJ, 625, 748

Fabian, A. C., et al. 2000, MNRAS, 318, L65

Heinz, S., Choi, Y.-Y., Reynolds, C. S., & Begelman, M. C. 2002, ApJ, 569, L79

Huang, Z., & Sarazin, C. L. 1998, ApJ, 496, 728

McNamara, B. R., et al. 2000, ApJ, 534, L135

McNamara, B. R. et al. 2001, ApJ, 562, L149

O'Dea, C. P., Baum, S. A., Mack, J., Koekemoer, A. M., & Laor, A. 2004, ApJ, 612, 131

Reynolds, C. S., McKernan, B., Fabian, A. C., Stone, J. M., & Vernaleo, J. C. 2005, MNRAS, 357, 242

Sarazin, C. L., Burns, J. O., Roettiger, K., & McNamara, B. R. 1995, ApJ, 447, 559

GAS DISTRIBUTIONS IN AN UNBIASED SAMPLE OF LOW-Z GALAXY CLUSTERS

J.H. Croston[1], M. Arnaud[1], G.W. Pratt[2], and H. Böhringer[2]

[1]Service d'Astrophysique, CEA Saclay, Orme des Merisiers, Bat 709, Gif-sur-Yvette Cedex, 91191, France
[2]MPE, Giessenbachstrasse, 85748 Garching, Germany

ABSTRACT

We present an improved technique for the deprojection and PSF-deconvolution of X-ray surface brightness profiles of galaxy clusters. Our method is tested using simulated profiles, *XMM-Newton* and *Chandra* data, and is shown to result in unbiased gas density profiles that retain full information about the gas distribution. We then apply the method to surface brightness profiles of an unbiased sample of nearby clusters from the XMM Legacy Project for the Study of Galaxy Cluster Structure, and discuss the scaling properties of the gas density profiles.

1. AN IMPROVED TECHIQUE FOR MEASURING GAS DENSITY PROFILES

We have developed a regularisation procedure for the direct deprojection and PSF-deconvolution of X-ray surface brightness profiles. Our technique allows us to obtain accurate gas density profiles in a straightforward manner from X-ray observations, avoiding *a priori* assumptions about the functional form of the density distribution and making full use of the information in the surface brightness profile, unlike the use of analytical models. Our regularisation procedure is adapted from the Philips-Towmey method used by Bouchet (1995) for the deconvolution of gamma-ray spectra. The effects of projection and PSF blurring can be expressed as a 2D redistribution matrix, determined from geometrical calculations and detector characteristics, which is multiplied by the emitted profile to produce an observed surface brightness profile. Since directly solving this equation for the emitted profile is an inverse problem, we minimise the amplification of errors in the derived emitted profile by constraining the solution to be smooth (minimising the sum of the squares of the 2nd derivatives about each point), using a cross-validation technique to systematically choose a regularisation coefficient based on distinguishing between smooth (i.e. physically plausible) variations and noise (e.g. Wahba 1978).

In Fig 1 we show the results of Monte Carlo simulations of profiles obtained by projection and PSF convolution of the simulated emission from model density distributions. We used the AB model of Pratt & Arnaud (2002), a modified β-model that can also fit central cusps:

$$n_e = A \left(\frac{r}{r_c}\right)^{-\alpha} \left[1 + \left(\frac{r}{r_c}\right)^2\right]^{-3\frac{\beta}{2}+\frac{\alpha}{2}} \quad (1)$$

We varied the parameters to generate input profiles, which were each projected, then used to generate 100 simulated *XMM* profiles per model using Poisson statistics. These were convolved with an *XMM* response matrix. For each model, we then compared the mean output density profiles from our code with the input profiles. In all cases the input profile is recovered to a high degree of accuracy with no bias. More details and rigorous testing of our method are presented in Croston et al. (in prep).

We applied our deprojection code to three clusters for which both XMM and Chandra data exist: Abell 478, Abell 1413 and Abell 1991. We found very good agreement between our results and the deprojected Chandra profile of Sun et al (2003) for A478, and best-fitting analytical model of Vikhlinin et al. (2005) for A1413 (Figure 2). In the case of Abell 1991 (not shown), the shape of the XMM profiles (both deprojected and best-fit model)

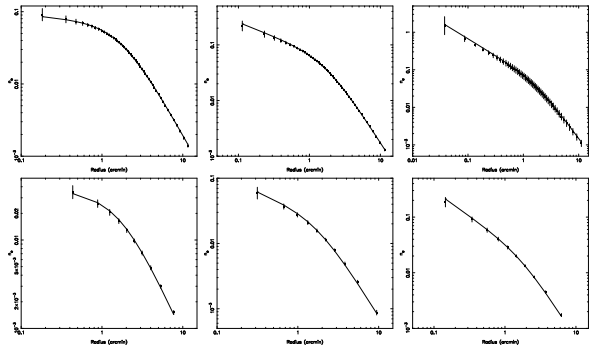

Figure 1. Simulation input density profiles (solid line) and output profiles (filled squares). L to r: AB models with $\beta = 0.67$ $r_c = 0.1R_{200}$, and $\alpha = 0.1$, 0.5 and 0.9. Top: high quality data, bottom: poor quality data.

was found to differ at about the 10% level from the best-fitting Chandra model (Vikhlinin et al. 2005) in the inner regions, but the profiles are consistent at large radii.

2. THE *XMM-NEWTON* LEGACY PROJECT FOR GALAXY CLUSTER STRUCTURE

A large, unbiased sample of clusters has been observed with XMM-Newton in order to allow a systematic investigation of: the scaling relations of observable cluster properties, such as X-ray luminosity, temperature, characteristic radius and cluster mass, and the source of scatter in these relations, e.g. non-thermal heating processes, merger activity; dynamical states of the clusters, the statistics of cluster mergers and the frequency of cooling cores as a function of cluster mass (important cosmological diagnostics); entropy profiles as a probe of thermal and star fomation history, metal abundances as a function of various observational parameters, and the variation of cluster mass and mass-to-light profiles. The REFLEX catalogue (Böhringer et al. 2004) was used to construct a sample based on the following criteria: $z < 0.2$; X-ray-luminosity-selected, to be unbiased to cluster type; close to homogeneous coverage of luminosity space; $T > 2$ keV; distances selected to optimally use photon collection power and field-of-view of XMM; and detectable with XMM to at least a radius of r_{500}. XMM-Newton has now carried out observations for the entire sample of 34 clusters. The results presented here are based on analysis of a subsample of 15 clusters, consisting of those for which the data were not significantly affected by high background periods.

X-ray surface brightness profiles were extracted for the subsample of 15 clusters, using standard techniques and double background subtraction. Profiles from the MOS1, MOS2 and pn cameras were summed. Density profiles were then obtained using the technique described in Section 1. Global temperatures (emission-weighted averages, excluding cooling regions) were used to calculate R_{200} using the relation of Arnaud et al. (2005); the densities were then scaled according to their expected

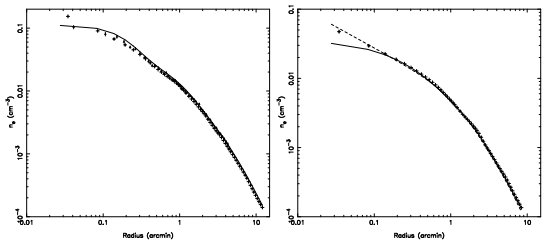

Figure 2. Comparison of XMM and Chandra profiles for Abell 478 (left) and Abell 1413 (right), with the XMM profile obtained with our method (+ symbols), the best-fitting XMM models of Pointecouteau et al. (2004) and Pratt & Arnaud (2002) (solid lines), respectively, and the Chandra profiles of Sun et al. (2003) (filles triangles) and Vikhlinin et al. (2005) (dashed line), respectively.

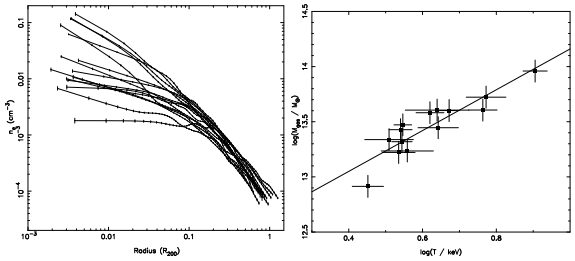

Figure 3. Left: The scaled gas density profiles for the cluster sample. Right: Total gas mass vs. global temperature.

evolution as a function of redshift. In Fig 3 (left) the scaled density profiles are shown for the entire subsample. We found a large scatter in the density profiles at large radii (σ_{ne}/n_e = 0.28 at $0.3R_{200}$). We tested whether this could be explained by a temperature-dependence of the density; however, rescaling the density profiles by $T^{0.525}$ (not plotted), the relation expected as a result of the departure from self-similarity in the $S - T$ relation (e.g. Ponman et al. 2003) does not reduce the scatter in n_e at $0.3R_{200}$. The mean slope for $R > 0.2R_{200}$ is $\alpha = 1.87 \pm 0.24$ ($\beta = 0.62$, consistent with the mean value of β for the sample of Vikhlinin et al. 2005). We find possible evidence of a relation between slope and global temperature; however, the temperature range is not sampled very well for our subsample, and so the full sample will be necessary to confirm this. We next investigated the scaling of the total gas mass with temperature (Fig 3, right), measuring the mass to a scaled radius of $0.7R_{200}$, and found a reasonably tight correlation, with a slope of 1.8 ± 0.3, consistent with the observed relation for total cluster mass (e.g. Arnaud et al. 2005). An investigation into the influence of cluster dynamical state on the gas density scaling properties is ongoing.

REFERENCES

Arnaud M., Pointecouteau E. & Pratt G.W. 2005 A&A, 441, 893

Böhringer H., Schuecker P., Guzzo L., et al. 2004, A&A, 425, 367

Bouchet L. 1995, A&AS, 113, 167

Ponman T.J., Sanderson A.J.R. & Finoguenov A. 2003, MNRAS, 343, 331

Pointecouteau E., Arnaud M., Kaastra J., de Plaa J. 2004, A&A, 423, 33

Pratt G.W. & Arnaud M. 2002, A&A, 394, 375

Sun M., Jones C., Murray S.S., et al. 2003, ApJ, 587, 619

Vikhlinin A., Kravstov A., Forman W., et al. 2005, ApJ submitted, astro-ph/0507092

Wahba G. 1978, J. Royal Stat. Soc., B3, 364

METAL ENRICHMENT DISCRIMINATORS OF COLD FRONTS

R. Dupke

Dept. Astronomy, University of Michigan, Ann Arbor 48109

ABSRACT

Cold fronts are sharp surface brightness discontinuities characterized by a jump in gas temperature accompanied by a decline in X-ray surface brightness such that the gas pressure remains continuous across the front and, thus, these structures differ from bow shocks. Models suggest that cold fronts can be generated by external mechanisms involving the accretion of a subsystem with a remnant "cold core". However, internal mechanisms can also create cold fronts, such as gravitational scattering of subclumps or cD oscillation around the bottom of the potential well. These competing models for their formation can be discriminated through the measurements of the SN Type contamination across the front, which in turn can be determined from metal abundance ratios as measured from an ensemble of elements. Here we present the preliminary results of such analysis using a sample of clusters observed with Chandra.

1. INTRODUCTION & METHODS

Cold fronts have been originally interpreted as subsonic motion of accreted substructures (Markevitch et al. 2002). Although this explanation holds relatively well for clusters that have clear signs of merging, such as A3667 (Mazzotta et al. 2001) there are other alternative explanations that involve internal mechanisms. For example, cD oscillation in the bottom of the potential well or induced oscillation of the potential well itself, e.g. A496 (Dupke & White 2003), A1795 (Fabian et al. 2001; cf. Markevitch et al. 2001). Both types of models are justified theoretically (e.g. Bialek, Evrard and Mohr 2002, Lufkin et al. 1995, Tittley & Henriksen 2005). The global enrichment history of clusters and groups is different (Finoguenov & Ponman 1999) and the internal distribution of metal enrichment is not flat in clusters (e.g. Dupke & White 2000; Allen et al. 2001); Typically, clusters have a higher SN Ia Fe mass contamination near the core than in the outer parts. This fact provides a way to test for competing cold front scenarios by looking at gradients in abundance ratios measured across the front.

If the mechanism is external, such as a sub-clump accretion, one should find an enrichment discontinuity across the front. If no discontinuity is found models based on internal mechanisms are favored. Dupke & White (2003) used this method with Abell 496 and found no evidence of a chemical discontinuity across the front within the errors. We here extend their analysis to a larger sample of "cold front" clusters to determine the frequency and overall properties of different mechanisms that generate cold fronts. The data presented here were reduced with **Ciao** 3.2.0 with **CALDB** 3.0 using the standard procedure and blank-sky background. Here we show the results of spectral fittings with **XSPEC** V11.3.1 using an absorbed **VAPEC** thermal emission model. The maps shown below are colored contour maps. The color steps were chosen in a way as to approximate the 1σ errors. Below, for illustration, we show the projected distribution of entropy $T/n^{2/3}$ (K cm^2)), which is a good tracer of cold fronts (marked with white arrows) and Si/Fe for A496 and A4059 and compare them to the merging cluster A576, for which there are strong indications of a strong line of sight merger with a NW-SE inclination of ~9º (Dupke, Mirabal and Bregman 2006).

2. RESULTS

In the "remnant scenario" model for cold fronts, the expected distribution of abundance ratios should be similar to what is observed for the merging cluster A576 (last row), where a clear Si/Fe discontinuity is seen at the cluster core. The results of a deeper observation of A496 do not indicate any obvious chemical gradient using 4 well define abundance ratios including Si, S, O and Fe in any of its 3 confirmed cold fronts. Furthermore, similar analysis performed in 3 other clusters with cold fronts (2A0335, A2052, A4059) show similar results. The results are in agreement with models that use internal mechanisms to form cold fronts. Despite the presence of chemical gradients near the core of some clusters (e.g. A4059 below), the distribution of abundance ratios do not show any systematic connection to the surface discontinuities as it should be expected and is yet to be detected, in the "remnant core" scenario. Therefore, association of cold fronts to ICM bulk motions may not be justified for a significant fraction of clusters.

A496 - Entropy - 3kcnt/cell

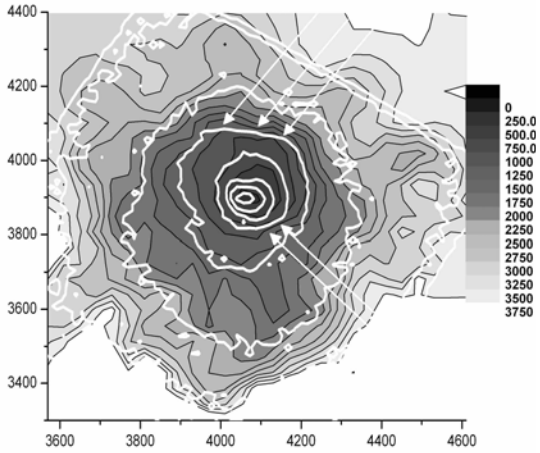

A496 - Si/Fe ratio - 7kcnt/cell

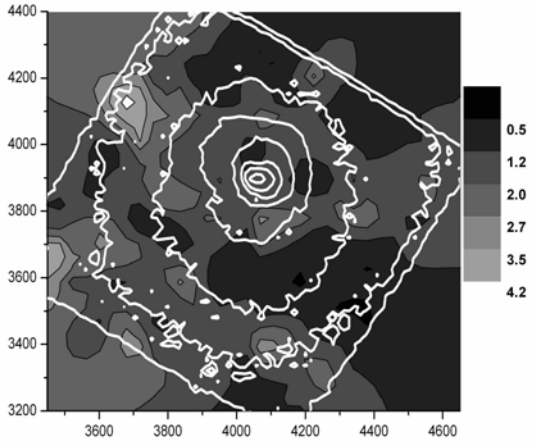

A4059 - Entropy - 3kcnt/cell

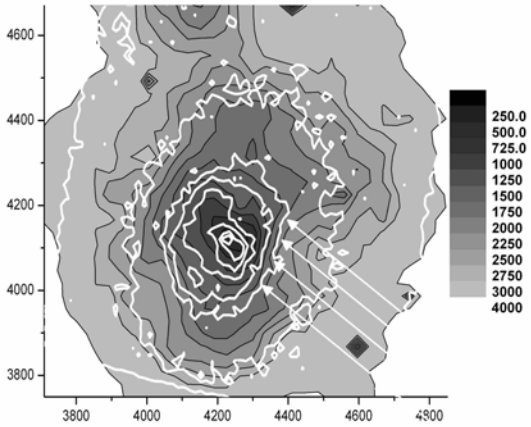

A4059 - Si/Fe - 15kcnt/cell

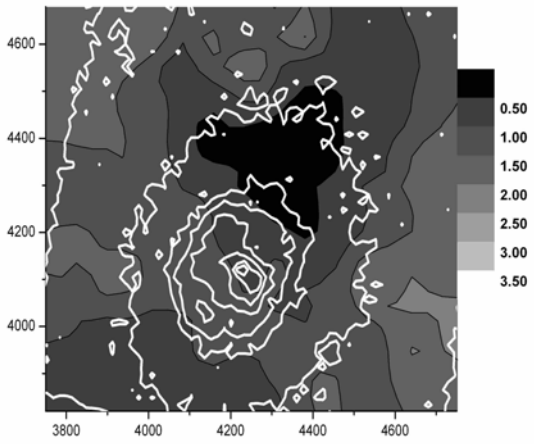

A576 - Entropy - 5kcnt/cell

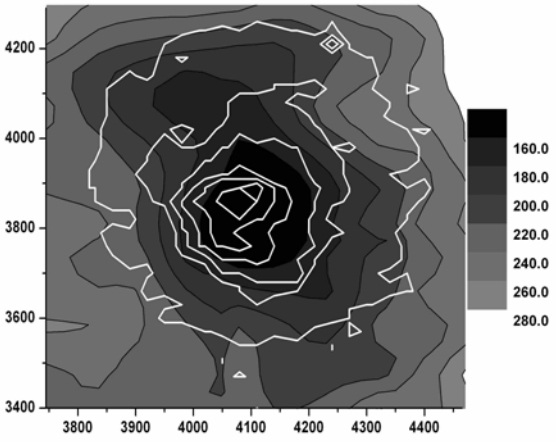

A576 - Si/Fe ratio - 5kcnt/cell

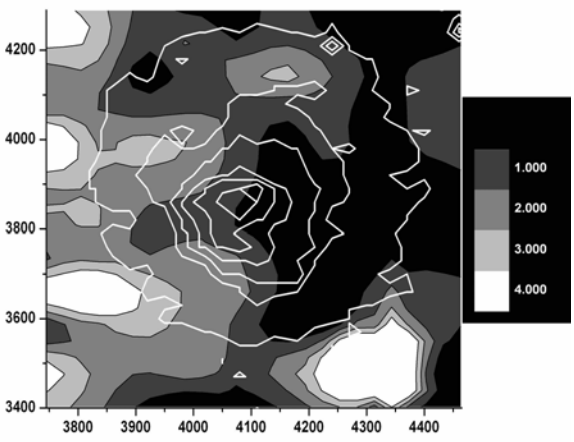

AN XMM-NEWTON VIEW ON RELAXED AND NON-RELAXED CLUSTERS OF GALAXIES

F. Durret[1], G.B. Lima Neto[2], J. Bagchi[3], C. Adami[4], H. Bravo-Alfaro[5], G. Covone[6], and J. van Gorkom[7]

[1]IAP, 98bis Bd Arago, 75014 Paris, France
[2]IAG/USP, São Paulo, Brazil
[3]IUCAA, Pune, India
[4]LAM, Marseille, France
[5]Univ. Guanajuato, Mexico
[6]INAF, Oss. Capodimonte, Naples, Italy
[7]Columbia Univ., New York NY, USA

ABSTRACT

XMM-Newton observations have allowed to draw temperature maps for the X-ray emitting gas in clusters of galaxies, showing evidence for violent mechanisms rather than peacefully relaxed structures. We present temperature maps for four very different clusters and show how their interpretation gives insight on the merging history of these clusters.

Key words: X-rays; clusters of galaxies.

1. INTRODUCTION

In the standard ΛCDM cosmological picture the latest objects to collapse are $\sim 10^{14} - 10^{15} M_{\odot}$ dark halos, corresponding to rich clusters of galaxies. These objects present signs of recent dynamical activity, implying a recent past of merger events. XMM-Newton now allows to draw intra-cluster gas temperature maps and to obtain informations on the cluster formation and evolution histories.

2. RESULTS: FROM CLUSTERS STILL FORMING TO RELAXED CLUSTERS

The XMM-Newton temperature maps were computed for the four clusters described here following the method fully described by Durret et al. (2005). These maps are displayed in Fig. 1.

Abell 2667 (z=0.233) is a rich, massive cluster, with bright gravitational arcs and optical intra-cluster diffuse light (Covone et al. 2005) aligned along a north-east to south-west direction. The general shape of the X-ray emission is aligned along the same direction, and the X-ray temperature map shows hotter regions than average south west and north east of the centre, that is along the cluster main axis, along which one or two sources of diffuse light are also detected. This suggests that the gas could have been shock heated in a past merging during which the diffuse light may have been created by stars stripped from galaxies by ram pressure.

Abell 85 (z=0.0555) consists of a main structure, a south-blob and a filament made of groups falling towards the main cluster (Durret et al. 2003, 2005). The XMM temperature map shows a hotter region between the south blob and the centre of Abell 85 corresponding to the heating of the ICM by the shock of the infalling groups from the filament. Several hot spots seen in the west half of the cluster strikingly resemble the temperature map derived from numerical simulations by Bourdin et al. (2004), strongly suggesting that a sub-cluster merged with Abell 85 a few Gyrs ago coming from the west. This is consistent with recent VLA observations showing that HI is detected in galaxies located in the east half of the cluster but not in the west half, therefore suggesting that their HI content has been stripped by a merger coming from the west (Bravo-Alfaro et al. in preparation).

Abell 3376 (z=0.0456) is probably the result of an ongoing merger. Its X-ray emission has a "bullet" structure, pointing towards the north-east, remindful of the "bullet cluster" observed by Markevitch et al. (2002, also see these proceedings). The XMM temperature map, shows a succession of cold and hot arcs suggesting the passing of shock waves, as in the simulations by Takizawa (2005).

Abell 496 (z=0.033) appears to be a very relaxed cluster from its X-ray emission map. However, its X-ray temperature map shows small signs of substructure, with somewhat cooler gas seen near the centre to the South and a possible "bubble" of hotter gas just south of the center (also see Dupke et al., these proceedings).

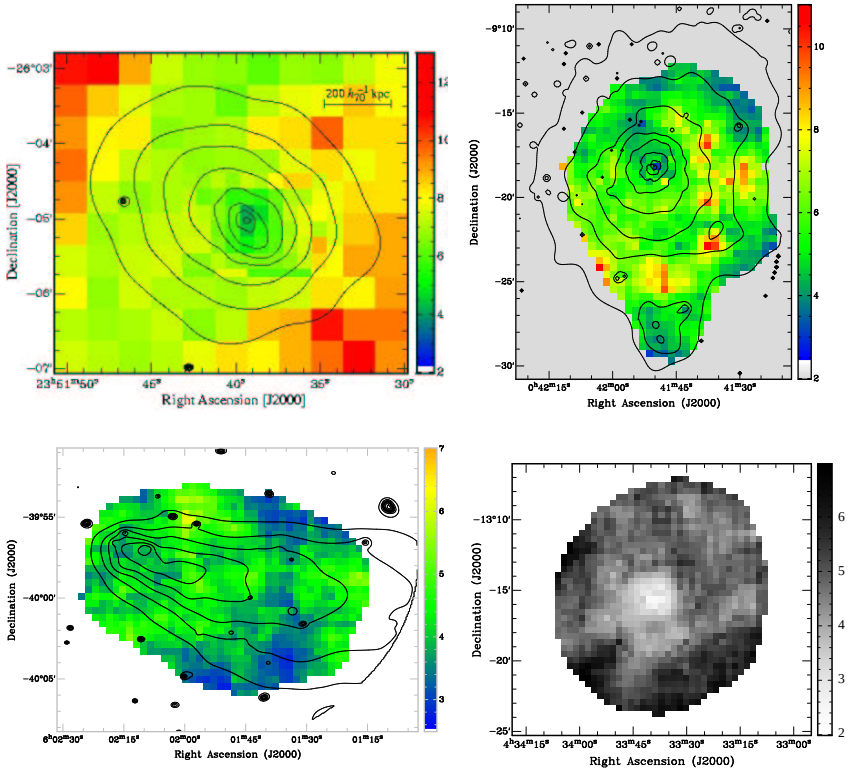

Figure 1. XMM-Newton temperature maps for the clusters of galaxies Abell 2667 (top left), Abell 85 (top right), Abell 3376 (bottom left) and Abell 496 (bottom right).

3. CONCLUSIONS

Thanks to the unprecedented sensitivity of XMM-Newton, detailed intra-cluster gas temperature maps can now be obtained, giving crucial informations on the formation and evolution histories of clusters. They allow in particular to trace the merging histories of clusters. Obviously, not two clusters are alike, an therefore an individual analysis of their properties is required before any statistical study can be made. Besides, even clusters with apparently smooth X-ray emission can show complicated temperature maps, implying that the number of really relaxed clusters is notably smaller than previously believed. One must therefore be careful when estimating, for example, total cluster masses, or when deriving cosmological parameters from a sample of clusters. The results described above also illustrate the fact that multi-wavelength observations are obviously necessary to analyze such complex objects. The complexity of nearby clusters is not unexpected of course, since it agrees with the generally accepted paradigm of hierarchical formation of structures.

ACKNOWLEDGMENTS

F.D. and G.B.L.N. acknowledge financial support from the CAPES/COFECUB. G.B.L.N. is grateful to FAPESP/Brazil and F.D. to CNES/France for financial support.

REFERENCES

[] Bourdin, H., Sauvageot, J.-L., Slezak, E., et al., 2004, A&A 414, 429

[1] Covone, G., Adami, C., Durret, F., et al., 2005, A&A submitted

[2] Durret, F., Lima Neto, G.B., Forman, W., & Churazov, E. 2003, A&A 403, L29

[3] Durret F., Lima Neto G.B., & Forman W. 2005, A&A 432, 809

[4] Markevitch M., Gonzalez A. H., David L. et al. 2002, ApJ 567, L27

[5] Takizawa, M. 2005, ApJ, 629, 791

TEMPERATURE AND DARK MATTER PROFILES OF GALAXY GROUPS

F. Gastaldello[1], D. Buote[1], P. Humphrey[1], L. Zappacosta[1], J. Bullock[1], F. Brighenti[2,3], and W. Mathews[2]

[1]Department of Physics and Astronomy, University of California Irvine
[2]UCO/Lick Observatory, Board of Studies in Astronomy and Astrophysics, University of California Santa Cruz
[3]Dipartimento di Astronomia, Università di Bologna

ABSTRACT

The *Chandra* and *XMM* data for a sample of 19 relaxed groups/poor clusters, covering the temperature range 1-3 keV and selected to have the best available data, reveal a remarkable similarity in their temperature profile: cool cores outside of which the temperatures reach a peak for radii less than 0.1 $r_{\rm vir}$ and then decline.
We fitted the derived mass profiles using an NFW model, which provides a good fit to the data when accounting for the central galaxy in the inner region. The concentration parameters and virial masses are in the range $c_{\rm vir}$= 5-22 and $M_{\rm vir}$= $2 \times 10^{13} - 4 \times 10^{14}$ $M_{\odot}$, in general agreement with the concentrations found in numerical simulations.

Key words: X-rays: galaxies: clusters; galaxies: halos; dark matter.

1. INTRODUCTION

The nature of Dark Matter (DM) in the universe is one of the fundamental problems in astrophysics and cosmology. Crucial is the comparison of observation with N-body simulations in the currently favored ΛCDM cosmology, which predicts a universal NFW profile for DM halos (Navarro et al., 1997). This prediction has been tested for the scale of hot, massive clusters (Pointecouteau et al., 2005; Vikhlinin et al., 2005) but few constraints exist on the group scale, where predictions for the statistical properties of DM halos are more accurate because a large number of objects can be simulated at once (e.g. Bullock et al., 2001). The distribution of concentration parameters (c) is expected to vary significantly as a function of the cosmological parameters (e.g. Kuhlen et al., 2005). A measure of the mean and scatter of c at the group scale is a crucial test of the ΛCDM model.

The inner halo profiles also reveal vital information about the interplay between the DM and baryons during group formation. It is expected that in the central region of group halos the pure NFW profile will be modified by adiabatic compression as a response to baryonic dissipation (Blumenthal et al., 1986). This raises the question whether the DM profile at the center of groups should be represented by a pure or modified (adiabatically compressed, AC) NFW profile. DM properties can strongly constrain the galaxy formation process.

2. DATA ANALYSIS

2.1. Sample selection

The sample has been selected to cover the range in the temperature from 1 to 3 keV, the temperatures expected for groups/poor clusters, with as much as possible regular X-ray morphology and with a dominant elliptical galaxy at the center (the only exception being RGH80, with two ellipticals of comparable size at the center), to ensure dynamical relaxation.

2.2. Background subtraction

A correct background subtraction is a critical element of our analysis. We describe here the procedure adopted for XMM. Soft proton flares cleaning have been performed on a region free of the luminous core of the objects and point sources and using both a hard and 0.5-10 keV light curve. The background has been then entirely modeled with a procedure similar to Lumb et al. (2002). This method is particularly effective in studying groups because the source component (mainly characterized by the Fe-L blend) is clearly spectrally separated from all the other background components. The model has been applied to a simultaneous fit of source+background in the outer annuli to correctly determine the normalizations of the various background components.

2.3. From temperature and density profiles to mass profiles

Spectra were extracted in concentric circular annuli located at the X-ray centroid and fitted with an APEC modified by Galactic absorption. We projected parameterized 3D models for gas density and temperature to fit the results obtained from our spectral analysis (the projected gas mass density is derived from the APEC normalization). Using the best fit parameterized function we derive the total gravitating mass under the assumption of spherical symmetry and hydrostatic equilibrium. The virial quantities quoted in the poster are for an over-density of ≈ 101 appropriate for the ΛCDM model.

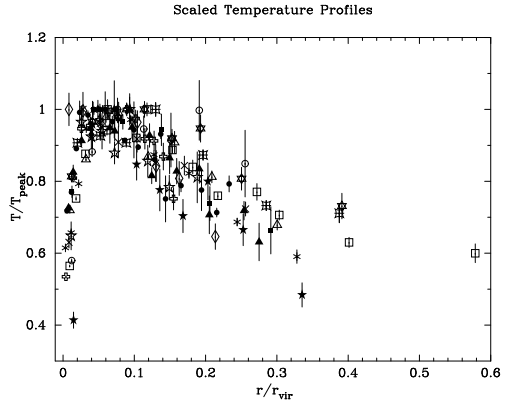

Figure 1. XMM temperature profiles for the sample normalized by the peak in the temperatures profile for each cluster and scaled by the virial radius obtained by the NFW fit. AWM 4 is shown with open diamonds.

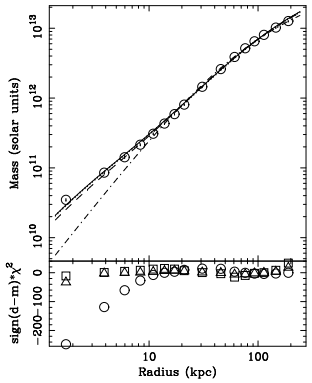

Figure 2. DM+stellar mass fitted by a pure NFW (dot-dashed, residuals with open circles), an NFW+Hernquist profile (dashed, triangles), an AC NFW model (solid, squares).

3. TEMPERATURE PROFILES

The temperature profiles for the systems, scaled by the virial radius obtained in the NFW fit, show a remarkable similarity. The shape resembles the one obtained for hotter, more massive clusters (e.g. Vikhlinin et al., 2005) but with the peak of the temperature profile occurring at smaller radii (see Fig.1). The central cooling region is smaller and can be extremely affected by non-gravitational processes like radiative cooling and AGN heating (as it is probably the case for AWM 7 which has an interesting isothermal central profile, O'Sullivan et al., 2005).

4. A CASE STUDY: NGC 1550

As an example of the procedure adopted for each object in the sample we show here the case of NGC 1550. We analyzed the two ACIS-I and XMM observations and fitted jointly the temperature and density profiles. The derived gravitating mass profile has been fitted by an NFW profile. The DM+stars profile (obtained by subtracting the gas mass from the gravitating mass) has been fitted by a pure NFW, an NFW + stellar component for the central galaxy, with the latter modeled by an Hernquist profile (Hernquist, 1990) or an AC model (Gnedin et al., 2004),

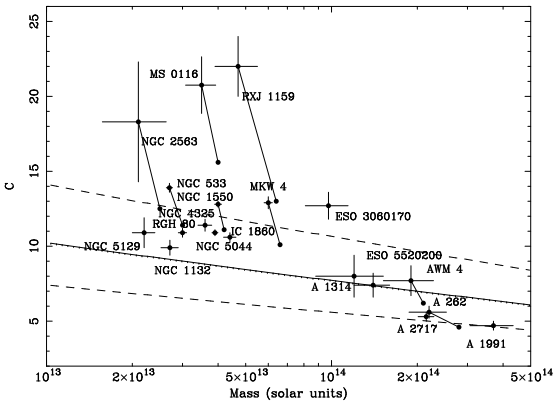

Figure 3. Concentration parameters as a function of mass. The solid line shows the mean c(M) and outer lines the 1σ scatter from numerical simulations (Bullock et al., 2001). The lines connect to the end point (shown without error bars) in the plot for objects requiring the introduction of a stellar component.

as shown in Fig.2.

5. VARIATION OF CONCENTRATION WITH MASS

The resulting relation between c and group mass is shown in Fig.3. An NFW profile is a good representation of the mass profiles observed; for 8 objects an excess compared to the NFW fit is present in the inner regions (as in NGC 1550): when fitted with an NFW+Hernquist or AC model, with the stellar mass free to vary, the returned stellar M/L_B for the central galaxy are in the range 2-7. We can not discriminate between these two latter models. The inferred M/L are considerably lower than the ones measured using stellar kinematics (e.g. Gerhard et al., 2001). The inclusion of the stellar component in these objects has the effect of lowering c and increasing the mass. The typical values and scatter of concentrations are in general agreement with the simulation results, as shown in Fig.3. Even after the inclusion of adiabatic contraction the results tend to be higher than predicted: a possible explanation is that we are looking at a biased population of groups (relaxed, with some objects in our sample being classified as fossil groups, which should show an higher c being formed at earlier epochs, Zentner et al., 2005).

ACKNOWLEDGMENTS

We thank O. Gnedin for kindly providing his AC code.

REFERENCES

Blumenthal, G.R. et al. 1986, ApJ, 301, 27
Bullock, J. et al. 2001, MNRAS, 321, 559
Gerhard, O. et al. 2001, ApJ, 121, 1936
Gnedin, O. Y. 2004, ApJ, 616, 16
Hernquist, L. 1990, ApJ, 356, 339
Kuhlen, M. et al. 2005, MNRAS, 357, 387
Lumb, D. et al. 2002, A&A, 389, 93
Navarro, J. et al. 1997, ApJ, 490, 493
O'Sullivan, E. et al. 2005, MNRAS, 357, 1134
Pointecouteau, E. et al. 2005, A&A, 435, 1
Vikhlinin, A. et al. 2005, astro-ph 0507902
Zentner, A.R. et al. 2005, ApJ, 624, 505

ANALYSIS OF LOW SURFACE BRIGHTNESS X-RAY CLUSTERS OF GALAXIES

H. Katayama[1] **and K. Hayashida**[2]

[1]Japan Aerospace Exploration Agency (JAXA), 2-1-1 Sengen, Tsukuba, Ibaraki 305-8505, Japan
[2]Department of Earth and Space Science, Graduate School of Science, Osaka University, Machikaneyama 1-1, Toyonaka, Osaka 560-0043, Japan

ABSTRACT

We present the analysis of a sample of 7 low surface brightness (LSB) X-ray clusters (4C+34.16, A1674, A1882, A194, A2638, A2690, and NGC5171) observed with XMM-Newton. These clusters are nearby ($0.02 < z < 0.14$) but have a low X-ray flux which is less than 10^{-12} erg sec^{-1}cm^{-2}. The LSB clusters are considered to be a new class of objects which are in the process of formation. We investigate the X-ray properties of these clusters.

We find 3 of 7 clusters shows a low metal abundance of $<$0.2 solar. Our result indicates that in these clusters not enough metals are supplied from member galaxies. The low metal abundance and LSB suggest that these clusters are still at an early stage of evolution.

Key words: Galaxy clusters; Low surface brightness; XMM-Newton .

1. INTRODUCTION

The evolution of the metal abundances in the intracluster medium (ICM) is historically studied by many authors (e.g., Mushotzky & Loewenstein, 1997; Tozzi et al., 2003). These results suggest that there is no evolution of the mean iron abundance out to $z \sim 1$ and that most of the cluster metals were produced at $z > 1$. These studies have mainly been performed for the X-ray luminous galaxy clusters.

However, Katayama, Hayashida, and Nishino (2005) observed a low surface brightness (LSB) X-ray clusters A1674 and found that some properties of A1674 are different from those of X-ray luminous galaxy clusters. The metal abundance of A1674 ($0.07(< 0.2)\,Z_{\odot}$) is lower than that of other clusters. Katayama, Hayashida, and Nishino also showed that the gas fraction $f_{\rm gas}$ of A1674 is only 1%. The low metal abundance and the low gas fraction suggest that this cluster is still at an early stage of evolution.

In order to investigate X-ray properties of other LSB clusters, we analyzed a sample of LSB clusters observed with XMM-Newton. Throughout this paper, we assume a cosmology with $H_0 = 70\,\mathrm{km\ s^{-1}\ Mpc^{-1}}$, $\Omega_{\rm m} = 0.27$ and $\Lambda = 0.73$.

2. SAMPLE

We selected sample clusters from the XMM-Newton archival data. In order to select a LSB cluster, we used following selection criteria: (1) Cluster redshift is less than 0.2, (2) X-ray flux is less than 10^{-12} erg sec^{-1}cm^{-2}, and (3) Spatially averaged temperature is more than 1 keV. From about 400 archival data of clusters of galaxies, we selected 7 clusters including A1674.

3. SPECTRAL ANALYSIS

We screened the event files following the method in Katayama et al. (2004). In order to investigate the diffuse X-ray emissions of these clusters, we first detected point sources using the SAS task eboxdetect. We excluded a circular region of radius $15''$ around detected sources. We used the blank sky data compiled by Read & Ponman (2003) as a background data. Fig. 1 shows the EPIC spectra of NGC5171. We fitted these spectra with the APEC model modified by Galactic absorption. The neutral hydrogen column density is fixed to the Galactic values. Fig .2 shows the error contours for metal abundance versus cluster temperature.

Table 1 shows the best-fit parameters for the spectrum fit. Although we can constrain only the upper limit due to the poor photon statistics for some clusters, the fitting results suggest that the metal abundance of 3 clusters (A1674, A2638, and NGC5171) are $<$0.2 solar.

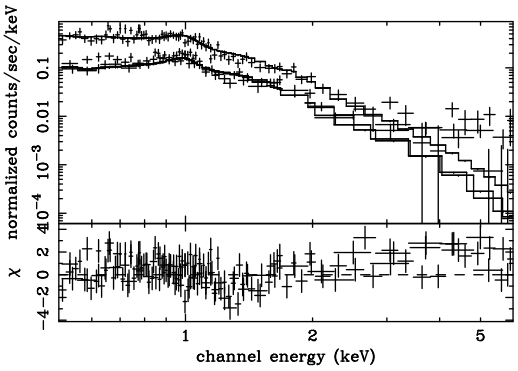

Figure 1. EPIC spectra of NGC5171.

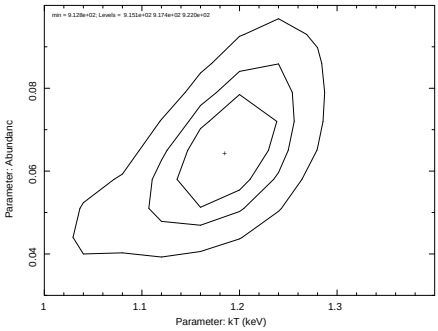

Figure 2. 68%, 90%, and 99% error contours for the cluster temperature and abundance of NGC5171.

4. COMPARISON WITH X-RAY BRIGHT CLUSTERS

Fig. 3 shows the temperature-iron abundance relation obtained from ASCA observation (Matsumoto et al., 2000). We find 3 of 7 clusters show a low metal abundance of $<$0.2 solar. Our result indicates that in these clusters not enough metals are supplied from member galaxies.

5. SUMMARY

We analyzed 7 LSB X-ray clusters. From the spectral analysis, we find that 3 of 7 clusters shows low metal abundance of $Z<0.2Z_{\odot}$. The low metal abundance and LSB suggest that these clusters are still at an early stage of evolution.

In order to investigate the LSB clusters, a low background detector is crucial. The X-ray CCD camera onboard Suzaku (X-ray Imaging Spectrometer: XIS) has an advantage that the background level is lower in comparison with Chandra or XMM-Newton Katayama et al. (2004). This advantage of Suzaku/XIS will reveal the detail of the early stage of cluster evolution.

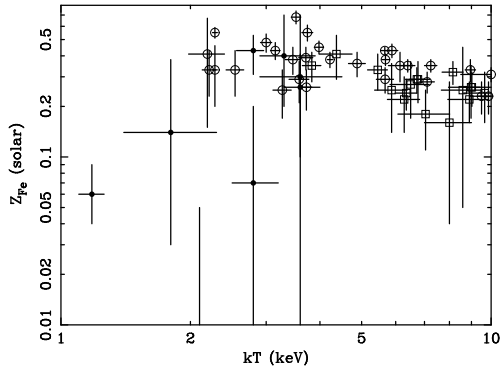

Figure 3. Comparison of temperature-iron abundance relation. Open circles and open squares are correspond to nearby cluster samples and distant cluster samples, respectively. Closed circles are 7 LSB clusters.

Table 1. Best-fit parameters of sample clusters.

Target	redshift	f_X [10^{-13} erg/s/cm^2]	kT [keV]	Z
4C+34.16	0.078	5.64$\pm$0.06	$3.3^{+0.6}_{-0.4}$	$0.4^{+0.3}_{-0.2}$
A1674	0.107	2.83$\pm$0.09	$2.8^{+0.4}_{-0.3}$	$0.07(<0.20)$
A1882	0.137	3.53$\pm$0.25	$3.6^{+0.9}_{-0.7}$	$0.3^{+0.4}_{-0.3}$
A194	0.018	7.74$\pm$0.35	$3.6^{+0.4}_{-0.3}$	$0.26^{+0.15}_{-0.16}$
A2638	0.083	1.44$\pm$0.03	$2.1^{+0.2}_{-0.2}$	$0.00(<0.05)$
A2690	0.013	0.69$\pm$0.09	$1.8^{+0.5}_{-0.4}$	$0.14^{+0.24}_{-0.11}$
NGC5171	0.023	1.40$\pm$0.05	$1.18^{+0.08}_{-0.08}$	$0.06^{+0.03}_{-0.02}$

REFERENCES

Katayama, H., Takahashi, I., Ikebe, Y., et al. 2004, A&A 414, 767

Katayama, H. Hayashida, K. and Nishino, Y. 2005, AdSpR, in press

Matsumoto, H., Tsuru, T. G., Fukazawa, Y., et al. 2000, PASJ 52, 153

Mushotzky, R. F. & Loewenstein, M. 1997, ApJ 481, L63

Read, A. M. & Ponman, T. J. 2003, A&A 409, 395

Tozzi, P., Rosati, P., Ettori, S., et al. 2003, ApJ 593, 705

DENSITY, TEMPERATURE AND DARK MATTER PROFILES IN CLUSTERS OF GALAXIES

Gastão B. Lima Neto[1], **Tatiana F. Laganá**[1], **and Florence Durret**[2]

[1]Instituto de Astronomia, Geofísica e Ciências Atmosféricas, USP, São Paulo/Brazil
[2]Institut d'Astrophysique de Paris, France

ABSTRACT

We have investigated the radial distribution of matter in a sample of rich clusters of galaxies by deprojecting the X-ray surface brightness and temperature profiles. We have used an analytical approach to solve the Abel inversion equation. With the deprojected observed profiles, we have computed the dark matter density profile. Cool core clusters presented cuspy dark matter profiles, similar to the profiles obtained in cosmological N-body simulations and strong lensing analysis.

Key words: X-rays; Cluster; Dark Matter.

1. INTRODUCTION

Theoretical analysis and N-body cosmological simulations of a cold dark matter dominated universe suggests that structure formation is hierarchical, smaller structures collapse first and larger structures are formed later by merging. The shape of the matter distribution profile in relaxed dark matter halos is steep, with a cuspy centre somewhere between $\rho \propto r^{-1}$ and $\rho \propto r^{-2}$. An important effort exists in order to obtain and understand the total mass, gas density and temperature, specific entropy, baryon fraction profiles (e.g., in the past 2 years, de Grandi & Molendi 2004; Vikhlinin et al. 2005; Piffaretti et al. 2005; Pointecouteau et al. 2005; Neumann 2005).

Here, we investigate the shape of the total mass density profile using the standard hydrostatic equilibrium hypothesis with simple analytical gas density and temperature profiles. This allows us to easily obtain the 3D profiles needed to solve the Euler equation.

2. DENSITY AND TEMPERATURE DEPROJECTION

In order to deproject the observed 2D surface brightness, $\Sigma(R)$, and emission-weighted temperature, $T_{\rm 2D}(R)$, we'll assume spherical symmetry. The continuum X-ray emission is, approximately, $\epsilon(r) = K\, n^2(r)\, T^{1/2}(r)$, with $K \approx 2.4 \times 10^{-27}$ in CGS units. The above approximation should be accurate for $kT > 1$ keV. For primordial gas (no metals) the approximation is very good, but the accuracy decreases for increasing metallicity.

The 2D emission-weighted temperature is:

$$T_{\rm 2D}(R) = \frac{2K \int_R^\infty T(r)[n^2(r)T^{1/2}(r)] \frac{r\,dr}{\sqrt{r^2-R^2}}}{2K \int_R^\infty [n^2(r)T^{1/2}(r)] \frac{r\,dr}{\sqrt{r^2-R^2}}} \,. \quad (1)$$

But the denominator of the above equation is the surface brightness, i.e.:

$$\Sigma(R) = 2K \int_R^\infty [n^2(r)T^{1/2}(r)] \frac{r\,dr}{\sqrt{r^2-R^2}} \,. \quad (2)$$

Therefore we have a system of two equations and two unknown functions:

$$\begin{cases} \Sigma'(R)T_{\rm 2D}(R) = & 2\int_R^\infty T^{3/2}(r)n^2(r) \frac{r\,dr}{\sqrt{r^2-R^2}} \\ \Sigma'(R) = & 2\int_R^\infty T^{1/2}(r)n^2(r) \frac{r\,dr}{\sqrt{r^2-R^2}} \end{cases} \quad (3)$$

where $\Sigma'(R) = \Sigma(R)/K$. The above integral equations are solved with the Abel transform. We obtain the deprojected (3D) temperature as:

$$T(r) = \frac{\int_r^\infty \left(\frac{\partial[\Sigma'(R)T_{\rm 2D}(R)]}{\partial R}\right) \frac{dR}{\sqrt{R^2-r^2}}}{\int_r^\infty \left(\frac{\partial \Sigma'(R)}{\partial R}\right) \frac{dR}{\sqrt{R^2-r^2}}} \,. \quad (4)$$

and the density:

$$n(r) = \left\{ \frac{-1}{\pi\sqrt{T(r)}} \int_r^\infty \left(\frac{\partial \Sigma'(R)}{\partial R}\right) \frac{dR}{\sqrt{R^2-r^2}} \right\}^{1/2} \,. \quad (5)$$

Except for special cases, the de-projected profiles will be rather cumbersome functions. Numerical solutions, however, involve the evaluation of only two integrals.

3. DENSITY AND TEMPERATURE PROFILES

We assume two projected analytical profiles for the observed quantities. The surface brightness:

$$\Sigma(R) = \Sigma_0 \exp\left[-\left(R/a\right)^{\nu}\right] , \qquad (6)$$

given by the Sérsic profile, shown by Demarco et al. (2004) to be a good description of cool-core clusters, and the temperature profile used by Durret et al. (2005):

$$T_{2\mathrm{D}}(R) = T_0 + 2T_0 \frac{\sqrt{R/r_t}}{1+(R/r_t)^2} . \qquad (7)$$

As an example we use the cluster Abell 85. For this cluster, we have an accurate temperature and surface brightness profiles, obtained with both XMM-*Newton* and *Chandra*. Fitting the observed profiles and deprojecting we obtain the 3D quantities. Fig. 1 shows the temperature fit and the 3D deprojection.

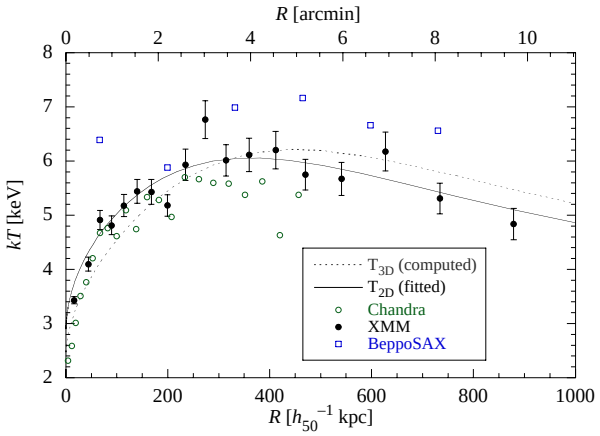

Figure 1. Abell 85 temperature profile obtained with BeppoSAX, XMM-Newton, and Chandra. The 2D temperature fit is the full line; the computed 3D temperature is the dashed line.

Abell 85 is relaxed in the centre, but shows clear signs of recent mergers. It has a cool-core and the brightness profile is well fitted by a cuspy profile – the Sérsic profile (Durret et al. 2005)

Consequently, the total mass density profile (Fig. 2) is as cuspy as the ΛCDM cosmological N-body simulations predictions. Moreover, a fit of the NFW profile (Navarro et al. 1997) gives a concentration parameter $c \approx 5$.

In fact, if the cluster presents a cool-core, the brightness profile must be steep, so that the total mass is always positive. In other words, if the brightness profile is indeed a β-model (with a central, flat core), then the cluster cannot have a decreasing temperature profile towards the centre.

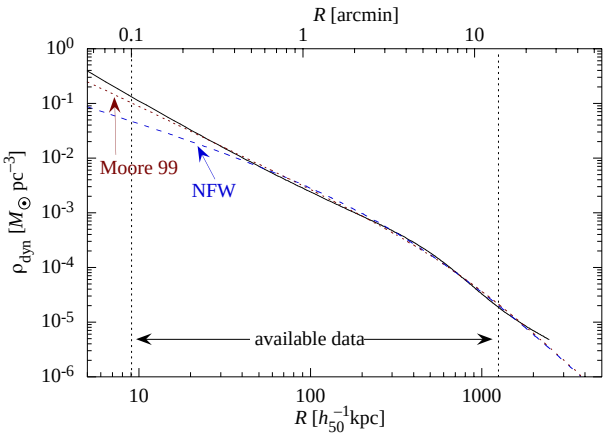

Figure 2. Dynamical mass density as a function of radius derived from our data: $\rho_{dyn} \propto r^{-1.9}$ (full line) and compared to a Navarro et al. (1997) model (dashed line) and to a Moore et al. (1999) profile (dotted line). The two vertical dotted lines indicate the spatial resolution (left) and the limit of our data (right).

ACKNOWLEDGMENTS

We acknowledge financial support from FAPESP (São Paulo/Brazil) and CAPES/COFECUB French-Brazilian cooperation.

REFERENCES

De Grandi S., Molendi S., 2004, IAU Coll. 195, 134, Ed. A. Diaferio, (astro-ph/0407392)

Demarco, R., Magnard, F., Durret, F., Márquez, I., 2003, A&A 407, 437

Durret, F., Lima Neto, G. B., Forman, W., 2005, A&A 432, 809

Moore, B., Ghigna, S., Governato, F., et al., 1999, ApJLett 524, 19

Navarro, J. F., Frenk, C. S., White, S. D. M., 1997, ApJ 490, 493

Neumann, D. M., 2005, A&A 439, 465

Piffaretti, R., Jetzer, Ph., Kaastra, J. S., Tamura, T., 2005, A&A 433, 101

Pointecouteau, E., Arnaud, M., Pratt, G. W., 2005, A&A 435, 1

Vikhlinin, A., Markevitch, M., Murray, S. S., Jones, C., Forman, W., Van Speybroeck, L., 2005, ApJ 628, 655

THE CLUSTER-GALAXY CONNECTION: THE MORPHOLOGY OF CLUSTERS

I. Sakelliou

Max-Planck for Astronomy, D-69117 Heidelberg, Germany

ABSTRACT

It is now common wisdom, that structure in the Universe is formed hierarchically, by the merging of smaller units. Large clusters of galaxies are formed by the continual falling of galaxies into the clusters. The interactions of the cluster gas (ICM) with the moving galaxies modify the properties of the galaxies and the clusters by, for example, stripping the galaxies, and heating the ICM.

If we want to: i) understand the impact of galaxy-cluster interactions, ii) get a better insight into the factors that control the evolution of galaxies and clusters, iii) find when, how, and if, the transformations of galaxies and clusters occur, we need to study the clusters and their galaxies by combining X-ray and optical/IR data of merging/evolving clusters.

I am presenting a program, that is aiming at combining the properties of clusters obtained from X-ray observations, with those of their galaxies found from optical data. Preliminary results are shown, and future prospects are outlined.

1. INTRODUCTION

As structure forms via violent merging events, physical processes take place that have significant impact on the properties of the constituents of clusters [i.e. intracluster medium (ICM), and the galaxies].
•*Effects on the galaxies:* It has been known for long time that the galaxies' environment is responsible for their properties [e.g., (2)]. Although the physical processes that stimulate or regulate star formation, nuclear activity, and the transformation of galaxies are fairly well known, it is unclear which one dominates, and under which conditions. These processes are (i) galaxy-galaxy interactions and merging, and (ii) galaxy-ICM interactions, manifested as ram pressure stripping and accretion of ICM onto and around the galaxies. As theoretical work has shown, (i) galaxy-galaxy interactions and merging, and (ii)galaxy-ICM interactions, manifested as ram pressure stripping and accretion of ICM onto and around the galaxies, can strip the interstellar media (ISM), trigger nuclear activity, compress the ISM and induce star formation, igniting new starbursts [e.g., (1)]
•*Effects on the clusters:* The clusters are also affected during the above interactions. The ICM, for example, is heated up by the outflows from the galaxies, which can be in the form of galactic winds from starburst galaxies, and/or radio jets from active galaxies. The galactic motion also contributes in the heating of the ICM. Evidence for the importance of galaxy/cluster interactions in the modification of the properties of the ICM is rapidly accumulating from the high quality data of the two major X-ray satellites (NASA's *Chandra* and ESA's *XMM-Newton*).

In forming/evolving clusters, the galaxies are falling towards the cluster centre, leaving galactic material behind forming a trailing galaxy wake. We have suspected for long time (based on theoretical and observational grounds) that ram pressure stripping would take place. If galaxies are stripped from their gas, the star formation rate can essentially stop or decline. On the other hand, during the galactic motion, the ISM might also get compressed by the ram pressure and the gravity force. Compression regions should be located in-front of the galactic core (immediately behind the leading bow shock, if the galactic motion is supersonic), and in the wake, due to the gravitational deflection and concentration of ICM behind the moving galaxy [Bondi-Hoyle accretion; e.g., (4)]. This extra compression may lead to a new burst of star formation.

2. DEFINING THE CLUSTER MORPHOLOGY

In order to understand the problems set in § 1 we need first to correlate the morphology of clusters in the optical/IR and X-ray lights. The feasibility of a method based on three 'simple' measures of the cluster morphologies (*centroid offset, ellipticity, and position angle*) is firstly explored. This method was first developed to investigate the structures of barred galaxies, and it was also applied to the X-ray images of clusters by (3).
•*Centroid offset:* The cluster images are analysed in circular annuli of constant width and increasing radius. The

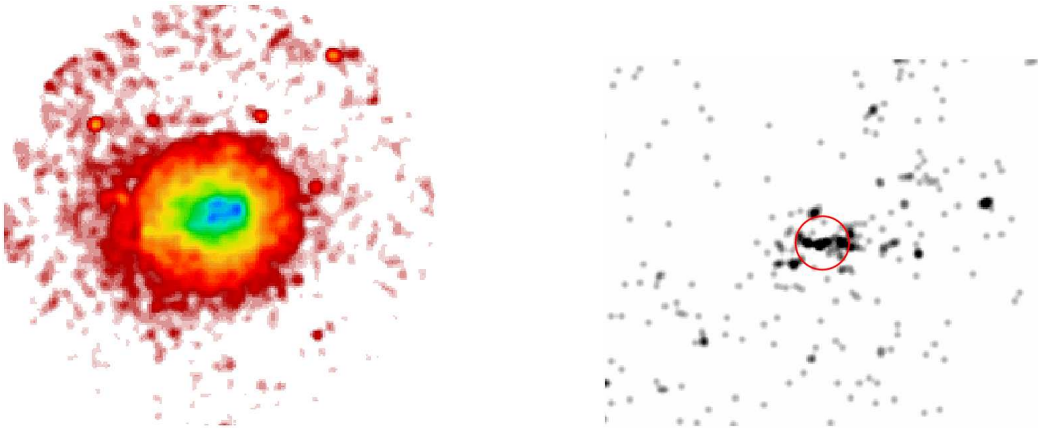

Figure 1. Left panel: The XMM-Newton mosaic of Abell 2255. Images from the MOS1 and MOS2 detectors in the (0.5-10.0) keV energy range have been co-added. Right panel: Distribution of all the galaxies with a redshift $0.06 < z < 0.1$ *taken from the SDSS. The red circle shows the position and extent of the XMM-Newton mosaic of the left panel.*

annuli are not concentric. The centroid offset for each annulus is defined as the difference between the geometrical and the intensity-weighted centre of each annulus.
•*Ellipticity:* Image counts (cnt) are accumulated in sectors with increasing angle (θ) along the above mentioned circular annuli. If the cluster is elliptical the distribution θ-cnt is double peaked, and its shape depends on the ellipticity and position angle of the cluster's shape.
•*Position angle:* It is calculated from the same θ-cnt distribution.

3. THE DATA

The 'simple' measures of cluster shapes described in § 2 has been applied to both, X-ray, and optical data of clusters. The need for 'simple measures' is dictated by the requirement that they have to be able to work efficiently for clusters at higher redshifts, for which the count rate in the X-ray images is expected to be low. To test this method, X-ray and optical data of nearby clusters are being used.

3.1. X-ray and optical data of Abell 2255

The first cluster that is being used is the nearby (z=0.08) cluster Abell 2255. The *XMM-Newton* data have been explored and presented in (5). Abell 2255 a rich cluster at a global temperature of ∼7 keV, and the *XMM-Newton* data showed that it is a merging cluster after the core crossing. The *XMM-Newton* mosaic is shown in Fig. 1(left panel).

Abell 2255 has been in the field of the SDSS survey. Galaxies that are within $6 \times 6\, deg^2$ around the cluster centre and in a redshift bin with z $0.06 < z < 0.1$ have been selected. A smoothed image of the galaxy distribution is shown in Fig. 1(right panel).

4. RESULTS AND FUTURE PROSPECTS

The analysis outlined in § 2 has been applied succefully to the X-ray and optical data of Abell 2255. A visual inspection of Fig. 1 indicates that the ICM and galaxy distributions are both elongated along the x-axis. The analysis of the *XMM-Newton* and SDSS data with the techniques of § 2 finds that the centroid offset increases monotolically with radius in both the X-ray and the optical images. The position angles of the ICM and galaxy distribitions are restricted both around $\theta = 0\, deg$.

Future plans include: 1) Application of the same or similar techniques to clusters at higher redshifts. The success of such a task is mainly challenged by the low count rates from distant clusters in the X-ray images. 2) Use of the same morphology measures of to analyze simulated X-ray images of clusters at different epochs of their evolution. Such a comparison will callibrate the morphology measures, and it will be possible to use them as indicators of the dynamical "age" of the ICM.

REFERENCES

[1] Barnes J.E., Hernquist L., 1992, ARA&A, 30, 705
[2] Kodama T., Bower R.G., 2001, MNRAS, 321, 18
[3] Mohr J.J., et al. 1995, ApJ, 447, 8
[4] Sakelliou I., 2000, MNRAS, 318, 1164
[5] Sakelliou I., Ponman T.J., 2005, MNRAS, submitted

ACKNOWLEDGMENTS

The author is greatful to T.J. Ponman, E. Bell, S. Falter, P. Motl, S. Borgani, and A. Dressler for interesting discussions, and help with the data. IS acknowledges the support of the European Community under a Marie Curie Intra-European Fellowship.

XMM-*NEWTON* RGS AND *CHANDRA* LETGS OBSERVATIONS OF THE WHIM IN 1ES 1028+511

K. C. Steenbrugge, F. Nicastro, and M. Elvis

Harvard-Smithsonian Center for Astrophysics, 60 Garden street, Cambridge, MA 02138, USA

ABSTRACT

We report preliminary results on the detection of the Warm-Hot Intergalactic Medium (WHIM) along the line of sight toward the blazar 1ES 1028+511 (z = 0.361). 1ES 1028+511 was observed for 150 ks with the low energy transmission grating in combination with the high resolution camera onboard *Chandra*. An additional 300 ks observation was obtained using the reflection grating spectrometers (RGS) onboard XMM-*Newton*. We report the detection of three absorption lines which can be attributed to the WHIM, and compare the results with theoretical predictions.

Key words: Warm-hot intergalactic medium, blazar: 1ES 1028+511, X-ray spectroscopy.

1. INTRODUCTION

At z $>$ 2 the vast majority of the baryons ($>$ 76 %, Rauch (1998); Weinberg et al. (1997)) are found in a mildly photoionized (by the metagalactic UV radiation field) phase of the IGM, through a forest of HI Lyα absorption lines in the background O-UV spectra of background quasars. However, at z $<$ 2 only $\sim$ 30 % of the baryons are detected in the residual local Lyα forest (Penton et al., 2004), and already-virialized structures account for even a smaller fraction $\sim$ 12 % Fukugita (2003). About 54 % of the baryons are eluding detection in the local Universe. Hydrodynamical simulations for the formation of structures in a Λ-CDM Universe, provide a self-consistent solution to this puzzle: about half of the baryons in the local Universe should still be confined in the IGM, but shock-heated to temperatures of about $10^5 - 10^7$ K, during the collapse of density perturbation.

At such high temperatures H is fully ionized and so the gas is transparent to Optical and UV observations. However, electronic transitions from highly ionized metals, can still provide a significant source of opacity. CV-VI, OVII-VIII and NeIX-X Kα are the most intense of these transitions, in gas with Solar-like composition. All these transitions fall in the soft X-ray band, and can now be detected thanks to the high-resolution spectrometers of *Chandra* and XMM-*Newton*.

1ES 1028+511 (Schachter et al. (1993); Elvis et al. (1992)) is at a redshift of 0.361 (Polomski et al., 1997) thus, according to simulations (Fang et al., 2002), we expect to detect 1 system with an O VII column density equal or greater than 10^{16} cm^{-2}.

2. OBSERVATIONS AND DATA REDUCTION

1ES 1028+511 was observed by *Chandra* for 149.86 ks on March 11, 2004, using the Low Energy Transmission Grating in combination with the High Resolution Camera (LETGS). We extracted the LETGS spectrum using the pipeline described by Kaastra et al. (2002), which includes an empirical correction for the known wavelength problem in the LETGS (Kaastra et al., 2002) and fitted it with responses that include the first 10 positive and negative orders.

The XMM-*Newton* observation was split into three separate observations, between June 20 to 24, 2005. The exposure times were 104.2, 95.2 and 101.4 ks. The data were reduced using the SAS version 6.1.0 standard threads.

In all fitting, we fitted the RGS and LETGS spectra (7 spectra) simultaneously. Errors were evaluated at 68 % significance level, for one interesting parameter. The data were analyzed using the *spex* package (Kaastra et al., 2002b).

3. ABSORPTION LINES

Three absorption lines are detected with a at least 2 σ significance. Table 1 lists the equivalent width (EW) of these absorption features, the most likely identification, and the ionic column densities assuming a velocity broadening of 100 km s^{-1}.

The 28.74 Å line can be identified as an O VII Kα line and has a 2.5 σ significance. However, this line is only

Table 1. The observed wavelength, EW, ion column density, the redshift and the most likely identifications.

λ_{obs} Å	EW mÅ	log N_i cm^{-2}	redshift	iden.
28.74	34±12	15.7±0.4	0.33	O VII Kα
46.25	24±7	15.6±0.2	0.15	C V Kα
			0.12	C IV Kα
48.80	32±10	15.8±0.2	0.21	C V Kα
			0.18	C IV Kα

Table 2. The 1 σ upper limits for the O VII and O VIII column density.

redshift	N_{OVII} log cm^{-2}	N_{OVIII} log cm^{-2}
0.15	> 15.5	> 15.9
0.21	> 15.3	> 15.9

seen in the positive order of the LETGS and has a full width half maximum of 500 km s^{-1}. The line falls on an instrumental feature in the RGS spectra. An alternative, but unlikely identification is z=0 N VI Kα. Therefore it should be considered as a possible detection of O VII Kα.

The 46.25 Å and 48.80 Å lines can be either identified as C V or C IV lines. The significance of the lines is 3.4 and 3.2 σ respectively. Table 2 lists the OVII−OVIII column density 1-sigma upper limit at the redshifts of the CV identifications. If the lines are C IV, they are probably imprinted by mildly photoionized gas at temperatures of about 10^4 K, and so are not tracking WHIM filaments. For both redshifts the C IV 1549 Å line is redshifted out the HST STIS spectrum.

4. COMPARISON WITH SIMULATION

Fig. 1 shows the expected number of WHIM absorbing systems per unit redshift versus O VII column density (Fang et al., 2002). The the Gehrels upper limit (square), the measured column density for O VII (circle), and the measured column density for Mrk 421 (star). The box indicates the expected number of O VII lines and column densities from the detected C V lines. All data points are consistent with the expectation of hydrodynamical simulations by Fang et al. (2002).

5. ACKNOWLEDGEMENTS

K. C. S. and F. N. acknowledges support from the Chandra grant G04-5101X. F. N. acknowledges support from the XMM grant NNN046D836.

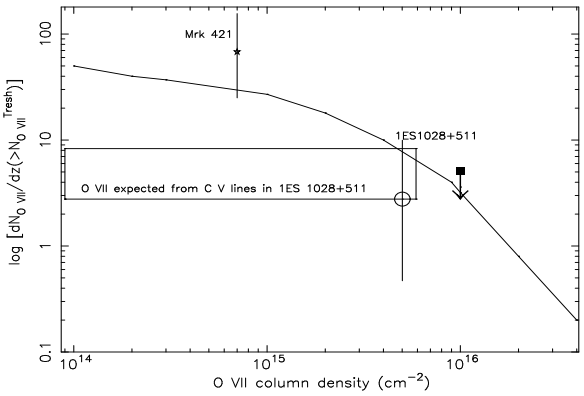

Figure 1. The predicted number of intervening WHIM absorbers per redshift versus the O VII column density (solid line) (Fang et al., 2002). The result for the Mrk 421 spectra (Nicastro et al., 2005) (star), the Gehrels upper limit (square), and assuming we detect O VII (circle). The box indicates the expected number of O VII absorption lines and their column density calculated from the C V detections in the 1ES 1028+511 spectra.

REFERENCES

Elvis, M., Plummer, D., Schachter, J., & Fabbiano, G. 1992, ApJS, 80, 257

Fang, T., Bryan, G. L., & Canizares, C. R. 2002, ApJ, 564, 604

Fukugita, M. 2003, Cosmic Matter Distribution: Cosmic Baryon Budget Revisited

Kaastra, J. S., Mewe, R., & Raassen, A. J. J. 2002b, Proc. Symp. New Visions of the X-ray Universe in the XMM-*Newton* and *Chandra* era

Kaastra, J. S., Steenbrugge, K. C., Raassen, A. J. J., et al. 2002, A&A, 386, 427

Nicastro, F., Mathur, S., Elvis, M., et al. 2005, ApJ, 629, 700

Penton, S. V., Stocke, J. T., & Shull, J. M. 2004, American Astronomical Society Meeting Abstracts, 204,

Polomski, E., Vennes, S., Thorstensen, J. R., Mathioudakis, M., & Falco, E. E. 1997, ApJ, 486, 179

Rauch, M. 1998, ARA&A, 36, 267

Schachter, J. F., Stocke, J. T., Perlman, E., et al. 1993, ApJ, 412, 541

Weinberg, D. H., Miralda-Escude, J., Hernquist, L., & Katz, N. 1997, ApJ, 490, 564

XMM-NEWTON LEGACY CLUSTERS - AN INVESTIGATION INTO BACKGROUND REMOVAL.

R.F. Temple[1], G.W. Pratt[2], T.J. Ponman[1], H. Böhringer[2], S. Raychaudhury[1], J. Rasmussen[1], and M. Arnaud[3]

[1]University of Birmingham, Edgbaston, Birmingham, B15 2TT, England
[2]MPE, Garching, Giessenbachstraße, 85740 Garching, Germany
[3]CEA/Saclay, Service d'Astrophysique, L'Orme des Merisiers, Bât. 709, 91191 Gif-sur Yvette Cedex, France

ABSTRACT

We investigate the treatment of background removal in the analysis of observations of galaxy clusters in the *XMM-Newton* Cluster Legacy project. Particularly for clusters that fill the field-of-view, care needs to be taken when removing the background from the source data. We compare various schemes for background removal, and evaluate their effect on the derived physical models such as temperature profiles of the clusters.

Key words: X-rays: diffuse background; X-rays: general.

1. INTRODUCTION

The *XMM-Newton* Cluster-Legacy project, undertaken by a consortium led by MPE, Garching, including the University of Birmingham and CEA, Saclay, involves a sample of 34 galaxy clusters observed with *XMM-Newton* (Böhringer et al., in prep). Correct treatment of the background is essential for analysing faint or diffuse sources. Using a local background region can be hazardous, due to the difference in vignetting between the source and local background regions. Using blank-sky background files can provide a better gauge of the background than a local background but care is still required to ensure that the background files are treated properly. Throughout this paper, the background files used are those of Read & Ponman (2003). In this paper we will look at the effect of different background subtraction methods on the temperature profiles of the cluster RXC0547-3152. This cluster was selected since it wasn't substantially affected by flaring.

2. USING BLANK-SKY BACKGROUND FILES

As discussed in §1, a local background subtraction causes problems due to vignetting. One of the possible solutions is to use the SAS task EVIGWEIGHT such that the photons are 'corrected' such that the events correspond to a flat detector. However, the events also contain non-vignetted particles which also get boosted by this task.

The blank-sky background files are a superposition of many *XMM-Newton* observations and need to be matched with the source dataset. The mean background count rate is different to that of the source data, and needs to be normalised accordingly. This can be done either by using the ratio of the exposure times, the high energy count rates or the out of field-of-view (FOV) count rates. The latter is used for the normalisation of the background in this paper unless specified otherwise.

The shape of the background also varies considerably at different count rates. Fig. 1 indicates the shape of the background spectrum at three different count rate cuts.

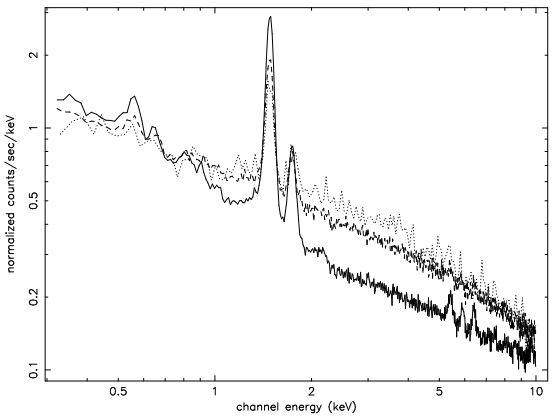

Figure 1. Count rates for MOS1 blank-sky background. The data have been scaled such that they are normalised to the same total integrated flux (Solid line: 0.1-0.2 c/s; Dashed line: 0.2-0.4 c/s; Solid line: 0.4-0.6 c/s)

Given the difference of shape in the background at different count rates, it is possible to do a count rate selected cut of the blank-sky background based on the mean count rate of the source data.

In Fig. 2 radial temperature profiles are plotted using the

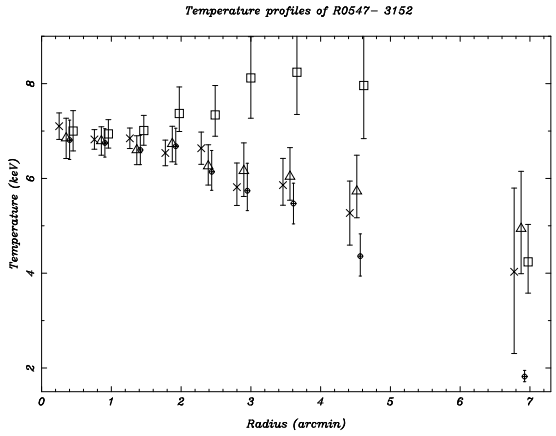

Figure 2. Temperature profile of RXJ0547-3152 using different background subtraction methods (Triangles:local background; Circles: Scaled blank background by out of FOV count rate; Squares: Scaled and count rate selected blank background; Crosses: Scaled by high energy count rate and double subtracted blank-sky background.)

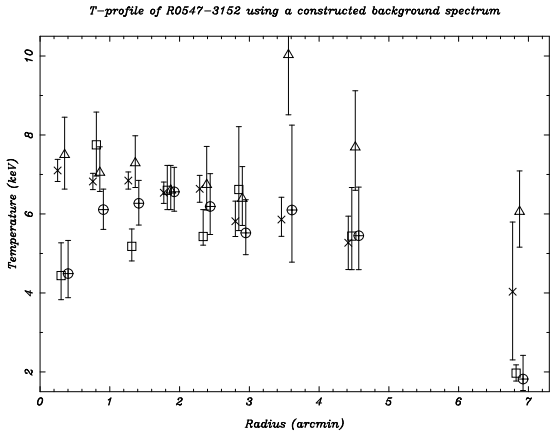

Figure 3. Temperature profiles comparing blank-sky background subtraction with constructed backgrounds (Cross: Blank sky background scaled by high energy count rates and double subtracted; Square: Constructed background with all parameters allowed to float; Circle: Constructed background ($\Gamma = 1.4$); Triangle: Constructed background ($\Gamma = 0$))

same annular bins for four different methods of background subtraction. Firstly, a local background (triangle) is plotted with the events weighted for vignetting. Secondly a blank-sky background is used that has been scaled by out of FOV count rates (circle). The events are not vignetting-corrected here as the same region is used for the source and background spectra. Thirdly, a background scaled by out of FOV and cleaned based on the mean count rate of the source is plotted (square).This is also not corrected for vignetting. Finally, a temperature profile scaled by high energy count rates and double subtracted based on the soft excess is plotted (cross). The events here are corrected for vignetting as the double subtraction involves using a different region of the camera to determine the soft excess.

The differences between derived temperatures, particularly at high radius, indicate the need for further review of the methods of background subtraction. The small errors at high radius for the blank-sky background are the result of a poor χ^2 fit. This would imply that a simple scaling of the background results in satisfactory fits in high surface brightness regions, but represents low surface brightness regions poorly. This could be improved by subtracting a soft excess (double subtraction) off the spectra.

The background scaling ought to be applied to the background events file before any cleaning is done based on the source cut. A scaling of the spectrum, as with the two background files scaled by the out of FOV, may result in parts of the background spectrum being clipped unnecessarily. This process may cause the wrong selection of the background count rate when clipping based on the source count rate leading to peculiar temperatures as seen in the outer bins.

3. USING A CONSTRUCTED BACKGROUND

Using a method designed by Snowden and Kuntz, the background can be decomposed into several components, each of which can be modelled or extracted from source data. The quiescent particle background spectrum is determined by scaling out of FOV spectra with the closed filter wheel spectra. The soft proton background is modelled using *ROSAT* All Sky Survey (RASS) data which is fitted in XSPEC. The Al and Si lines are modelled by gaussians (also fitted in XSPEC). Finally, the cosmic background is modelled by three thermal components and a powerlaw (fitted through XSPEC). One of the limitations of this method is that this is only applicable to the MOS cameras due to PN having insufficient out of FOV regions.

When a constructed background (triangle) was compared to a blank sky background (cross) in Fig. 3, the fits at low radius were considerably lower than expected. We determined this to be due to the powerlaw component in the cosmic background softening the spectrum at low radii. Two permutations for varying the spectral index (Γ) were tried i.e. removing the component (triangle); and fixing it at the value 1.4 (circle). This method clearly needs further study to reproduce blank sky background spectra, but could be a powerful tool for background subtraction, particularly if the source covers the entire FOV and double subtraction is not possible.

REFERENCES

Böhringer et al., in preparation.

Read A.M. & Ponman T.J. A&A, 409, 395

CHANDRA X-RAY SPECTRA FROM HYDRO SIMULATIONS OF GALAXY CLUSTERS

R. Valdarnini

SISSA, Via Beirut 2-4 34014 Trieste Italy

ABSTRACT

Hydrodynamic cluster simulations are used to construct spatially resolved X-ray spectra as expected from Chandra. The constructed spectra are fitted using a single temperature emission model. The biasing of spectral temperatures with respect to mass-weighted temperatures is found to be influenced by two independent processes. The first scale dependency is absent in adiabatic runs and is due to cooling, whose efficiency to transform cold gas into stars is higher for cool clusters and this in turn implies a strong dependency of the spectral versus mass-weighted temperature relation on the cluster mass. The second dependency is due to photon emission because of cool gas which is accreted during merging events and biases the spectral fits. The behavior of the simulated temperature profiles can also be interpreted according to these two scale dependencies. Moreover, the temperature profiles of cooling clusters is scale dependent and can not be considered universal, the profile of massive clusters being shallower than that of cool clusters.

Key words: hydrodynamic simulations; clusters; X-rays.

1. INTRODUCTION

Results from a large sample of hydrodynamical/N-body simulations of galaxy clusters in a ΛCDM cosmology are used to simulate cluster X-ray observations. The physical modeling of the gas includes radiative cooling, star formation, energy feedback and metal enrichment that follow from supernova explosions. Mock cluster samples are constructed grouping simulation data according to a number of constraints which would be satisfied by a data set of X-ray measurements of cluster temperatures as expected from *Chandra* observations. The simulated events take into account the effects of quiescent background noise, detector geometry and energy response. The X-ray spectra from simulated clusters are fitted into different energy bands using the XSPEC *mekal* model. Relationships between spectral and mass-weighted global cluster temperatures are investigated for different cluster overdensities. Moreover, spatially resolved X-ray spectra of the simulated clusters are also used to investigate how the measured temperature profiles differ from the projected profiles obtained directly from simulations. The numerical sample is also subdivided according to the amount of substructure present in a given cluster, this allows us to investigate how spectral measurements are affected by the cluster dynamical state.

2. CONSTRUCTION OF THE SPECTRAL SAMPLES

The cosmological model assumes a flat CDM universe, with matter density parameter $\Omega_m = 0.3$, $\Omega_\Lambda = 0.7$, $\Omega_b = 0.019h^{-2}$ and $h = 0.7$ is the value of the Hubble constant in units of $100Kmsec^{-1}Mpc^{-1}$. The power spectrum has been normalized to $\sigma_8 = 0.9$ on a $8h^{-1}Mpc$ scale. In order to construct the numerical sample, the 120 most massive clusters were selected from a N-body cosmological simulation with box size $L_1 = 200h^{-1}Mpc$. The procedure is repeated with a simulation having box size $L_2 = 400h^{-1}Mpc$ and the 32 most massive clusters are chosen to be part of the final sample. These 152 clusters are then resimulated individually according to the multi-mass technique using a multistep hydrodynamic TREESPH code in which the modeling of the gas physics takes into account: gas cooling, star formation, energy and metal feedback from SN explosions. A more detailed description of the simulations can be found in Valdarnini (2003). A large sample of hydrodynamic simulations of galaxy clusters is then constructed and for each cluster all of the hydro variables are output at various redshifts.

In order to obtain simulated spectral fit temperatures the simulated photon spectra are first calculated from the simulated clusters observed at various redshifts along a given line of sight. To the binned source spectra are then added properly normalized background spectra. The files are subsequently convolved with a template pair of area response file (ARF) and redistribution matrix file (RMF) of the *Chandra* observatory. Finally, the generated event files are fitted by a single temperature *mekal* model available with the XSPEC library, provided a certain number of constraints are satisfied. These constraints take into ac-

count the instrumental limits of the receiver. The *mekal* model with which the fits are performed has three free parameters: the gas temperature, the metallicity abundance and the normalization; the other parameters being kept fixed.

3. RESULTS

The global cluster spectral fits temperatures are obtained by applying the prescriptions previously described to a cluster sample which is constructed by grouping data from the simulation ensemble at redshifts $z = 0.087, 0.47$ and $z = 0.85$. The spectral fits are performed in the energy band $[0.5 - 10]keV$ and the source spectra are computed from gas emission within spherical volumes with radii r_Δ such that $M_\Delta = 4\pi r_\Delta^3 \Delta \rho_c(z)/3$ is the enclosed mass, where $\rho_c(z)$ is the critical density and $\Delta = 2500,\ 500,\ 200$. The spectral fit temperatures T_S^Δ are then compared against mass-weighted temperatures T_{mw}^Δ. The results indicate that the biasing of temperatures with respect to mass-weighted temperatures is found to be governed by two independent processes.

The first scale dependency is absent in adiabatic runs and is due to cooling, whose efficiency to transform cold gas into stars is higher for cool clusters and this in turn implies a strong dependency of the spectral versus mass-weighted temperature relation on the cluster mass. Mathiesen & Evrard (2001) argue that spectroscopic temperatures are biased toward lower values of the mass-weighted temperatures because spectroscopically determined temperatures are weighted by the fitting process according to the photon counts, From the spectral samples it is found that for massive clusters spectral temperatures are lower than mass-weighted temperatures, whereas $T_s \simeq T_{mw}$ as cool clusters are considered. This behavior follows from two effects: the way in which the sample is constructed and the introduction of the physical modeling of cooling in the simulations. At high redshifts the sample is dominated by massive clusters for which $T_s \lesssim T_{mw}$, because of selection effects at low redshifts the sample population is dominated by cool clusters. For these clusters the efficiency of galaxy formation is higher than in hot clusters. This implies a removal of the low-entropy cooled gas, transformed into stars, and a subsequent inflow of the surrounding high-entropy gas. Therefore, in this scenario, it follows that for cool clusters the central cluster temperature, in units of a characteristic cluster temperature, is higher than for massive clusters. The second scale dependency is correlated with the amount of cluster substructure and is independent from the first. This dependency is due to photon emission because of cool gas which is accreted during merging events and biases the spectral fits. These events have been quantified according to the power ratio method (Buote & Tsai 1995). The method works as follows. The X-ray surface brightness Σ_X along a given line of sight is the source term of the pseudo potential which satisfies the 2-D Poisson equation. The pseudo potential is expanded into plane harmonics and the $m - th$ coefficients of the expansion are calculated over a circular aperture of radius R_{ap}. The $m - th$ power ratios are then defined as $\Pi^m = log_{10} P_m/P_0$. The ratios P_m/P_0 are a measure of the amount of structure present on a given scale. For a relaxed configuration $\Pi^{(m)} \rightarrow -\infty$. For global cluster temperatures the results indicate the existence of a robust correlation between the spectral bias, which is defined as $(T_s^\Delta - T_{mw}^\Delta)/T_{mw}^\Delta$, and the amount of cluster substructure.

The behavior of the projected emission-weighted temperature profiles is investigated in the energy band $[0.5 - 7]keV$. The profiles have been calculated keeping fixed the chosen line of sight and the radial binning, in units of r_{200}, for all of the clusters. The profiles have been averaged over samples at redshifts $z = 0.116, 0.052, 0.039$ and $z = 0.025$. Because of the scale dependencies previously discussed, the sample of temperature profiles has been subdivided by grouping individual profiles into subsample according to the degree of regularity of the gas distribution of its cluster members. A cluster is part of a subsample denominated 'quiescent' if the value of Π_3 is below the threshold value which defines the 25% percentile of the cumulative distribution of the power ratios. Similarly, clusters which are members of the 'active' subsample have their value of Π_3 above the threshold which defines the 75% of the percentile of the distribution. The results indicate that quiescent clusters have scaled profiles which rise toward the cluster center, reaching their peak values at $r \simeq 0.02 r_{200}$ and with a steep decline thereafter. The profiles of active clusters are shallower than those of quiescent clusters and the peak heights are much more modest. These dependencies of the shape of the profiles on the value of P_3/P_0 have been obtained with $R_{ap} = r_{200}/2$ and indicate that the effects of merging on the gas distribution of the clusters are the main source for the differences in the profiles. According to this framework active clusters have profiles much shallower than quiescent clusters because their cores have accreted from subclumps a significant amount of cool gas through a number of merging events. For small values of the aperture radius ($R_{ap} \lesssim r_{200}/4$) the differences between the shape of the profiles from active and quiescent clusters are not as significant as those obtained with $R_{ap} = r_{200}/2$. This suggests that cools gas can significantly accrete into cluster cores only through major merging events, where the mass of the subclump is a significant fraction of the cluster mass. Moreover, the shape of the profiles is not universal and it is steeper at the cluster center for cool clusters than for the massive ones. This follows owing to the scale dependency introduced by cooling which implies for cool clusters higher central temperatures, in scaled units, than for massive clusters.

REFERENCES

Buote D.A. & Tsai J.C., 1995, ApJ, 452, 522

Mathiesen B. & Evrard A.E., 2001, ApJ, 546, 100

Valdarnini R., 2003, MNRAS, 339, 1117

X-RAY CONSTRAINTS ON THE DARK MATTER PROFILE OF A VERY RELAXED CLUSTER OF GALAXIES

L. Zappacosta[1], D. A. Buote[1], F. Gastaldello[1], P. J. Humphrey[1], J. Bullock[1], F. Brighenti[2,3], and W. Mathews[2]

[1]Department of Physics and Astronomy, University of California, Irvine
[2]UCO/Lick Observatory, Board of Studies in Astronomy and Astrophysics, University of California, Santa Cruz
[3]Dipartimento di Astronomia, Università di Bologna, Bologna, Italy

ABSTRACT

We have analyzed an XMM-Newton observation of the cluster Abell 2589. Apart from a low-level asymmetry in the central region, the cluster appears very relaxed and does not show presence of a central AGN. We derived constraints for the radial temperature, density and, assuming hydrostatic equilibrium, mass profiles. We find that the best fit to the dark matter profile is given by the Sersic-like profile proposed by Navarro et al. (2004). The NFW model does not provide a good fit. We also tested whether the central stellar component could affect the profile through the adiabatic contraction model but were unable to distinguish it from a simple dark matter + stars modeling.

Key words: X-rays: galaxies: clusters; dark matter; galaxies: clusters.

1. INTRODUCTION

Clusters of galaxies, being the largest bound and dark matter dominated objects in the universe, are an optimal place to test the predictions of cosmological simulations regarding the mass profile of their dark halos. In this regard their X-ray emission can be successfully used to constrain the mass profile as long as the emitting plasma is in hydrostatic equilibrium. For this reason, to compare with theoretical predictions, we need to study very relaxed systems that do not show any sign of disturbance in their morphology. Clusters like these are very rare since they often show signs of interactions with other objects and, especially the more relaxed ones, almost always show a central radio galaxy whose influence on the hot plasma can easily invalidate the assumption of hydrostatic equilibrium. Here we show the results of an XMM-Newton analysis of Abell 2589 (z=0.0414), a very relaxed cluster with no presence of central radio emission.

2. DATA REDUCTION

The data reduction was performed using SAS 6.0. We excluded the point sources by first looking at the PPS source list and then through a visual inspection. The $50\,\mathrm{ksec}$ observation we have analysed was affected by frequent periods of strong flaring. Having screened the data, based on light curves from a "source-free" region in different energy bands, the final exposure times were 17 ksec and 13 ksec respectively for the MOS and PN detectors. We modeled the background by performing a simultaneous fit of the spectra of the outermost 4 annuli we have chosen for the spectral analysis.

3. SPATIAL ANALYSIS

In Fig. 1 we show the XMM-MOS and Chandra X-ray images[1] of the cluster and their unsharp mask images obtained by differencing images smoothed by gaussian kernels of $5''$ and $40''$. The images show very regular isophotes with ellipticities of ~ 0.3. The only disturbance in the morphology is a southward centroid offset very well shown in the unsharped mask images. This offset region has an emission only 30% higher than the mean cluster emission at $\sim 60\,\mathrm{kpc}$ from the center corresponding to $\sim 15\%$ variation in the gas density. We also produced an hardness ratio map and could not find any significant non radial variation in temperature. The cluster has a central dominant bright galaxy centered at the X-ray peak. Beers et al. (1991) measured its relative velocity finding that is unusually high for a dominant galaxy. The distribution of galaxies shows a preferential north-south alignment (2.5 degrees to the south there is Abell 2593) and a big subclump to the north (in the opposite side of the X-ray offset) off-centered by $3'$ from the X-ray peak. The well relaxed gas phase appearance and the particular galaxy distribution may be revealing a mild process of accretion through the large-scale structure (Plionis & Basilakos, 2002) that does not greatly disturb the gas properties.

4. SPECTRAL ANALYSIS

We extracted spectra from 7 concentric annuli centered on the X-ray peak and obtained gas density and tem-

[1]The Chandra images are from a 14 ksec observation previously analized by Buote & Lewis (2004).

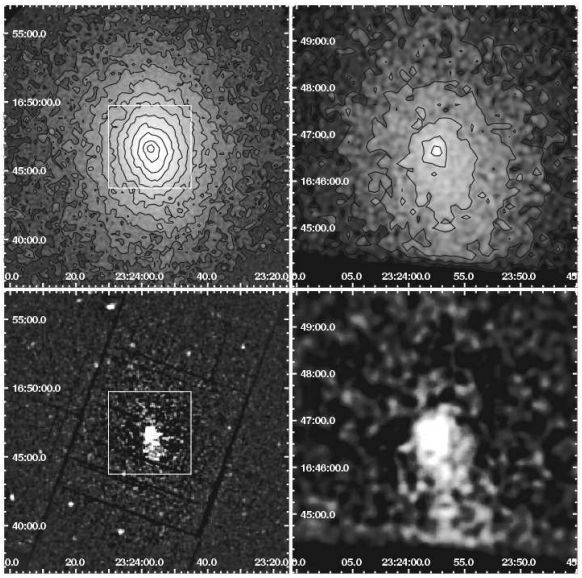

Figure 1. Upper panels: XMM-MOS and Chandra images. Lower panels: XMM-MOS1 and Chandra unsharp mask images. The XMM images report the Chandra field of view.

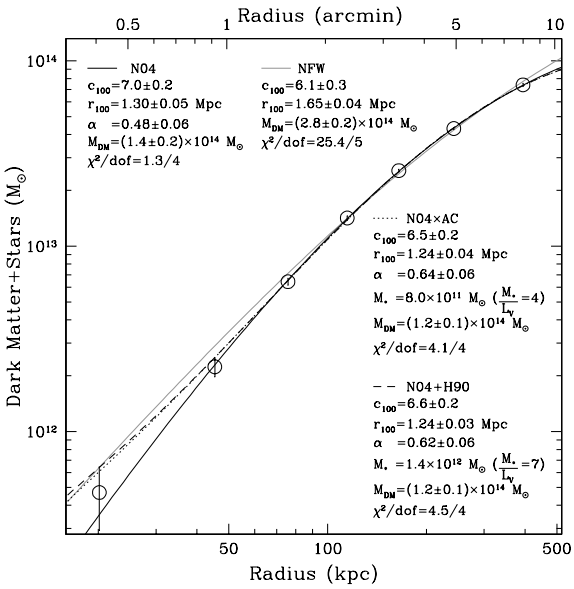

Figure 2. Dark matter+stars *profile. The models discussed in Sect. 5 are reported. The virial quantities refer to a halo whose mean density is* $100\,\rho_c$.

perature[2] profiles. We have analyzed only the projected quantities that with the quality of our data give us the best constraints. The best fit to the projected gas density is obtained using a cusped β model with core radius $r_c = 110 \pm 12\,\mathrm{kpc}$, cusp slope $\alpha = 0.3 \pm 0.1$ and $\beta = 0.57 \pm 0.01$. A single β model does not fit the inner two data points. The temperature profile of Abell 2589 is almost isothermal as already shown by the Chandra analysis of this object by Buote & Lewis (2004). The important deviations from isothermality are in the inner and outer data points that have lower temperatures. The resulting profile has been parametrized using two power-laws joined smoothly by exponential cut-offs.

5. DARK MATTER PROFILE

Given the parametrized quantities we can calculate the *total gravitating mass* profile (assuming hydrostatic equilibrium) and infer constraints on the dark matter profile. The *dark matter+stars* profile ($total\ mass - gas\ mass$) and the fitted models are shown in Fig. 2. The NFW profile (solid grey line; Navarro et al., 1997) is a good fit except for $\mathrm{r} < 80\,\mathrm{kpc}$. The updated Sersic-like CDM profile proposed by Navarro et al. (2004) (hereafter N04) is able to provide a good fit to the entire *dark matter+stars* profile. We tried to assess the level of importance of the stellar component due to the central bright galaxy, modeled with an Hernquist profile (Hernquist, 1990, hereafter H90), using parameters from Malumuth & Kirshner (1985). We also tested the influence of baryonic condensation into stars by using the adiabatic contraction model (AC) of Gnedin et al. (2004). If we let the total mass in stars M_* be free to vary, the data do not require any stellar component. If we fix $\mathrm{M}_*/\mathrm{L}_\mathrm{v}$ we can still obtain a reasonable fit allowing for $\mathrm{M}_*/\mathrm{L}_\mathrm{v} = 7$ in case of a N04+H90 profile (dashed black line) and $\mathrm{M}_*/\mathrm{L}_\mathrm{v} = 5$ in case of a N04 with adiabatic contraction ($\mathrm{N04} \times \mathrm{AC}$; dotted black line). In general we are not able to discriminate between models with and without adiabatic contraction.

[2]We fitted APEC models modified by the Galactic absorption using XSPEC.

ACKNOWLEDGMENTS

We thank O. Gnedin for providing us the code for the adiabatic contraction.

REFERENCES

Beers, T. C., Gebhardt, K., Forman, W., Huchra, J. P., & Jones, C. 1991, AJ, 102, 1581

Buote, D. A., & Lewis, A. D. 2004, ApJ, 604, 116

Gnedin, O. Y., Kravtsov, A. V., Klypin, A. A., & Nagai, D. 2004, ApJ, 616, 16

Hernquist, L. 1990, ApJ, 356, 359

Malumuth, E. M., & Kirshner, R. P. 1985, ApJ, 291, 8

Navarro, J. F., Frenk, C. S., & White, S. D. M. 1997, ApJ, 490, 493

Navarro, J. F., et al. 2004, MNRAS, 349, 1039

Plionis, M., & Basilakos, S. 2002, MNRAS, 329, L47

X-RAY PROPERTIES IN GALAXY CLUSTERS

Y.-Y. Zhang[1], H. Böhringer[1], A. Finoguenov[1], Y. Ikebe[1,2], K. Matsushita[1,3], P. Schuecker[1], L. Guzzo[4], and C. A. Collins[5]

[1]Max-Planck-Institut für extraterrestrische Physik, Garching, Germany
[2]National Museum of Emerging Science and Innovation, Tokyo, Japan
[3]Tokyo University of Science, Tokyo, Japan
[4]INAF - Osservatorio Astronomico di Brera, Merate/Milano, Italy
[5]Liverpool John Moores University, Liverpool, U.K.

ABSTRACT

Using XMM-Newton, we observed 14 distant X-ray luminous ($z \sim 0.3$) galaxy clusters selected from the REFLEX survey (REFLEX-DXL sample). We derived the X-ray properties of the REFLEX-DXL galaxy clusters using a double background subtraction method in Zhang et al. (2004). Cluster mass measurements based on the X-ray data have been used to study the X-ray galaxy cluster scaling relations and their intrinsic scatter. This is important for the use of clusters of galaxies as cosmological probes. We found that the X-ray properties of the REFLEX-DXL sample show an approximate self-similar behavior above 0.15–0.2 virial radii. This helps us to establish tight cluster mass–observables scaling relations, in particular the M–T relation with a scatter of 0.3 for M.

Key words: self-similar; cluster of galaxies; X-rays.

1. REFLEX-DXL

X-ray luminous (massive) clusters can be used in a variety of ways to perform both, cosmological and astrophysical studies. Excluding the cooling cores, a self-similar scaling of the ICM properties such as the temperature, density, and entropy of massive clusters (> 4 keV) is indicated in the ROSAT, ASCA, and Chandra observations, e.g. Arnaud et al. (2002), Reiprich & Böhringer (2002), and Vikhlinin et al. (2004), and simulations, e.g. Borgani et al. (2004). Precise ICM property measurements provide accurate cluster mass and gas mass fraction determinations. This is important for the study of the X-ray scaling relations and their intrinsic scatter for clusters of galaxies. So far, Böhringer et al. (2004) provide the largest catalog of X-ray clusters of galaxies, the ROSAT-ESO Flux-Limited X-ray (REFLEX) galaxy cluster survey. It is important to make an unbiased selection to compose a subsample of the REFLEX survey. We thus constructed an almost volume complete sample of 13 distant, X-ray luminous (DXL, $z = 0.27$ to 0.31, $L_X \geq 10^{45}$ erg s^{-1} for $0.1 - 2.4$ keV) galaxy clusters and one supplementary cluster at $z = 0.2578$ from the REFLEX survey, the REFLEX-DXL sample. The volume completeness correction can be done using the well known selection function of the REFLEX survey. This is a morphology-unbiased, flux- limited and volume-complete sample giving a representative example of morphological variations as shown in Fig. 2. We analyzed the REFLEX-DXL sample and explored ralibale ICM properties to determine an accurate cluster mass and gas mass fraction and to investigate the scaling relations and intrinsic scatter in Zhang et al. (2004), Zhang et al. (2005) and Finoguenov et al. (2005). The sample will be used to test the evolution of the temperature function in comparison to nearby cluster samples (Böhringer et al. in preparation). We adopt a flat ΛCDM cosmology with $\Omega_{\rm m} = 0.3$, $\Omega_\Lambda = 0.7$, and $H_0 = 70$ km s^{-1} Mpc^{-1}. Error bars correspond to 68% confidence levels.

2. CONCLUSION

An approximately self-similar behavior of these X-ray properties, such as metallicity, temperature, surface brightness, entropy, and gravitational mass, has been found in the $r > 0.1 r_{\rm vir}$ region for the REFLEX-DXL sample. We obtained an almost universal metallicity profile. We obtained an average temperature profile of the REFLEX-DXL clusters, which agrees with the previous studies within the observational dispersion. We performed the redshift evolution correction on the central entropies for the REFLEX-DXL clusters and obtained consistency with those for the nearby clusters in Ponman et al. (2003). The central entropies for the REFLEX-DXL sample agree with the scaling, $S \propto T^{0.65}$. The deviation around the self-similar model in the central region reveals

Table 1. Classification of the dynamical state. Col.(1): Classification. Col.(2): Cluster name.

Classification (Jones & Forman 1992)	RXCJ
Single	0307.0−2840 0532.9−3701
	2308.3−0211
Primary with small secondary	0232.2−4420 0303.7−7752
Elliptical	0043.4−2037 0437.1+0043
	0516.7−5430 1131.9−1955
Offset center	0014.3−3022 0528.9−3927
	0658.5−5556 2337.6+0016
Complex	2011.3−5725

additional physical processes and is thus correlated with the cluster morphology. The gas density and temperature profiles provide an excellent diagnostics of the cluster structure and yield precise determinations of the mass and gas mass fraction. The gas mass fractions are about 0.11 ± 0.07 and agree with previous studies by, e.g. Ettori et al. (2002), Sanderson et al. (2003) and Kotov & Vikhlinin (2005). The mass–observable relations of the REFLEX-DXL sample agree with the scaling relations of the nearby and more distant samples after the redshift evolution correction. As a morphology-unbiased sample, the cluster morphology has been taken into account to understand the systematics of the scaling relations.

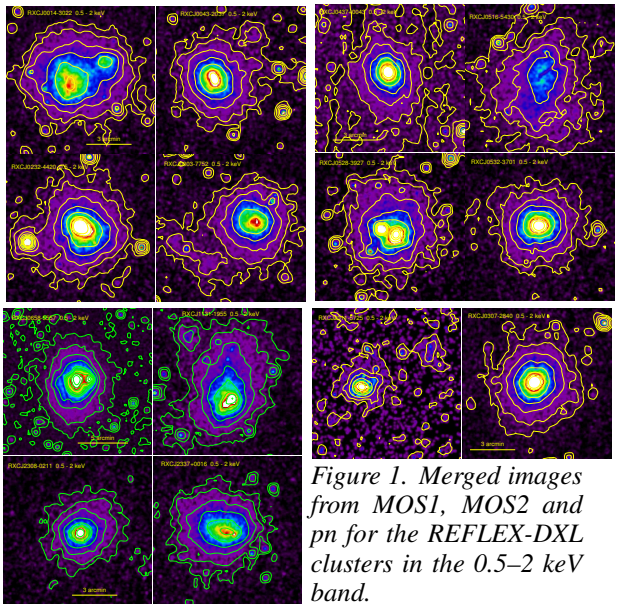

Figure 1. Merged images from MOS1, MOS2 and pn for the REFLEX-DXL clusters in the 0.5–2 keV band.

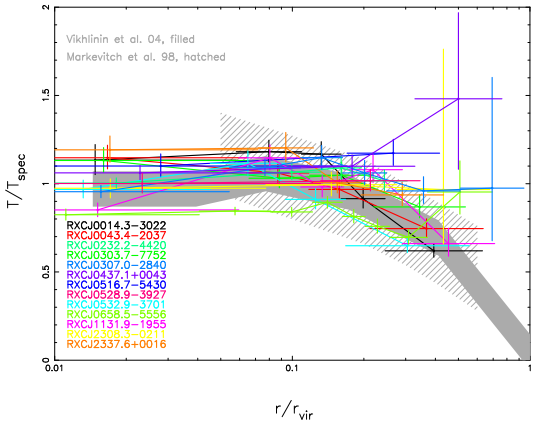

Figure 2. Temperature profiles of the REFLEX-DXL clusters. The shadows show the temperature profile ranges in Markevitch et al. (1998) and Vikhlinin et al. (2004).

ACKNOWLEDGMENTS

The XMM-Newton project is supported by the Bundesministerium für Bildung und Forschung, Deutschen Zentrum für Luft und Raumfahrt (BMBF/DLR), the Max-Planck Society and the Haidenhaim-Stiftung. Y.Y.Z. acknowledges support from ESA.

REFERENCES

Arnaud, M., Aghanim, N., & Neumann, M. 2002, A&A, 389, 1

Böhringer, H., Schuecker, P., Guzzo, L., et al. 2004, A&A, 425, 367

Borgani, S., Murante, G., Springel, V., et al. 2004, MNRAS, 348, 1078

Ettori, S., De Grandi, S., & Molendi, S. 2002, A&A, 391, 841

Finoguenov, A., Böhringer, H., & Zhang, Y.-Y., 2005, A&A, in press

Jones, C., & Forman, W. 1992, Proc. Clusters and superclusters of galaxies, ed. A. C. Fabian, NATO ASI Series, 366, 49

Kotov, O., & Vikhlinin, A. 2005, ApJ, in press

Markevitch, M., Forman, W. R., Sarazin, C. L., & Vikhlinin, A. 1998, ApJ, 503, 77

Ponman, T. J., Sanderson, A. J. R., & Finoguenov, A. 2003, MNRAS, 343, 331

Reiprich, T. H., & Böhringer, H. 2002, ApJ, 567, 716

Sanderson, A. J. R., Ponman, T. J., Finoguenov, A., Lloyd-Davies, E. J., & Markevitch, M. 2003, MNRAS, 340, 989

Vikhlinin, A., Markevitch, M., Murray, S. S., et al. 2004, ApJ, in press

Zhang, Y.-Y., Finoguenov, A., Böhringer, H., et al., 2004, A&A, 413, 49

Zhang, Y.-Y., Böhringer, H., Finoguenov, A., et al., 2005, A&A, submitted